The Dissertation Committee for Hojung Jung Certifies that this is the approved version of the following Dissertation:

INVESTIGATION OF COUPLED
THERMO-CHEMO-MECHANICAL PROCESSES FOR
SAFE CARBON GEOLOGICAL STORAGE

Committee:

_____
David Nicolas Espinoza, Supervisor

_____
Mary F. Wheeler

_____
David A. DiCarlo

_____
Matthew T. Balhoff

_____
Seyyed A. Hosseini

INVESTIGATION OF COUPLED

THERMO-CHEMO-MECHANICAL PROCESSES FOR

SAFE CARBON GEOLOGICAL STORAGE

by

Hojung Jung

Dissertation

Presented to the Faculty of the Graduate School of

The University of Texas at Austin

in Partial Fulfillment

of the Requirements

for the Degree of

DOCTOR OF PHILOSOPHY

The University of Texas at Austin

December 2018

Dedication

To My Family, Mom, Dad, Husband, and Brother

Acknowledgements

First and foremost, I would like to express my deepest appreciation to my supervisor, Dr. D. Nicolas Espinoza for his great support, guidance, patience, and advice during my Ph.D. program of study. He was highly approachable, responsive, and perceptive. From his passion, intuition and knowledge, I could learn a lot of academic and experimental skills and physical intuition.

I would like to express deep gratitude to my collaborators, Drs. Mary F. Wheeler and Gurpreet Singh for their numerical analysis supports and valuable comments. I greatly appreciate Dr. Seyyed A. Hosseini for kindly providing the field data and sharing rock samples from field. Further, I would like to appreciate my Ph.D. dissertation committee, Drs. Matthew T. Balhoff and David A. DiCarlo for their valuable comments and feedbacks.

The study is supported by Department of Energy, Center for Frontiers of Subsurface Energy Security (CFSES) and Center for Subsurface Modeling (CSM) in the University of Texas at Austin. I would have not been able to finish my study without the financial support of CFSES and CSM.

I appreciate my husband, Sang Hyon Han, for his emotional support with full of love. I will definitely miss my kind and warm PGE friends and the Korean softball crews. Finally, I appreciate all the technical and emotional supports from my research group Energy Applied Geomechanics Laboratory (EAGL) members.

Abstract

INVESTIGATION OF COUPLED
THERMO-CHEMO-MECHANICAL PROCESSES FOR SAFE
CARBON GEOLOGICAL STORAGE

Hojung Jung, Ph.D.

The University of Texas at Austin, 2018

Supervisor: David Nicolas Espinoza

Safe and permanent CO_2 storage in geological formations requires reservoir geomechanical stability. Injection of CO_2 into the subsurface changes the local pore pressure and, further, alters the effective stresses due to poro-thermo-chemo-mechanical coupled responses. Changes of pore pressure and effective stress may disrupt the host formation mechanical equilibrium. This alteration may result in geomechanical failure events such as fault reactivation and hydraulic fracturing. Such events can favor fluid migration paths for injected CO_2, induce seismic activity, and cause surface uplift. Examples of field observations during CO_2 injection include: (1) surface uplift at the In Salah project in Algeria, (2) absence if bottom-hole pressure (BHP) increase during injection in Cranfield, Mississippi, and (3) induced seismicity with magnitude M>1 in Decatur, Illinois. In this context, accurate estimations of pore pressure build up and local stress alteration induced by CO_2 injection are critical to avoid geomechanical perturbations. However, current

models and predictions often assume relatively homogeneous reservoirs without taking into account compositional behavior. Further, the effects of temperature and chemical reactions have not been rigorously incorporated into the interpretation of local stress alteration and the well response to CO_2 injection.

This dissertation shows geomechanical analyses of CO_2 geological sequestrations by three field case studies: Frio CO_2 sequestration pilot test in Texas, Cranfield CO_2 sequestration in Mississippi, and Crystal Geyser in Utah. Both Frio and Cranfield case studies are studied with the help of reservoir simulation and history matching of field data including assimilation of vertical heterogeneity from well-logging analysis and calibration with laboratory experiments. The Frio case study focuses on examination of reservoir capacity of a compartmentalized volume to avert fault reactivation. The Cranfield case study analyzes the influence of thermo-chemo-elastic processes on wellbore fracturing induced by CO_2 injection. The Crystal Geyser case study investigates the long-term chemical effects of CO_2-charged brine on rock mechanical properties through analyses and measurements on rock samples from the field, where a natural CO_2 leakage analog exists. The following conclusions are a result of this dissertation. CO_2 dissolution into brine reduces pore pressure build up significantly in small and compartmentalized reservoirs. Thermo-elastic and chemo-elastic effects alter local stresses and may trigger injector fracturing at bottom-hole pressures lower than expected. Capturing phase behavior, coupled thermo-chemo-mechanical processes, and reservoir heterogeneity are important factors to estimate reservoir capacity and prevent geomechanical perturbations.

Table of Contents

x

List of Tables

List of Figures

Chapter 1

Introduction

1.1 GEOMECHANICAL STABILITY CONCERNS ON CO₂ GEOLOGICAL SEQUESTRATION

Geological sequestration of carbon dioxide (CO_2) can help reduce carbon emissions to the atmosphere by storing CO_2 into deep subsurface formations (IPCC, 2005; Benson & Surles, 2006; Benson & Cole, 2008). CO_2 injection has been conducted in depleted reservoirs and in brine formations for geological sequestration and enhanced oil recovery (EOR) worldwide (IPCC, 2005; Steeneveldt et al., 2006; Hovorka et al., 2006). Projects in Decatur, Illinois and Cranfield, Mississippi tested industrial large-scale CO_2 capture and storage by injecting more than 1 million tons of CO_2 in the time lapse of several years (Hovorka et al., 2013; Bauer et al., 2016). However, large injection volumes and/or high injection rates may disturb the geomechanical equilibrium of the host formation by increasing pore pressure and altering the formation stresses (Bauer et al., 2016; Jung et al., 2017).

Changing pore pressure and formation stresses may induce fault reactivation and hydraulic fracturing if the pressure exceeds the corresponding thresholds for geomechanical failure (Ellsworth, 2013; Rinaldi and Rutqvist, 2013; Rutqvist et al., 2016). Such failure may result in new migration paths of the injected CO_2 (Espinoza and Santamarina, 2011, Rutqvist et al., 2016). Previous studies have demonstrated that injecting large volumes of water and CO_2 into subsurface may cause surface uplift and

1

induced seismicity with magnitude over M>1 (Frohilich, 2012; Ellsworth, 2013; Rinaldi and Rutqvist, 2013).

Injection of large volumes of CO_2 requires careful geomechanical analysis for secure storage over long times and large length scales (Sharp, 1975; Lake, 1996). The geomechanical analysis should include estimations of pore pressure window to avert geomechanical failure in the target formation. The pore pressure window depends on various factors including the reservoir size. Safe and permanent CO_2 geological storage requires in-depth understanding of the alterations of pore pressure and state of stress due to injection in order to prevent migration to the surface (Espinoza and Santamarina, 2011, Rutqvist et al., 2016).

1.2 GEOMECHANICAL STABILITY WITH THERMO-CHEMO-PORO-MECHANICAL PROCESSES

Investigating the evolution of pore pressure and formation stresses upon CO_2 injection is a challenging problem associated with reservoir petrophysycal properties, reservoir capacity, and thermo-chemo-poro-mechanical processes (Espinoza and Santamarina, 2011; Luo and Bryant, 2011; Gor and Prevost, 2013; Kim and Hosseini, 2013 & 2017, Jung et al., 2018). These coupled processes impact pore pressure, and stresses simultaneously, but the impact is different depending on time scale, distance from the injector, and reservoir capacity. Analytic geomechanical stability analyses considering all these coupled processes as a function of time and location may be difficult and sometimes impossible. Numerical analyses including thermo-chemo-poro-mechanical coupled

processes with varying time scales (from injection schedule time to geologic time) and length scale (from near wellbore to far-field) require high computational cost.

Pore pressure buildup induced by CO_2 injection depends on formation capacity, transport properties, and aquifer connectivity among others (Economides and Ehlig-Economides, 2010; Jung et al., 2017). Formation transport and geomechanical properties including porosity, permeability, and pore compressibility determine CO_2 plume movement and local pore pressure changes. These formation properties vary considerably with rock types and spatial heterogeneity with significant impact on CO_2 trapping and migration. CO_2 dissolution into brine may reduce pore pressure by reducing the injected CO_2 bulk volume. This increases apparent reservoir capacity and CO_2 trapping. An accurate quantification of pore pressure build-up requires estimation of target formation capacity by investigating rock properties, heterogeneities, and phase behavior effect for the fate of stored CO_2 (Jung et al., 2017; Jung and Espinoza, 2018).

Injecting CO_2 at surface ambient temperature into a formation may lower the temperature of the resident brine and rock. The temperature alteration may induce rock shrinkage and reduce reservoir stresses in the near-wellbore region during injection (Luo and Bryant, 2011; Gor and Prevost, 2013). CO_2 injection in Cranfield resulted in the bottom-hole temperature (BHT) reduction by more than 50°C (Kim and Hosseini, 2013). Non-trivial temperature reduction in BHT can alter the stress considerably near the injector depending on the thermo-elastic and transport properties of the formation. Decreases in effective stress may lead to injector failure (Jung and Espinoza, 2018; Jung et al., 2018 (In

3

review)). Thermo-mechanical assessment of CO_2 injection is critical to wellbore stability and short-term fate of injected CO_2.

Injecting CO_2 in saline aquifers acidifies the resident brine, and the chemically reactive brine interacts with the host rock. The interactions include clay swelling for clay-rich rocks, and mineral dissolution and precipitation for carbonate-rich rocks (Gunter et al., 2000; Kaszuba et al., 2005; Rohmer et al., 2016; Yoksoulian et al., 2013). The chemical reaction speed varies depending on the mineralogy of host rock. Chemical reactions between the acidified brine and minerals may alter rock fabric and induce the changes of rock mechanical properties (Major et al., 2013; Espinoza et al., 2018; Rohmer et al., 2016). The alterations in mechanical properties by CO_2 injection may trigger reservoir compaction and disturb formation stress equilibrium at the short and long term (Jung and Espinoza, 2017; Shovkun and Espinoza, 2017; Espinoza et al., 2018).

1.3 OUTLINE OF THE DISSERTATION

The dissertation presents geomechanical analyses for CO_2 sequestration with three main chapters. Chapter 2 shows the quantification of maximum reservoir capacity to avert geomechanical perturbation using Frio CO_2 injection pilot test in Dayton, Texas in 2008 as a case study. Frio CO_2 injection site is compartmentalized with faults and a salt dome, thus suitable for investigating the reservoir capacity with relatively accurate pore pressure buildup within reservoir boundary scale. The study is based on a coupled compositional flow reservoir model (Integrated Parallel Accurate Reservoir Simulator, IPARS) and geomechanical analytical solutions. The compositional flow model enables the

investigation of pore pressure buildup considering effect of CO_2 dissolution into brine. The study includes laboratory experiments and well-logging analysis to estimate reservoir properties and the vertical heterogeneity in detail. The characterized petrophysical and geomechanial properties are implemented to construct an integrated reservoir model with vertical heterogeneity. History-matching based on the integrated reservoir model calculates accurate pore pressure at fault boundaries and injector. Geomechanical analyses help quantify the maximum reservoir capacity using the numerical results of pore pressure by predicting fault reactivation and injector fracturing. The contents of this chapter have been published in [Jung, H., G. Singh, D. N. Espinoza, and M. F. Wheeler. 2017. Quantification of a Maximum Injection Volume of CO_2 without Geomechanical Perturbations Using a Compositional Fluid Flow Reservoir Simulator. *Advances in Water Resources*. Volume 112, Pages 160-169].

Chapter 3 discusses a wellbore injectivity changes and possible injector fracturing during CO_2 injection due to thermo-poro-mechanical effect. The study uses a field data of CO_2 sequestration project in Cranfield, Mississippi as a case study. Unexpected pressure responses and bottom-hole temperature reduction pose a possibility of injector fracturing in Cranfield. The study is based on a reservoir simulation using a coupled thermo-poro-mechanical reservoir simulator (Computer Modeling Group, CMG-GEM). The coupled thermo-poromechanical simulations estimate the stress alteration induced by temperature reduction near injector. A Cranfield reservoir model is built based on well-logs and laboratory core analysis. The reservoir simulation includes vertical heterogeneity in

reservoir properties, and the resulting vertical heterogeneous stress condition. The simulation with heterogeneity investigates the least local minimum principal stress and the risk of local injector fracturing induced by thermo-elastic stress alteration from CO_2 injection. The contents of this chapter have been submitted to the *International Journal of Greenhouse Control* with title of "Wellbore injectivity response to step-rate CO_2 injection: coupled thermo-poro-elastic analysis in a vertically heterogeneous formation" by authors Jung, H., Espinoza, D. N., and Hosseini, S. A.

Chapter 4 shows alterations of rock mechanical properties induced by chemical interactions with CO_2-charged brine in geological time scale. The study is based on laboratory measurements using samples from outcrops of Crystal Geyser field site in Utah. The site shows clear geological evidences of natural CO_2 migration path from source rock. Experiments using the samples from the migration path and off the path are compared to investigate the effect of chemical alterations to rocks. The study examines the chemical effect of CO_2-acidified brine to rock fabrication and mechanical properties both experimentally and numerically. The contents of this chapter can be found in [Espinoza, D. N., Jung, H., Major, J. R., Sun, Z., Ramos, M. J., Eichhubl, P., Balhoff, M. T. Choens, R. C., Dewers, T. A. 2018. CO_2 charged brines changed rock strength and stiffness at Crystal Geyser, Utah: Implications for leaking subsurface CO_2 storage reservoirs. *International Journal of Greenhouse Gas Control*. Volume 73. Pages 16-28].

Finally, Chapter 5 concludes above works and potential research directions for future applications.

Chapter 2

Quantification of a Maximum Injection Volume of CO_2 without Geomechanical Perturbations Using a Compositional Fluid Flow Reservoir Simulator[1]

2.1 INTRODUCTION

Pore pressure prediction and management are crucial for successful development and implementation of CO_2 capture and large-scale geological storage. Field evidence shows that the state of stresses in many sedimentary basins is close to limit equilibrium, and therefore the window for pore pressure alteration –without fault reactivation– is relatively narrow (Zoback and Gorelick, 2002). High injection rates may trigger open-mode fractures. Large injection volumes even with low injection rate over time can reactivate shear fractures and faults in compartmentalized reservoirs (Bjerrum at al., 1972; Economides and Ehlig-Economides, 2010). Previous studies demonstrate that injection of large volumes of water and CO_2 have caused fault reactivation and induced seismicity with magnitude over $M>1$ (Frohlich, 2012; Ellsworth, 2013; Bauer et al., 2016). In-depth understanding of short-term implications of pressure build-up and long-term fate of stored CO_2 requires a comprehensive study of (1) petrophysical and geomechanical properties of the target injection formation, (2) caprock, adjacent faults and reservoir compartmentalization, and (3) multiphase and compositional behavior of CO_2 and resident fluid.

Poorly consolidated sediments are good candidates for CO_2 geological storage due to: (1) relatively large porosity and permeability in sandy intervals, (2) high rock compressibility (or expansivity), and (3) ductile deformational behavior. Fault reactivation does not necessarily imply leakage (Rutqvist, 2016). Ductile rocks tend to self-heal in the event of fracturing and subsequent fracture closure (Bernier et al., 2007; Menaceur et al., 2015). Large sections of the Gulf of Mexico sedimentary basin are comprised by uncemented sediments –including the Frio Formation– that display ductile rather than brittle post-peak behavior (Boswell et al., 2009; Muller et al., 2007; Owen et al., 1987).

The Frio CO_2 injection pilot project injected about 1,600 metric tons of CO_2 in unconsolidated sands of the Frio Formation at a location near Dayton, Texas. The first injection test targeted the upper Frio Formation (Frio "C" brine-bearing Oligocene age sand) in a fault-bounded formation (Hovorka et al., 2004). The formation is adjacent to a salt dome and is located below the highly heterogeneous Anahuac shale (Figure 2.1). The injection well was permitted as a Class V underground injection control experimental well with a maximum of 54,000 tons of cumulative injection and a maximum injection rate 250 tons per day (Hovorka et al., 2003). The first pilot test injected 1,600 metric tons of CO_2 into the formation for ten days with four main injection and shut-in cycles with approximately constant injection rates of 260 tons per day (Hovorka et al., 2004, 2006; Doughty et al., 2008). The pilot test made use of various monitoring techniques and tools such as time-lapse well logs, U-tube sampling, and tracer injection test to diagnose and demonstrate the injection progress and CO_2 plume fate (Sakurai et al., 2006). The second

Frio pilot project was conducted in 2006 and injected 380 tons of CO_2 into a formation 120 m (360 ft) below the first project injection zone at the same injection rate. Monitoring devices did not detect leakage nor induced seismicity from the Frio injection tests (Hovorka et al., 2006; Doughty et al., 2008).
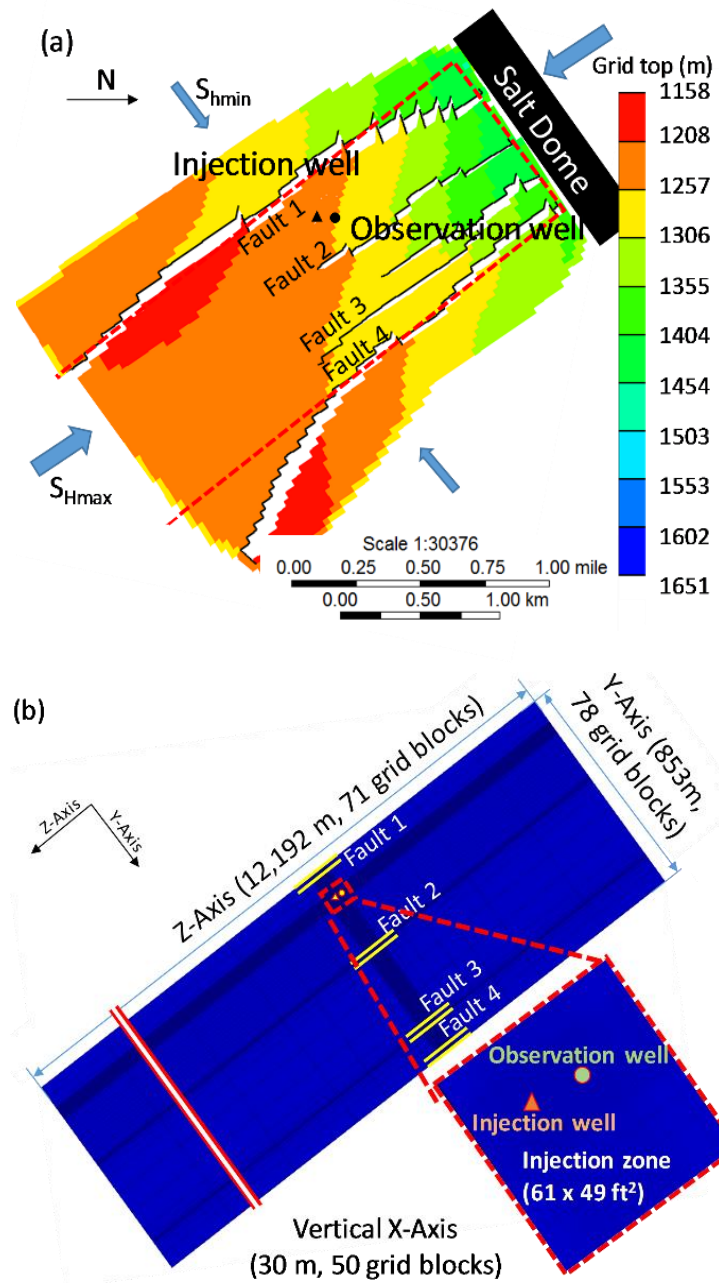
Figure 2.1. (a) Schematic diagram of the Frio aquifer structure (Top view). The dashed red box is the selected region for building a detailed are of study (DAS) model. (b) DAS reservoir model geometry and zoom-in into the grid refinement around the injection zone. Double-yellow lines show the faults locations analyzed in this study.

The purpose of this study is to investigate pore pressure build-up induced by CO_2 injection in heterogeneous and compartmentalized poorly consolidated sands. We utilize the Frio CO_2 project as a case study. The paper starts with a description of the reservoir model, petrophysical and geomechanical properties (based on laboratory experiments and well-logging analyses), and the compositional phase behavior model. Then, we show the results of history matching for the actual injection schedule and extend conclusions for larger injection volumes and rates. We conclude with an evaluation of expected geomechanical perturbations and limits for injection volumes and rates based on the current in-situ state of stress and compartmentalization assumption.

2.2 FRIO I RESERVOIR MODEL

2.2.1 Reservoir Geometry, Boundary Conditions and Simulation Grid

The detailed area of study (DAS) is a subdomain of interest in the larger Frio reservoir which includes injection and observation wells. The DAS boundaries are determined by faults and a salt dome North-West of the reservoir (Figure 2.1-a). The reservoir dips 16° towards the South-East. We adopted no-flow boundary conditions for all four boundaries because reservoirs and aquifers in these relatively ductile formations tend to be compartmentalized. The lower end of the reservoir is idealized as an elongated section of 12 km, long enough to satisfy history-matching under the assumption of compartmentalization (Figure 2.1-b). Fault 2 and 3 are represented by low permeability planes embedded in the middle of the DAS area. All four faults are normal faults having

11

same strike about N45°W but with different dip angles as interpreted from seismic images and earlier developed models (Hovorka et al., 2006) (Table 2.1).

Table 2.1: Information about faults in detailed area of study (DAS).

	Depth (closest to injection well)	Strike	Dip
Fault 1	1,566 m (5,139 ft)	N45°W	87°NE
Fault 2	1,542 m (5,060 ft)	N45°W	77°NE
Fault 3	1,458 m (4,873 ft)	N45°W	77°NE
Fault 4	1,408 m (4,621 ft)	N45°W	78°NE

The total thickness of the model is 30 m (100 ft) evenly divided into 50 grid blocks of 0.6 m (2 ft) perpendicular to bedding in the x-direction. Parallel to the bedding plane, the model is divided into 78 grid blocks in the y-direction (853 m) and 71 grid blocks in the z-direction (12192 m). The injection zone (approximately 49 m by 61 m (160 ft by 200 ft)) is refined parallel to the bedding (y and z-directions) with 1.5 m (5 ft) grid blocks, and the surrounding area is spaced with gradually larger sizes of the blocks from 3 m (10 ft) to 305 m (1,000 ft). The full DAS model has 276,900 degrees of freedom. The well injection schedules replicated the field injection/shut-in schedule. Further the initial reservoir pressure was populated using full observation of base pressure at the injection and observation wells.

2.2.2 Petrophysical and Geomechanical Properties of Frio C Sandstone and In-situ Stresses

Frio C sand is composed of subarkosic fine-grained moderately sorted quartz and feldspar sand grains; with minor amounts of illite, smectite, and calcite (Kharaka et al.

2006). These minor amounts of clay and calcite are located at grain contacts and may effect

dynamic elastic properties (Al Hosni et al., 2016). We obtained petrophysical properties

from laboratory tests courtesy of GCCC and petrophysical and geomechanical properties

from experiments performed in our laboratory. Table 2.2 summarizes specimen depths and

experiments performed.

Table 2.2: Information of samples from laboratory experiments.

Depth [ft]	Depth [m]	Plug direction	Type of experiments	Porosity [-]	Permeability [mD]
5051.8	1539.8	Horizontal	Gas permeability, MICP (GCCC)	0.308	837
5050.4	1539.3	Horizontal	Gas permeability, MICP (GCCC)	0.277	25
5051.2	1539.6	Horizontal	Gas permeability, MICP (GCCC)	0.244	45
5053.4	1540.3	Horizontal	Gas permeability, MICP (GCCC)	0.326	2930
5055.1	1540.8	Vertical (V1)	Multistage triaxial loading, N_2-brine injection at in-situ stress condition (Biot coefficient and compressibility), MICP (Our laboratory)	0.376	263
5055.8	1541.0	Horizontal (H1)	Porous plate capillary pressure measurement (Our laboratory)	0.377	-
5055.9	1541.0	Vertical (V2)	Porous plate capillary pressure measurement (Our laboratory)	0.355	-
5061.4	1542.7	Horizontal	Gas permeability, MICP (GCCC)	0.331	1150
5065.6	1544.0	Horizontal	Gas permeability, MICP (GCCC)	0.327	1830
5070.5	1545.5	Horizontal	Gas permeability, MICP (GCCC)	0.280	212
5071.5	1545.8	Horizontal	Gas permeability, MICP (GCCC)	0.353	2650
5075.4	1547.0	Horizontal	Gas permeability, MICP (GCCC)	0.326	1080
5076.3	1547.3	Horizontal	Gas permeability, MICP (GCCC)	0.340	2330

2.2.2.1 Porosity and Permeability

Experimental measurements as well as well-logging analysis (data courtesy of the

GCCC) provided petrophysical properties and geomechanical properties for populating the

reservoir model. The well-logging data analysis is used to calculate porosity and

permeability from data spaced every 0.15 m (0.5 ft). We corrected measured neutron

porosity ϕ_N and density porosity ϕ_D for the presence of clays according to Equations

(1-2) (Torres-Verdin, 2016).

$$\phi_D^c = \frac{\phi_D - C_{sh}\phi_{D,sh}}{1 - C_{sh}} \qquad \text{(Eq 2.1)}$$

$$\phi_N^c = \frac{\phi_N - C_{sh}\phi_{N,sh}}{1 - C_{sh}} \qquad \text{(Eq 2.2)}$$

where ϕ_D^c and ϕ_N^c are shale-corrected density porosity and neutron porosity, C_{sh} is

volumetric concentration of shale, and $\phi_{D,sh}$ and $\phi_{N,sh}$ are apparent density porosity and

neutron porosity of pure shale. The selected depths for the shale correction are 1516 m

(4972.5 ft) for the clay-rich layer (local maximum GR) and 1544 m (5065.5 ft) for the

water saturated clay-poor layer (local minimum GR). Table 2.3 shows the well log GR

readings at the two depths. The corrected porosity ϕ_S^c is

$$\phi_S^c = \sqrt{\frac{\left(\phi_D^c\right)^2 + \left(\phi_N^c\right)^2}{2}} \qquad \text{(Eq 2.3)}$$

We calculated permeability along the entire injection zone using an empirical

correlation between laboratory measured porosity ϕ and permeability k (Figure 2.2 -

Ghomian 2008). Figure 2.3 shows the resulting corrected porosity and permeability

including layers above and below the injection zone. Reservoir properties were averaged

arithmetically from the calculated data; namely the grid block spatial scale is 0.6 m (2 ft)

– see Figures 2.3-a and b for interpolated values of porosity and permeability. We adjusted

the ratio between vertical and horizontal permeabilities to 1/3 in order to achieve history

matching in the pressure response. Hovorka et al. (2006) applied 1/10 for the reservoir

permeability anisotropy ratio. However, our fine vertical discretization of 2 ft allows us to handle directly vertical heterogeneity. Frio C sandstone core photos and CT images exhibit weak lamination in the perforation interval 1543.2–1548.4 m (5053–5070 ft). Strong laminations appear below the perforation depth at a scale of less than ~2 cm. We did not account for variation of permeability and porosity in horizontal direction because of limited information (available just from one well).

Table 2.3: Measured well log values at depths for shale correction

Property	Water saturated sands	Clay-rich sands
Depth [m]	1,544 m (5065.5 ft)	1,516 m (4,972.5 ft)
Gamma ray [GAPI]	45.5	148.9
Density porosity $\phi_{D,sh}$ [-]	0.354	0.260
Neutron porosity $\phi_{N,sh}$ [-]	0.348	0.501
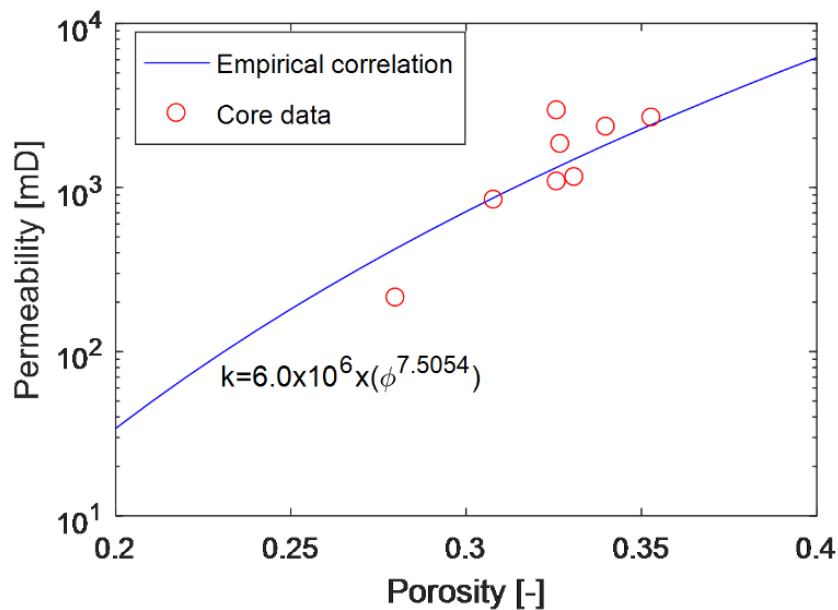
Figure 2.2 Porosity and permeability empirical relationship from core measurements.
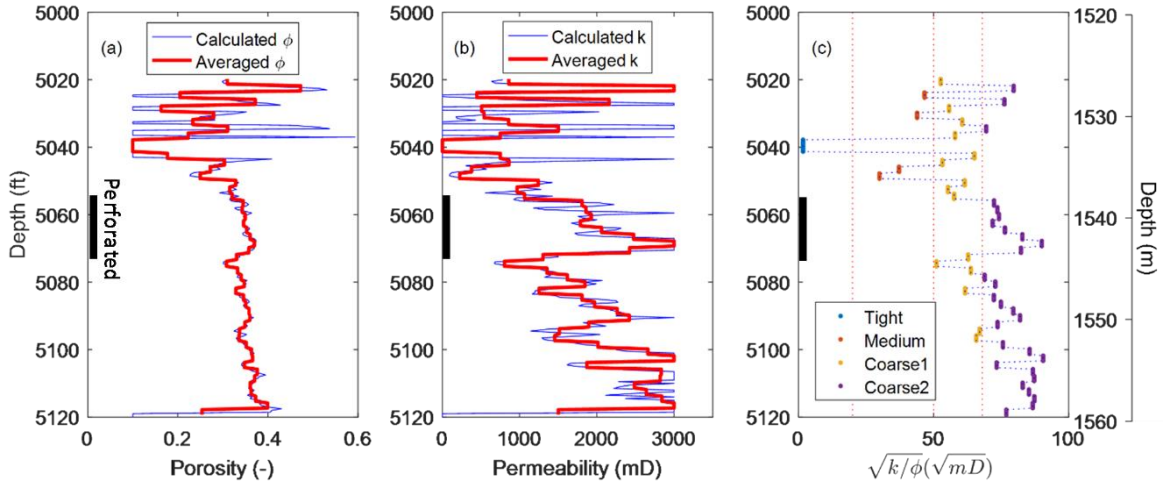
Figure 2.3 (a) Porosity, (b) permeability, and (c) ratio $\sqrt{k/\phi}$ around the injection well as a function of measured depth: calculated from well-logs (blue line), adopted in model (red line).

2.2.2.2 Capillary Pressure and Relative Permeability

Capillary pressure measurements from MICP tests of 10 cores from Frio sand suggest that the layered formation can be categorized into different sand groups depending on the values of the J-function:

$$J(S_w) = \frac{P_c(S_w)}{\gamma \cos\theta} \sqrt{\frac{k}{\phi}} \qquad\qquad\qquad (\text{Eq 2.4})$$

where S_w is saturation of water, P_c is capillary pressure, γ is interfacial tension, and θ is contact angle (Peters, 2012). We used the J-functions to classify the full reservoir model into four different rock types to build an accurate reservoir model (Table 2.4). Figure 2.4-b shows the capillary pressure converted from J-functions measured with an air-mercury system (interfacial tension at 485 mN/m and contact angle 140°) to CO_2-brine system (interfacial tension 30 mN/m and contact angle 40° - Espinoza and Santamarina, 2010).

16

We employed a Brooks-Corey drainage model to calculate the relative permeability curves from capillary pressure data (Figure 2.4-b and -c). We utilized relative permeability curves from drainage process only.

$$P_c = P_e (S_w^*)^{-\frac{1}{\lambda}} \tag{Eq 2.5}$$

$$S_w^* = \frac{S_w - S_{wirr}}{1 - S_{wirr}} \tag{Eq 2.6}$$

where P_e is the capillary entry pressure, S_w^* is the reduced wetting phase saturation, λ is the pore size distribution index, and S_{wirr} is irreducible water saturation. The corresponding relative permeabilities are

$$k_{rw}(S_w) = (S_w^*)^{\frac{2+3\lambda}{\lambda}} \tag{Eq 2.7}$$

$$k_{rnw}(S_w) = k_{nwr} \left(1 - \frac{S_w - S_{wirr}}{S_m - S_{wirr}}\right)^2 \left[1 - (S_w^*)^{\frac{2+\lambda}{\lambda}}\right] \tag{Eq 2.8}$$

where k_{rw} is the relative permeability of wetting phase (brine), k_{rnw} is the relative permeability of non-wetting phase (CO_2), S_m (= 1 for drainage) is the wetting phase saturation corresponding to the critical non-wetting phase saturation, and k_{nwr} is the non-wetting phase relative permeability at the irreducible wetting phase saturation and assumed to be 0.45 for tight rock, 0.82 for medium rock, and 0.9 and 0.95 for coarser rock adjusted from Ghomian (2008). Table 2.4 lists the modelling parameters used to calculate the relative permeability curves (Figure 2.4-c). The reservoir model adopts heterogeneity of capillary pressure and relative permeability as shown in Figure 2.4-c.

Table 2.4: Rock types applied to Frio reservoir modeling for capillary pressure and relative permeability. (Assumed parameter includes Sm = 1)

Property	Tight	Medium	Coarse 1	Coarse 2
Permeability [mD]	0.3	618	1026	2107
Porosity [-]	0.1	0.24	0.29	0.36
J-function	1	2	3	3
λ	0.29	1.1	2	1.9
P_e [MPa]	0.0055	0.0021	0.0028	0.0016
S_{wirr}	0.5	0.279	0.263	0.263
k_{nwr}	0.45	0.8	0.9	0.95
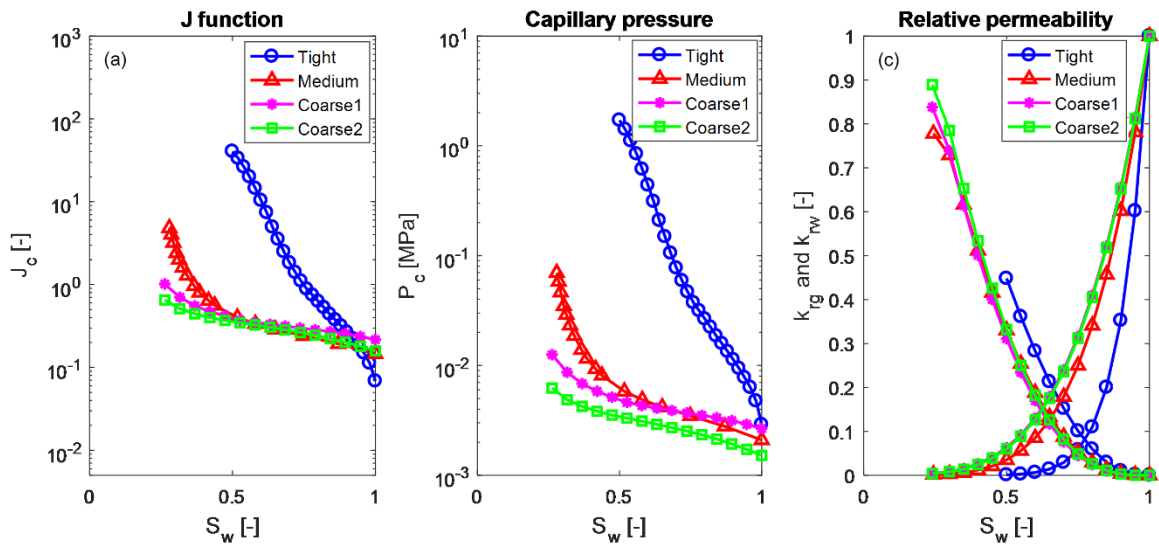
Figure 2.4. (a) J-function, (b) capillary pressure, and (c) relative permeability of four rock types applied into the reservoir model.

2.2.2.3 Geomechanical Properties

We saturated sample V1 with synthetic 93,000 ppm salinity NaCl solution as pore fluid and measured volumetric strain as a function of effective mean stress (Figure 2.5-b). The confining pressure was controlled by fixing a pressure rate of 6.89 kPa/s at 1.37 MPa of deviatoric stress. The corresponding unloading bulk rock compressibility is $9.6 \cdot 10^{-4}$ MPa^{-1} ($6.6 \cdot 10^{-6}$ psi^{-1}) evaluated using the following equation:

$$C_p = \frac{1}{V_p}\frac{\Delta V_p}{\Delta P_p} \cong \frac{\Delta \varepsilon_{vol}}{\Delta P_p} \tag{Eq 2.9}$$

We quantified Frio sand rock Biot coefficient using step loading of pore pressure and confining stress (Guéguen and Bouteca, 1999). Figure 2.5(b) shows the effective mean stress as a function of volumetric strain. The data collapses in a single line for the right Biot coefficient. The compressibility for uni-axial strain condition, usually more appropriate for reservoir stress paths, tends to be larger than the bulk compressibility (Dudley, et al., 2016). The model assumes constant rock compressibility throughout the reservoir.
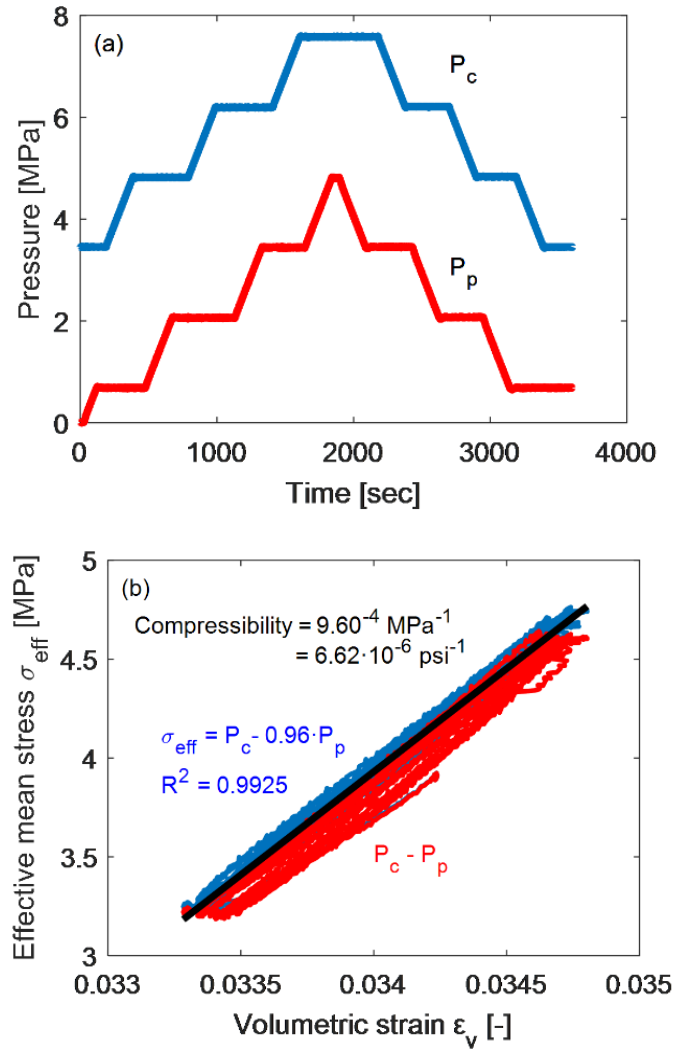
Figure 2.5. Results of pore pressure and confining stress loading and unloading on Frio sand: (a) loading paths of pore pressure P_p and confining stress P_c (b) volumetric strain change as a function of effective mean stress. The resulting Biot coefficient is 0.96 and bulk compressibility is 6.62×10^{-6} psi.

We also conducted a multistage deviatoric loading test to evaluate strength and post-peak failure behavior of the Frio C sand. The multistage loading consisted of increasing deviatoric stress at three different constant confining stresses: 3.4 MPa (500 psi), 6.9 MPa (1,000 psi), and 10.3 MPa (1,500 psi) (Figure 2.6-a). During the first two

loading stages, the sample was loaded until the onset of dilative behavior by increasing

deviatoric stress. The last loading stage went into shear yield. The sand resulting friction

angle is about 38º, and the cohesive strength is zero (Figure 2.6-b). The sand undergoes

ductile deformation at peak stress.
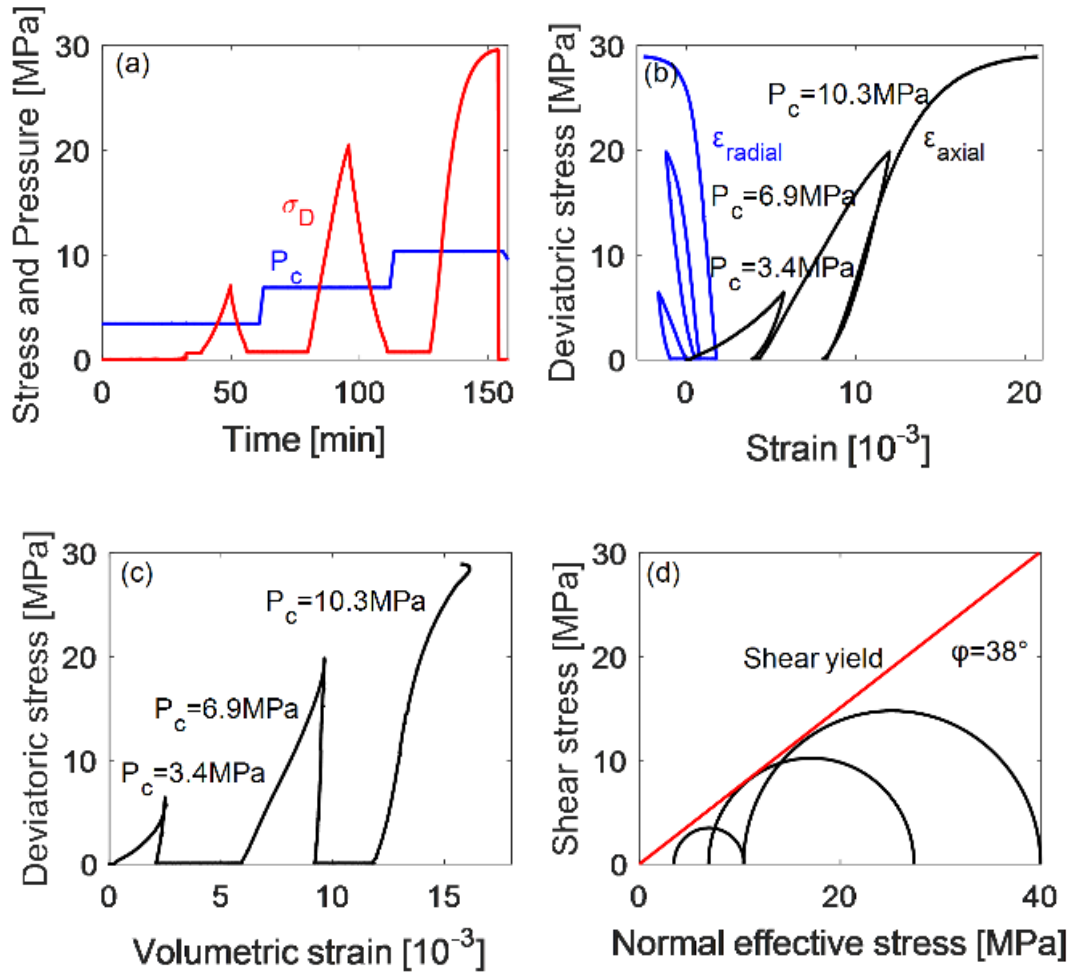
Figure 2.6 Results of multistage triaxial loading on Frio sand at confining stress 3.4 MPa, 6.9 MPa and 10.3 MPa: (a) loading path of the test, (b) deviatoric stress as a function of axial and radial strains, (c) deviatoric stress as a function of volumetric strain, and (d) Mohr-Coulomb shear yield line.

2.2.2.4 In-situ Stresses

We estimated the magnitude and direction of principal stresses using an overburden (total vertical stress) gradient of 20.5 MPa/km (0.907 psi/ft) (Hovorka et al., 2003) and considered the effect of the rising salt dome on "dome hoop stresses" (minimum principal stress oriented in circumferential direction - Nikolinakou et al., 2014). We assumed limit frictional equilibrium in the sand unit (Zoback, 2007), a friction angle for Frio sand from Section 2.2, and a normal faulting regime from the seismic interpretation of strikes and dips of the respective faults (Figure 2.1 and Table 2.1). At limit frictional equilibrium between vertical and horizontal stress, the friction angle φ dictates the vertical-to-horizontal effective stress anisotropy:

$$\frac{\sigma_1}{\sigma_3} = \frac{S_v - P_p}{S_{hmin} - P_p} \leq \frac{1 + sin(\varphi)}{1 - sin(\varphi)} \tag{Eq 2.10}$$

where σ_1 and σ_3 are maximum and minimum principal effective stress, S_v is the total vertical stress, S_{hmin} is the minimum total horizontal stress, and P_p is the pore pressure. This estimation computes a lower bound for S_{hmin}.

At the perforation depth 1540 m–1546 m (5053 ft–5071 ft) of the injection well, measured bottomhole pressure P_p was 14.8 MPa (2153 psi), and calculated S_v is 31.6 MPa (4580.4 psi). Using $\varphi = 38°$ (Figure 2.6), Eq. 10 provides a lower bound estimate of minimum principal total stress equal to 18.8 MPa (2,734 psi). Stress anisotropy may decrease with time due to visco-elastic stress relaxation (Sone and Zoback 2014a, 2014b). We utilize the calculated minimum horizontal stress and vertical stress to estimate the

possibility of fault reactivation and fracture opening upon pore pressure change but did not intend to calculate the intermediate stress S_{Hmax}.

Hovorka et al. (2003) calculated formation fracture pressure equal to 26.6 MPa (3,851 psi) at a depth of 1,527 m (5,000 ft) based on Eaton's equation using Poisson's ratio $v = 0.416$, overburden gradient 0.907 psi/ft, and reservoir pressure gradient 0.432 psi/ft:

$$S_{hmin} = \left(\frac{v}{1-v}\right)(S_v - P_p) + P_p \qquad \text{(Eq 2.11)}.$$

2.2.3 Reservoir Simulator

2.2.3.1 Simulation Methodology

The compositional flow model in IPARS uses the Peng-Robinson cubic equation of state (PR-EOS) for describing fluid phase behavior. The conservation equations for each component (Equations 12-13) are discretized in time using the backward Euler scheme resulting in a fully implicit system in pressure and concentration unknowns. A lowest order mixed finite element method (equivalent to cell-centered finite differences) was used for the spatial discretization. The component concentration equations can be written as,

$$\frac{\partial}{\partial t}(\phi N_i) + \nabla \cdot \vec{F_i} - \nabla \cdot \left(\sum_\alpha \phi S_\alpha \mathbf{D_{i\alpha}}(\nabla \rho_\alpha x_{i\alpha})\right) = q_i \qquad \text{(Eq 2.12)}$$

$$\vec{F_i} = -\mathbf{K} \wedge_i \left(\nabla P_{ref} - \frac{1}{\wedge_i}\sum_\alpha \rho_\alpha x_{i\alpha}\frac{k_{r\alpha}}{\mu_\alpha}\rho_{m,\alpha}\vec{g} + \frac{1}{\wedge_i}\sum_{\alpha \neq ref}\rho_\alpha x_{i\alpha}\frac{k_{r\alpha}}{\mu_\alpha}\nabla P_{c\alpha}\right)$$

$$\text{(Eq 2.13)}$$

where $\wedge_i = \sum_\alpha \rho_\alpha x_{i\alpha}\frac{k_{r\alpha}}{\mu_\alpha}$ is the mobility, $N_i = \sum_\alpha \rho_\alpha S_\alpha x_{i\alpha}$ is the concentration, $q_i = \sum_\alpha q_{i\alpha}$ is the injection/production rate, $\vec{F_i}$ is the flux vector of component i, S_α is

saturation of phase α, $\boldsymbol{D_{i\alpha}}$ is diffusion coefficient tensor, $x_{i\alpha}$ is mole fraction of component i in phase α, $\boldsymbol{K}$ is permeability tensor, P_{ref} is reference pressure, $\rho_{m,\alpha}$ is mass density, and $P_{c\alpha}$ is capillary pressure of phase α, and $\vec{g}$ is the gravity vector (Singh and Wheeler, 2016). The phase equilibrium is calculated using the Rachford-Rice equation (Rachford-Rice, 1952) and iso-fugacity criteria. Further details regarding the compositional flow formulation, phase behavior model, and numerical solution scheme can be found in Singh and Wheeler (2016).

IPARS compositional flow module has been used extensively for evaluating various sequestration and gas injection scenarios (Delshad et al., 2011; Kong et al., 2015). Although the PR-EOS is developed for non-polar molecules such as hydrocarbons, IPARS allows water phase properties to be calculated using PR-EOS. This is achieved by modifying the binary interaction parameters (BIP) for the components. In this study, we used two components (CO_2 and brine) and tuned the BIPs of the PR-EOS to match experimentally observed solubility of CO_2 in brine. Table 2.5 shows the EOS parameters used in this study. The calculations further assume CO_2 and brine as chemical components wherein the CO_2 component can exist in both gaseous and aqueous phases. The brine component is considered to exist only in the liquid phase. We considered two approaches for studying CO_2 migration (discussed in detail in Section 3.4). The partially miscible case uses PR-EOS for calculating both gas and aqueous phase properties. The immiscible case uses PR-EOS and slightly compressible approach for gas and aqueous phase, respectively.

A tensor product refinement was used to better capture changes in the DAS, where the injection and observation wells are located. This approach is especially useful when limited amount of reservoir properties are available from well logs, seismic observations and geological models for detailed calculation near the injector. Although the numerical simulation model used tensor product refinements, current IPARS capabilities allow computationally efficient local adaptive mesh refinement for long term evaluation of multiple sequestration scenarios.

Table 2.5: EOS parameters for CO_2 and brine flow calculation.

	T_c [R°]	P_c [psi]	Z_c	ω[-]	M_w [g/mol]	P [-]	V_{shift} [-]	BIC
CO_2	547.56	1070.38	0.3023	0.2240	44.01	78.0	0.0247	-0.0602
Brine	1165.23	3203.88	0.2298	0.2240	19.35	52.0	0.2340	-0.0602

2.2.3.2 Simulation Description

Reservoir simulation included various cases (Table 2.6):

- Baseline scenario: history match case (BC), partially miscible,

- Immiscible flooding case to compare with baseline scenario (IM), and

- Sensitivity analysis cases varying injection rates (IR), both partially miscible and

  immiscible.

We performed history matching with the model described in Sections 2.1 and 2.2. The initial pressure was determined using equilibrium calculation as preprocessing step. The binary interaction coefficient for brine and CO_2 ($BIC_{H_2O-CO_2}$) interaction was evaluated according to the relationship introduced by Kong et al. (2013),

$$BIC_{H_2O-CO_2} = -0.093625 + [4.861 \cdot 10^{-4}(T - 113)] + (2.29 \cdot 10^{-7}S) \quad (14)$$

where T is temperature (°F), and S is salinity (ppm). The binary coefficient was calcualted

to be -0.06212 at a reservoir, temperature of 134 °F (56.7 °C) and brine salinity of 93,000

ppm. We assumed constant reservoir temperature in simulations.

The objective of CO_2 injection simulations was to quantify the maximum injection volume

required for the fluid pressure to reactivate faults or fracture the injector. We examined the

effect of CO_2 solubility on pore pressure build-up computing the immiscible and miscible

scenario described above.

Table 2.6: Simulation input settings (miscibility and well schedule) varied in simulations.

	BC	IM	IR1	IR2	IR3	IR4	IR5	IR6	IR7	IR8
Miscibility	Partially miscible	Immiscible			Partially miscible and immiscible					
Injection rate (ton/day)	Field data	Field data	200	500	1,000	2,000	5,000	10,000	20,000	30,000

2.3 RESULTS AND DISCUSSION

2.3.1 History-Match

Figure 2.7 shows history-matching of pressure responses for four injection cycles

in the base case, including injection and shut-in periods for both the injection and

observation wells. The pressure response in the first injection cycle does not coincide with

simulation results. This peak might have occurred due to effects of formation damage or

near-wellbore perforation complexity. The CO_2 breakthrough time predicted by the

numerical simulation was 2.3 days, compared to 2.1 days observed in the field.
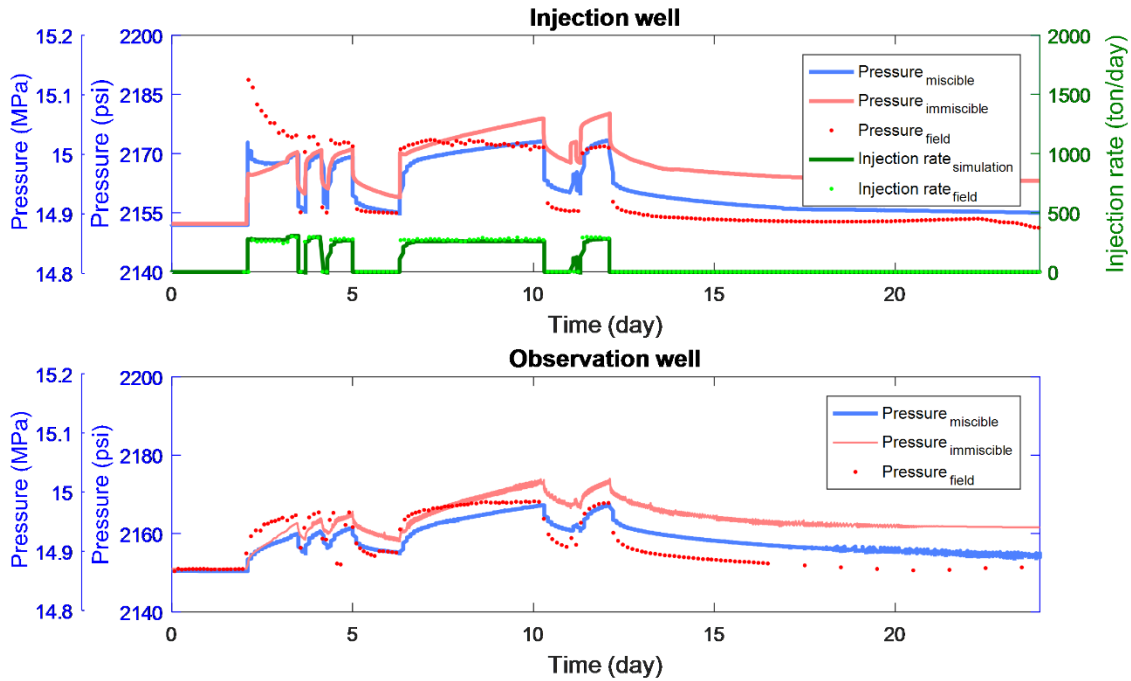
Figure 2.7 Injection rate and the bottom-hole pressure response at the injection well of Frio field and history matched simulation results.

Figure 2.8 shows snapshots of the CO_2 plume migration up to 60 days after injection. The CO_2 plume moves toward the observation well due to buoyancy but does not cross low permeability layers. Figure 2.8-a shows the total CO_2 concentration (CO_2 [lb-mole]/pore volume [ft^3]) in both gas phase and dissolved phase while Figure 2.8-b shows CO_2 saturation of the gas phase only (bulk supercritical CO_2). Initially, the two figures show similar CO_2 saturation distribution since the CO_2 has not dissolved extensively into brine yet. After 30 days of the injection, the difference between Figures 2.8-a and -b demonstrates a considerable amount of dissolved CO_2 around injection zone (approximately 30%).

27
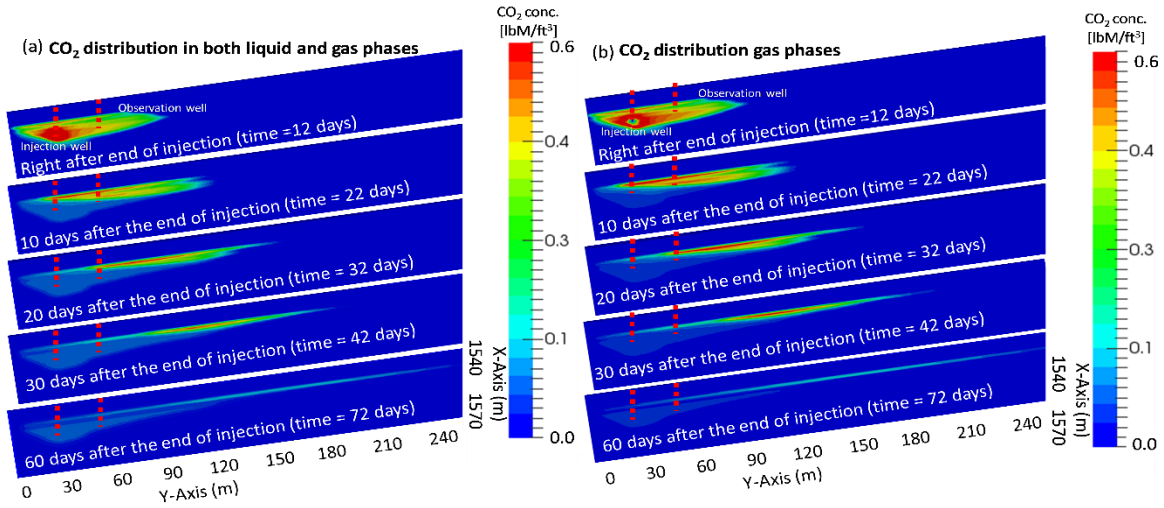
Figure 2.8 History-matched simulation: (a) CO_2 amount in bulk conditions and dissolved, and (b) CO_2 amount in bulk conditions along a cross section passing by the injection and observation wells. Dissolved amount per unit volume is < ~0.1 lb-mole/ft³ CO_2 = 1.6 mole/L CO_2.

2.3.2 Injection Rate to Induce Fault Reactivation

This section applied results of reservoir simulation to determine critical pore pressures and injection rates for fault reactivation. The principal stresses at each fault are calculated as a function of depth (Table 2.1 and Figure 2.9). The stress tensor in geographical coordinates S_g is obtained by applying a transformation matrix R_1 to the principal stress tensor.

$$S_g = R_1^T S R_1 = R_1^T \begin{bmatrix} S_1 & 0 & 0 \\ 0 & S_2 & 0 \\ 0 & 0 & S_3 \end{bmatrix} R_1 \qquad \text{(Eq 2.15)},$$

,where

$$R_1 = \begin{bmatrix} cos\,a\,cos\,b & sin\,a\,cos\,b & -sin\,b \\ cos\,a\,sin\,b\,sin\,c - sin\,a\,cos\,c & sin\,a\,sin\,b\,sin\,c + cos\,a\,cos\,c & cos\,b\,sin\,c \\ cos\,a\,sin\,b\,cos\,c + sin\,a\,sin\,c & sin\,a\,sin\,b\,cos\,c - cos\,a\,sin\,c & cos\,b\,cos\,c \end{bmatrix}$$

$$\text{(Eq 2.16)},$$

28

and Euler rotation angles $a = 44.85°$, $b = 90°$, and $c = 0°$ for the location shown in Figure 1 (Zoback, 2007). Then, we calculate the magnitudes of shear stress τ and normal stress S_n on the fault plane from the projection of S_g, using the respective fault strikes and dip transformation vectors n_n and n_d, (function of fault strike str and dip dip).

$$\tau = \{S_g[n_n]\}^T n_d = \left\{ S_g \begin{bmatrix} -\sin(str)\sin(dip) \\ \cos(str)\sin(dip) \\ -\cos(dip) \end{bmatrix} \right\}^T \begin{bmatrix} -\sin(str)\cos(dip) \\ \cos(str)\cos(dip) \\ \sin(dip) \end{bmatrix}$$

(Eq 2.17),

$$S_n = \{S_g[n_n]\}^T n_n = \left\{ S_g \begin{bmatrix} -\sin(str)\sin(dip) \\ \cos(str)\sin(dip) \\ -\cos(dip) \end{bmatrix} \right\}^T \begin{bmatrix} -\sin(str)\sin(dip) \\ \cos(str)\sin(dip) \\ -\cos(dip) \end{bmatrix}$$

(Eq 2.18),

Figure 2.9 shows the stress conditions at each fault at the initial pore and stress - before injection and calculated following procedure in Section 2.2.4- and at fault reactivation. The values of principal stresses change depending on the depth. The Mohr circles are close to the failure criterion and represent the state of stress in the sand layer. The failure line represents the yield limit of the entire fault across several layers. Fault reactivation requires $\tau/\sigma_n > \mu$ at prescribed fault orientation. Fluid injection and decrease of effective stresses may cause shearing in the sand interval but not necessarily fault reactivation along the entire fracture plane that connects sand and shale intervals. We adopted this simplification to account for fault orientation in the analysis.
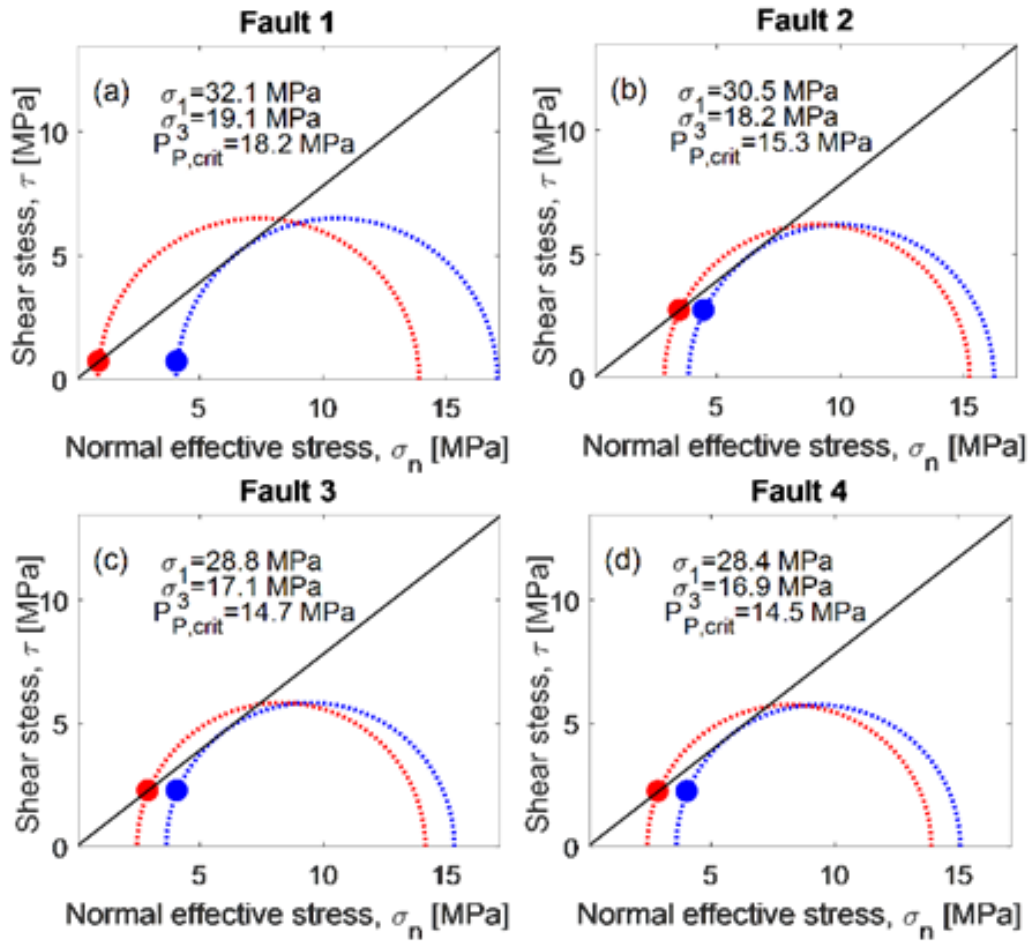
Figure 2.9 Effective stress Mohr circle at initial pore pressure. Circle (initial, blue and critical, red) shows the state of stress at Fault 1 (a), Fault 2 (b), Fault 3 (c), and Fault 4 (d). In-situ stresses are assumed based on stress limit equilibrium. Results illustrate the effect of pore pressure increase at faults inclined at a non-critical angle.

Figure 2.10 shows the maximum amount of CO_2 injection without causing fault reactivation as a function of injection rate. The maximum cumulative amount of CO_2 injection is about 100,000 tons, and the amount is dependent of injection rate through a power law relationship. The first location of fault reactivation is Fault 2 for all injection

rate cases (Table 2.7). Extremely high injection rates over 10,000 tons/day may fracture the well before causing fault reactivation.
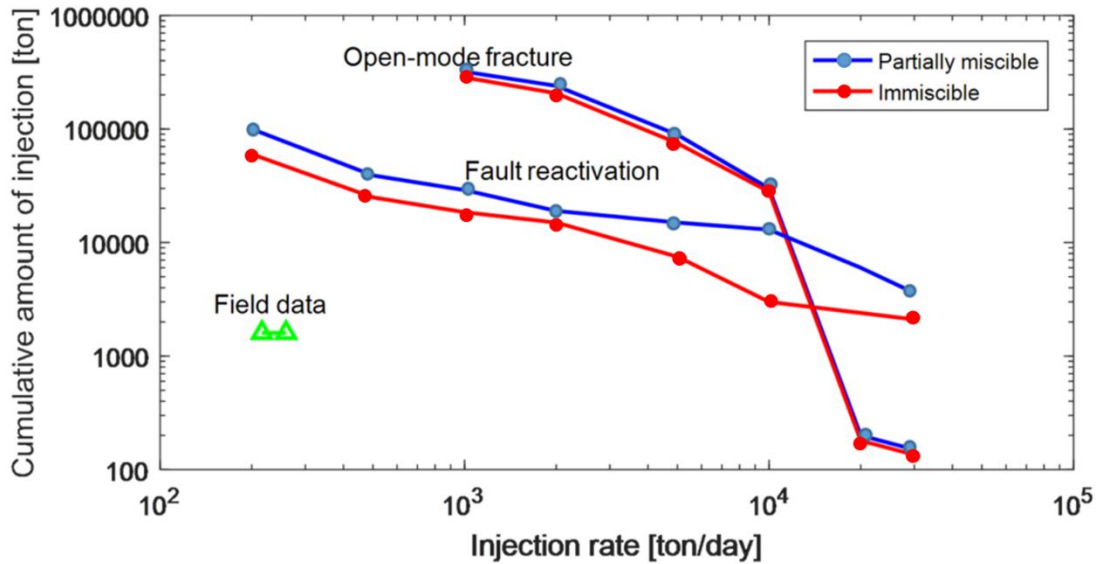
Figure 2.10 Cumulative amounts of CO_2 injection at the limit of fault reactivation and hydraulic fracturing at the injector as a function of injection rate assuming perfect compartmentalization. Blue and red lines indicate partially miscible and immiscible cases. Green triangles show actual cumulative CO_2 injection volume and injection rates attained in the field during the first Frio pilot test.

Table 2.7: Pore pressure at injection well and nearby faults for different injection rates (constant) and elapsed time to reach fault reactivation (marked with *) assuming compartmentalization. Injector fracturing is marked with **.

Injection rate (ton/day)	Time after beginning of injection (days)	Pore pressure at injection well and faults [MPa]				
		Injection well	Fault 1	Fault 2	Fault 3	Fault 4
200	650	15.8	16.0	15.3*	14.5	14.3
500	113	15.9	16.1	15.3*	14.5	14.3
1,000	36	16.0	16.1	15.3*	14.4	14.2
2,000	12	16.2	16.2	15.3*	14.3	14.1
5,000	3.05	16.7	16.5	15.3*	14.1	13.8
10,000	1.1	17.5	16.9	15.3*	13.8	13.6
20,000	0.5	18.5**	17.2	15.3*	13.5	13.3
30,000	0.19	20.3**	18.0	15.3*	13.4	13.3

Overall, the results indicate that the first Frio pilot test injected less than 1.6% of the maximum possible amount of CO_2 storage without perturbing faults (Figure 2.10). Assumption of negligible rock compressibility results in a reduction of storage capacity by a factor of ten. These values are provided as an illustrative comparison for compartmentalized reservoirs in formations near the limit of stress equilibrium. Actual predictions need to measure in-situ stress magnitude and orientation and should account for flow boundary conditions that may allow for leaks at faults.

Tertiary unconsolidated sands and mudrocks at Frio do not exhibit brittle deformation during shearing. Figure 2.6-a shows slight strain hardening behavior of Frio sand at in-situ effective stresses. Large induced seismicity events and failure localization (and local increases in permeability) are less likely to occur in geological formations that sustain large plastic strains at yield.

2.3.3 Injection Rate to Induce Open-Mode Fractures

Figure 2.10 summarizes simulation results showing the maximum amounts of CO_2 injection needed to fracture the injection well (assuming that bottom-hole pressure reaches the minimum principal stress) and zero fault leakage upon reactivation. If faults allow for leaks, then an open-mode fracture may not develop due to the pore pressure control at faults. Based on the results, continuing injection of CO_2 at lower injection rates (below 10,000 tons per day) may cause fault reactivation first rather than an open-mode fracture. Once the fault reactivates, the reservoir may not be compartmentalized anymore and an open-mode fracture may not occur at all. Injection rates above 10,000 tons per day can cause hydraulic fracturing before fault reactivation and are not affected by domain size because of the sharp pressure gradient developed around the injection wellbore (Table 2.7). Hovorka et al. (2003) suggested a maximum injection rate of 250 tons per day. Injection pressure and rate used at the first Frio pilot test seems to be significantly below thresholds for developing open-mode fractures.

2.3.4 Pore Pressure Reduction Due to CO_2 Dissolution into Brine

The immiscible two-phase fluid flow simulation (Simulation IM) shows 75.9 kPa (11 psi) higher pressure response compared to compositional simulation (Simulation BC) due to no dissolution of CO_2 into the brine (Figure 2.7). The amount of dissolved CO_2 in Simulation BC increases with time as the plume spreads in the brine-saturated reservoir. The binary interaction coefficient, one of the key parameters for CO_2 solubility in brine, has large effects on the pore pressure for a given injection scenario. At the end of injection,

33

approximately 20% of the CO_2 was dissolved in the brine. After 20 days of the end of injection, 44% of the injected CO_2 was dissolved into the brine, and eventually, 91% of the CO_2 was dissolved after 95 days in the entire reservoir (i.e., just 9% of injected CO_2 remained in bulk phase - CO_2 solubility in Frio brine is about 1.6 mol/L) (Figure 2.8). The CO_2 plume in immiscible simulations (IM) is thinner and moves faster than in the history match simulation (BC). Results indicate that CO_2 dissolution contributes a fair proportion to trapping for small CO_2 injection volumes. CO_2 dissolution in the brine phase alleviates pore pressure buildup and extends injection times without affecting mechanical stability compared to the immiscible case (Figure 2.10). Based on simulation with extended range of injection rate and volume, we predict that injection could have been carried out for an additional 200 days at 200 tons per day. The amount of CO_2 injection considering dissolution is 20% to 60% higher than the amount assuming immiscible conditions for various injection rates. The effect of dissolution on pore pressure buildup is stronger in rocks with low pore compressibility.

2.3.5 Pore Pressure Reduction due to Rock Volumetric Deformation

Rock compressibility C_p is one of the key mechanical properties determining pore pressure buildup. Non-zero rock compressibility or "expandability" allows pore space expansion and relieves the pore pressure buildup at the injection well. Zero-rock compressibility results in a steady increase of wellbore pressure for rate specified injection well. In fact, the pressure buildup is twice for zero rock compressibility compared to the field observations at both injection and observation wells. Our simulation results show

flattening pressure transient curve during constant injection rate using the rock compressibility estimated from the laboratory. Accurate compressibility calculations are critically important to reduce uncertainty in predictions of pore pressure build-up and potential geomechanical events.

2.4 CONCLUSIONS

In this study, we investigated the geomechanical implications of injecting CO_2 in a fault-bounded reservoir comprised by tertiary sediments. We used the Frio pilot CO_2 sequestration project as a case study and matched field data. We also predicted long-term storage feasibility by means of numerical simulation. The history-matched simulation was used as the base case to conduct injection rate sensitivity studies in order to predict thresholds for geomechanical perturbations. Simulations results show that:

- The history-matched simulation shows a considerable amount of dissolved CO_2 in brine for a hundred days after the injection was completed. CO_2 dissolution into brine reduce tens-of-psi pore pressure buildup and result in 91% trapping after 95 days for an injection of 1,600 tons of CO_2 in the first Frio pilot project.

- Simulations using a large range of injection rates show that fault reactivation is likely to occur after the injection of about 100,000 tons assuming perfect compartmentalization (sixty times of the amount injected at the first Frio Pilot project). The actual amount of injection for fault reactivation would depend on accurately determined in-situ stresses and flow boundary conditions. Storage volume decreases with injection rate following a power law relationship.

35

- High reservoir permeability, high rock/pore compressibility, and low CO_2 viscosity render hydraulic fracturing of the injector unlikely. Pore pressure build-up transfers quickly to neighboring faults for injection rates smaller than ~10,000 tons/day.

- The deformational behavior of the tested unconsolidated sediments at yield shear stresses tends to be ductile rather than brittle and may not create significant seismic events or localize channels of high permeability upon fault reactivation.

Chapter 3

Wellbore injectivity response to step-rate CO_2 injection: coupled thermo-poro-elastic analysis in a vertically heterogeneous formation[1]

3.1 INTRODUCTION

Geological sequestration of carbon dioxide (CO_2) can potentially alleviate carbon emissions to the atmosphere by injecting CO_2 into depleted reservoirs and brine formations (IPCC, 2005; Benson & Surles, 2006; Benson & Cole, 2008). However, injecting large amounts of CO_2 at high injection rates in the subsurface may disturb the geomechanical equilibrium of the host formation and lead to fault shear reactivation or open-mode fractures (Rinaldi and Rutqvist, 2013; Bauer et al., 2016; Rutqvist et al., 2016). Predicting the evolution of the state of stress upon CO_2 injection is a complex problem that includes thermo-elastic, poro-elastic, and chemo-elastic coupled processes (Espinoza et al, 2011; Zoback and Gorelick, 2012; Kim and Hosseini, 2013 & 2017). CO_2 injection increases reservoir pore pressure and alters local stress with alterations that depend on formation capacity, compressibility, size, permeability, and aquifer connectivity among others (Economides and Ehlig-Economides, 2010; Jung et al., 2017). Further, injecting fluids at ambient temperature (on surface) into a reservoir at high temperature results in rock shrinkage and effective stress reduction (Luo and Bryant, 2011; Gor and Prevost, 2013). CO_2 injection also results in acidification of the host formation brine, process that may induce mineral dissolution and lower the rock strength (Hangx et al., 2012; Aman et al.,

2017; Jung and Espinoza, 2017; Espinoza et al., 2018). These mechanisms may alter the geomechanical equilibrium and induce inelastic strains in the reservoir.

The Cranfield reservoir in Mississippi, USA implemented CO_2 injection for enhanced oil recovery and carbon sequestration (Hovorka et al., 2013). A total of 0.5 million tons of CO_2 were injected in the water leg solely for carbon sequestration (Southeast Regional Carbon Sequestration Partnership – www.secarbon.org). We call this section of the formation the Detailed Area of Study (DAS) in this paper (Figure 3.1). The DAS area includes one injector (CFU31F-1) and two observation wells (CFU31F-2 and CFU31F-3) perforated at the interval of the Tuscaloosa sandstone (Hovorka et al., 2013; Lu et al., 2012). During the injection in the DAS, the CO_2 injection rate was initialized from 0 to 175 kg/min and then ramped up twice, from 175 to 300 kg/min and then from 300 to 500 kg/min (Soltanian et al., 2016). Even though the injection rate was nearly doubled during the second injection rate change, the injection well did not experience an increase in bottom-hole pressure (BHP), as expected from typical step-rate tests and confirmed by reservoir simulation (Figure 3.2 & Kim and Hosseini, 2013; Soltanian et al., 2016). The field observations of BHP suggest the development of an open-mode fracture, after injection rate was ramped to 500 kg/min (Kim and Hosseini, 2013; Soltanian et al., 2016) and permeability modification (Delshad et al. 2013; Min et al., 2017) in the near-wellbore region during injection.
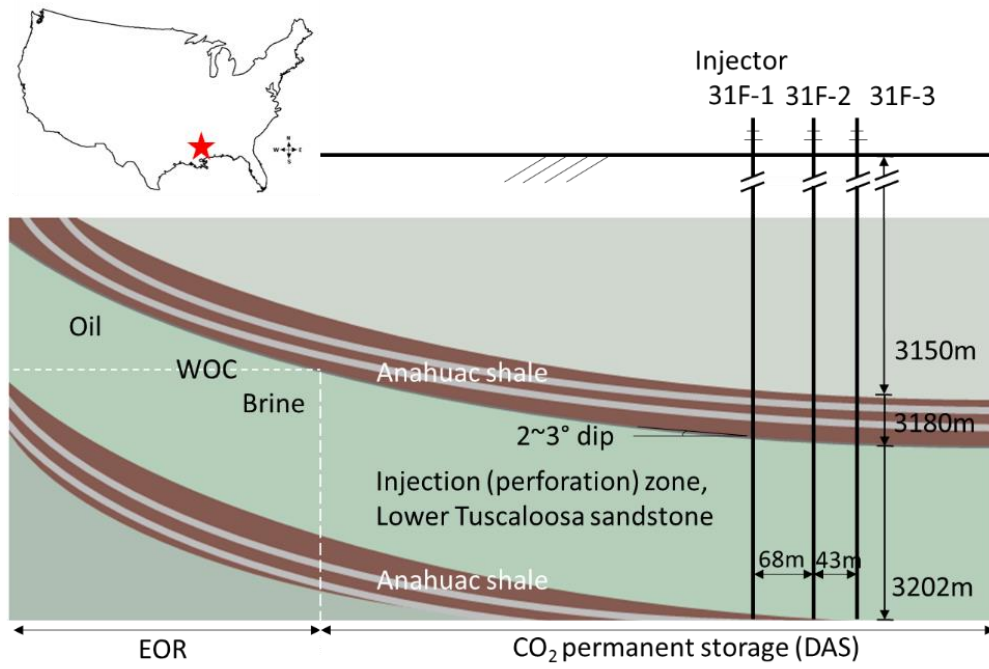
Figure 3.1: Schematic diagram of Cranfield water leg Detailed Area of Study (DAS) for permanent storage of CO_2.
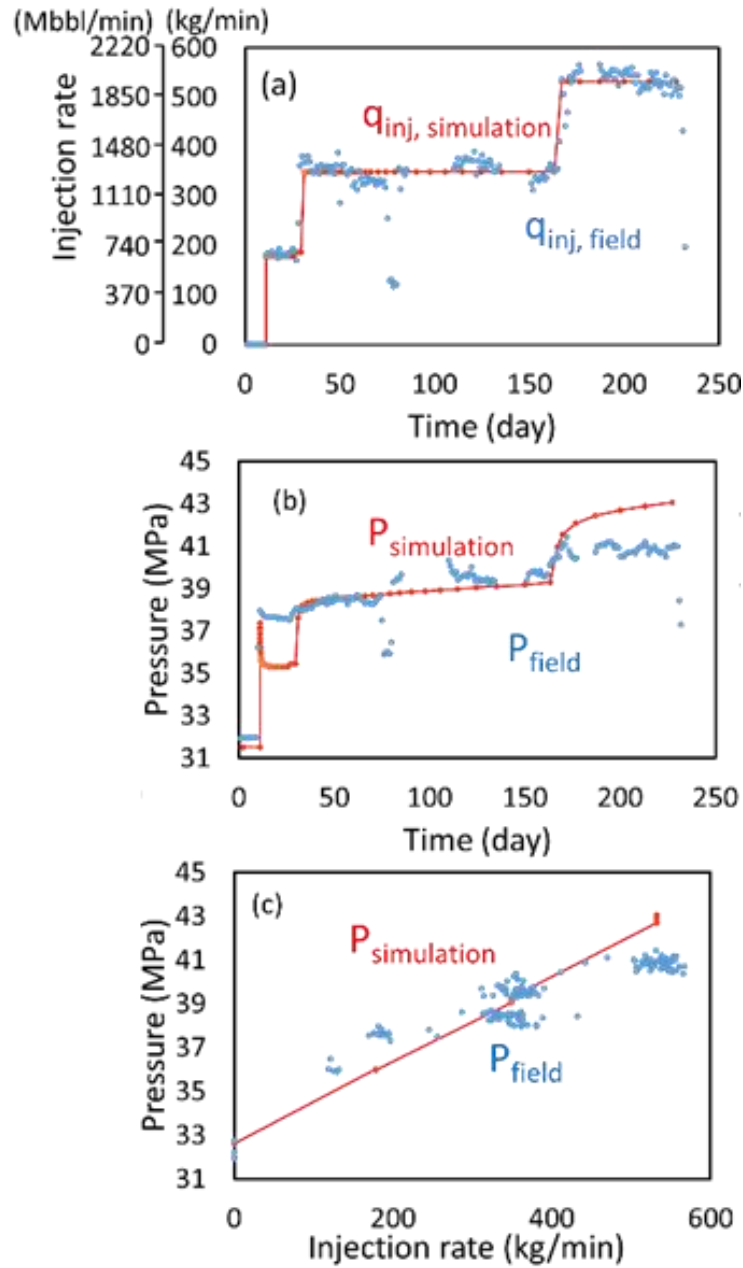
Figure 3.2: Imposed injection rate (a), bottom-hole pressure (BHP) (b), and BHP vs injection rate (c) at well CFU31F-1 and the expected simulation result with constant permeability. Figure 3.2(c) shows the deviation of field data from simulation linear line due to possible fracture opening.

In this study, we built a reservoir model to simulate CO_2 injection in the DAS using CMG-GEM (Computer Modeling Group Ltd., 2013) coupled with thermo-poro-elasticity and compositional fluid behavior. The model uses petrophysical and geomechanical properties from well-logging analysis calibrated with laboratory measurements in field cores. Then we show the results of history matching of the pressure response at the injector (CFU31F-1) using this reservoir model with and without thermo-elasticity. We expand the model on the analysis of the effects of thermally induced stress relaxation on effective stress and the possibility of propagation of open-mode fractures at the injector. Finally, the model is used for sensitivity analysis to injection temperature, thermal expansion coefficient, and maximum fracture permeability. The sensitivity analysis helps understand the effects of various thermos-elastic parameters on the geomechanical stability of the CO_2 reservoir.

3.2 CRANFIELD DAS RESERVOIR PROPERTIES AND MODEL

The DAS model includes vertical heterogeneity in petrophysical and geomechanical properties from well-logging analysis and laboratory core measurements on Tuscaloosa sandstone. We detail the construction of the reservoir model in the following subsections.

3.2.1 Petrophysical Properties of Lower Tuscaloosa Sandstone

We estimated reservoir properties from well-logging data analysis from the injection (CFU31F-1) and one of the observation wells (CFU31F-2). The distance between these two wells is 68 m (223 ft). The two wells show similar rock types and sequences with

slightly shifted depth as a result of reservoir dip of $2 - 3°$ (Lu et al., 2013). Since the purpose of this paper is to perform a geomechanical analysis of the near-injector region, the simulation includes heterogeneity in the vertical direction only for both petrophysical and geomechanical properties.

Figure 3.3 summarizes the well log analysis results and averaged properties for the simulation model. We applied averaged property values every 1.1 m (3.6 ft) to our DAS model balancing the computational cost to run simulations and the level of detail of the reservoir sequence and heterogeneity (Figure 3.1).
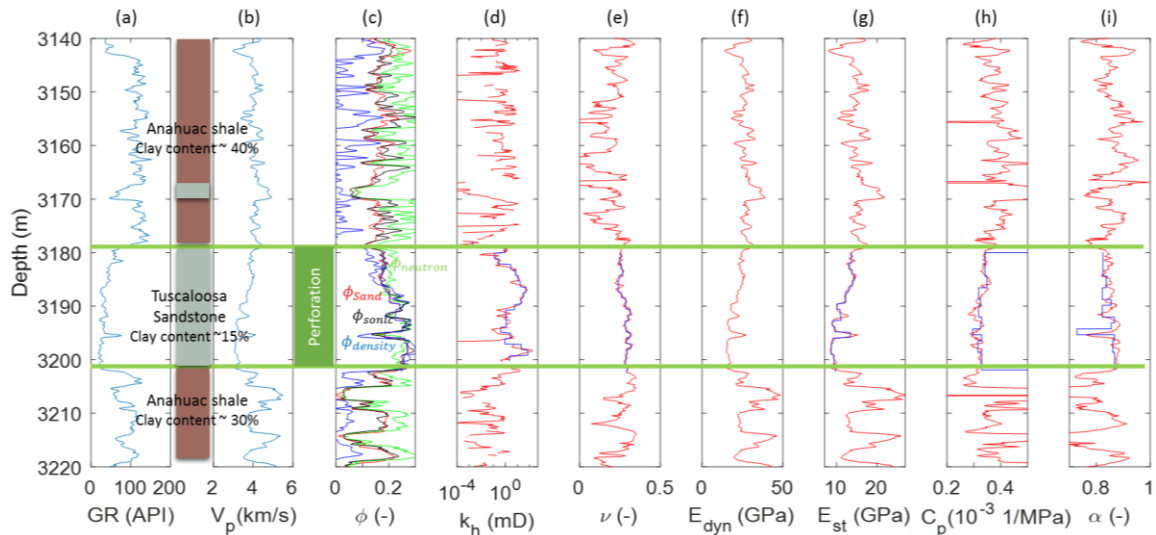
Figure 3.3: Geological context of Cranfield DAS: (a) gamma ray, (b) compressional wave velocity, (c) porosity, (d) horizontal permeability, (e) Poisson's ratio, (f) dynamic Young's modulus, (g) static Young's modulus, (h) pore compressibility. Red lines are well-logging analysis results, and dark blue lines are the averaged values for simulation at injection zone.

3.2.1.1 Porosity and permeability

We used clay corrected sand porosity (Figure 3.3-c - Torres-Verdin, 2016). As discussed above, the injection and observation wells show similar rock types and

42

sequences. Hence, we adopted permeability values estimated for the observation well CFU31F-2 after correcting for the depth difference. The ratio between horizontal to vertical permeability is set to be 0.1 from laboratory permeability measurements (Table 3.1).

Table 3.1: Information of samples from laboratory experiments.

Sample number	Depth [m]	Diameter [in]	Length [in]	Weight [g]	Bulk density [g/cm³]	Porosity	Rock density [g/cm³]	Permeability [mD]
38V	3189.9	0.97	2.00	44.30	1.82	0.31	2.13	10 - 20
30V	3192.9	0.98	1.74	42.30	1.96	0.26	2.22	20 - 40
26H	3188.6	0.97	1.66	36.97	1.83	0.31	2.14	150 - 250

3.2.1.2 Capillary pressure and relative permeability

We assigned heterogeneity to relative permeability and capillary pressure distinguishing the caprock and the injection zone (sandstone) by adopting the corresponding parameters from the Brooks-Corey model (Hosseini et al., 2013).

3.2.2 Geomechanical Properties

3.2.2.1 Dynamic and static elastic moduli

We calculated elastic moduli using sonic elastic travel time. Since the shear wave travel time was not measured at the injector, we applied the ratio between compressional wave velocity V_P and shear wave velocity V_S from the observation well (CFU31F-2) to calculate V_S at the injector. The ratio V_P/V_S varies from 1.5 to 1.7 at the injection zone, slightly lower than the assumed value 2.0 in Carter and Spikes (2014) and Daley et al. (2014). The calculated static moduli were calibrated with the laboratory measured ratio between static and dynamic moduli approximately equal to 0.56 (Jung and Espinoza,

2017).

We assigned the calculated static elastic moduli to nine different rock types based on porosity (including seven for the injection zone and two for the caprock and underlying layers) in order to build an accurate mechanical reservoir model (Table 3.2).

Table 3.2: Rock types applied to Frio reservoir modeling for capillary pressure and relative permeability (Assumed parameter includes $S_m = 1$).

Rock type	E (GPa)	v	C_p (1/psi×10^{-6})	α	ϕ_{avg}
1	13.71	0.255	2.35	0.824	0.177
2	13.45	0.240	2.40	0.837	0.181
3	12.15	0.285	2.19	0.822	0.200
4	9.84	0.286	2.24	0.855	0.241
5	9.02	0.286	2.27	0.868	0.260
6	15.23	0.324	2.04	0.728	0.153
7	8.68	0.304	2.17	0.861	0.269
8 (Caprock)	16.80	0.150	7.78	0.849	0.050
9 (Overlying layer)	25.20	0.150	25.9	0.774	0.010

3.2.2.2 Unloading formation compressibility

The model adopts heterogeneous pore compressibility values according to the corresponding rock types. The value of pore compressibility results in significant impact to local pore pressure calculation upon injection (Jung et al, 2017). We calculated the pore compressibility C_{pore} based on the relationship between the unloading constrained elastic modulus $M = \frac{(1-v)E}{(1+v)(1-2v)}$ and porosity ϕ:

$$C_{pore} \approx \frac{\phi}{M} \qquad \text{(Eq. 3.1)}$$

The calculated unloading formation compressibility is assigned to the nine rock types (Table 3.2 and Figure 3.3-h).

3.2.2.3 Biot coefficient

The DAS model uses a heterogeneous Biot coefficient (α) as shown in Figure 3.3-i. Biot coefficient is calculated with the following equation:

$$\alpha = 1 - \frac{K}{K_S} \qquad\qquad\text{(Eq. 3.2)},$$

where K is bulk drained modulus and K_S is the unjacketed bulk modulus. The parameter K_S is estimated to be 53 GPa using experimentally measured poroelastic response of Tuscaloosa sandstone samples from the observation well CFU31F-3 (Jung and Espinoza, 2017). Considering Biot coefficient not equal to unity yields appropriate initial fracture gradient and effective stress alteration upon pore pressure change (Kim and Hosseini, 2017).

3.2.3 Cranfield Simulation Domain and Boundary Conditions

3.2.3.1 Simulation domain

The DAS simulation includes 87,261 (59×51×29) degrees of freedom with refined mesh near the injector region (Figure 3.4). The grid block size decreases to 6.1 m in horizontal direction and 1.1 m in vertical direction at the injection zone. A tensor product refinement was used to better capture changes in the DAS, where the injection well is located. This approach is especially useful when a limited number of reservoir properties is available from well logs, seismic observations and geological models. The compositional flow model in CMG-GEM uses the Peng-Robinson cubic equation of state (PR-EOS) for describing fluid phase behavior (Table 3.3). Henry's law calculates the CO_2 solubility as 1.2 (mol of CO_2)/(kg of water) using the coefficients in Table 3.3 at P = 31.0 MPa and T =

127°C.
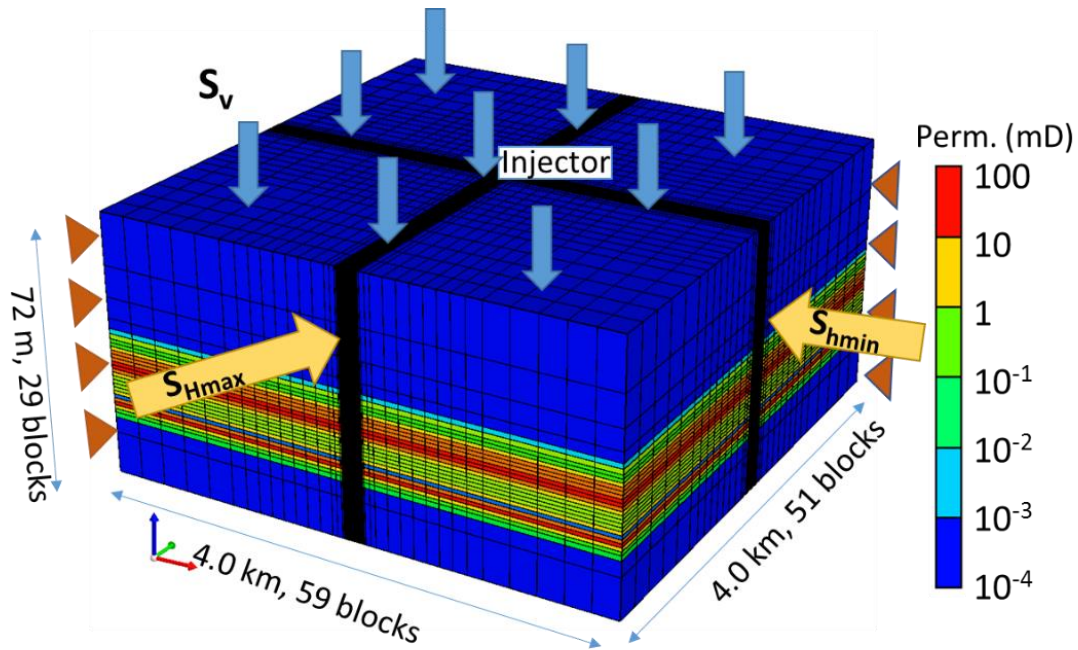
Figure 3.4: Reservoir domain and simulation boundary conditions.

Table 3.3: EOS parameters for CO_2 solubility calculation.

	T_c [R°]	P_c [psi]	Z_c	ω[-]	M_w [g/mol]	P [-]	Henry's law constant [kPa]	P_{ref} for Henry's law [MPa]	Partial molar volume [l/mol]
CO_2	547.56	1070.4	0.302	0.224	44.01	78.0	749,588	31.0	0.037

3.2.3.2 Flow boundary conditions and the domain model size

We assumed no flow boundary condition with a reservoir size large enough so that it resembles an infinite-acting flow regime in the beginning and then pseudo-steady state flow regime during the CO_2 injection cycles. The reservoir domain size is 4.0×4.0 km^2 based on sensitivity analysis. The simulation domain thickness is 76.8 m including both injection zone and parts of caprock and underlying layers.

46

3.2.3.3 Geomechanical boundary conditions

We assumed zero-lateral strain at boundaries and constant vertical stress conditions above the caprock. We applied total vertical stress $S_v = 66.2$ MPa at 3,150 m of depth (top of the caprock layer in the simulation domain - stress gradient of 21 MPa/km (0.933 psi/ft) (Figure 3.5). The initial stress condition of the numerical model is shown in Figure 3.5. Using the vertical stress applied for simulation, we also calculated horizontal stress assuming a stacked poroelastic medium without tectonic strains:

$$S_h = \left(\frac{v}{1-v}\right)S_v + \left(\frac{1-2v}{1-v}\right)\alpha P_p \qquad \text{(Eq. 3.3),}$$

where S_v and S_h are vertical and minimum horizontal total stresses, P_p is pore pressure, v is Poisson's ratio, and α is the Biot coefficient (Lorenz et al., 1991). The initial stress condition of the numerical model is close to the analytical solution and captures the local minimum horizontal stress at ~ 3,186 m (Figure 3.5). We assumed the initial maximum total horizontal stress is 6.9 MPa (1,000 psi) higher than the minimum horizontal stress.

47
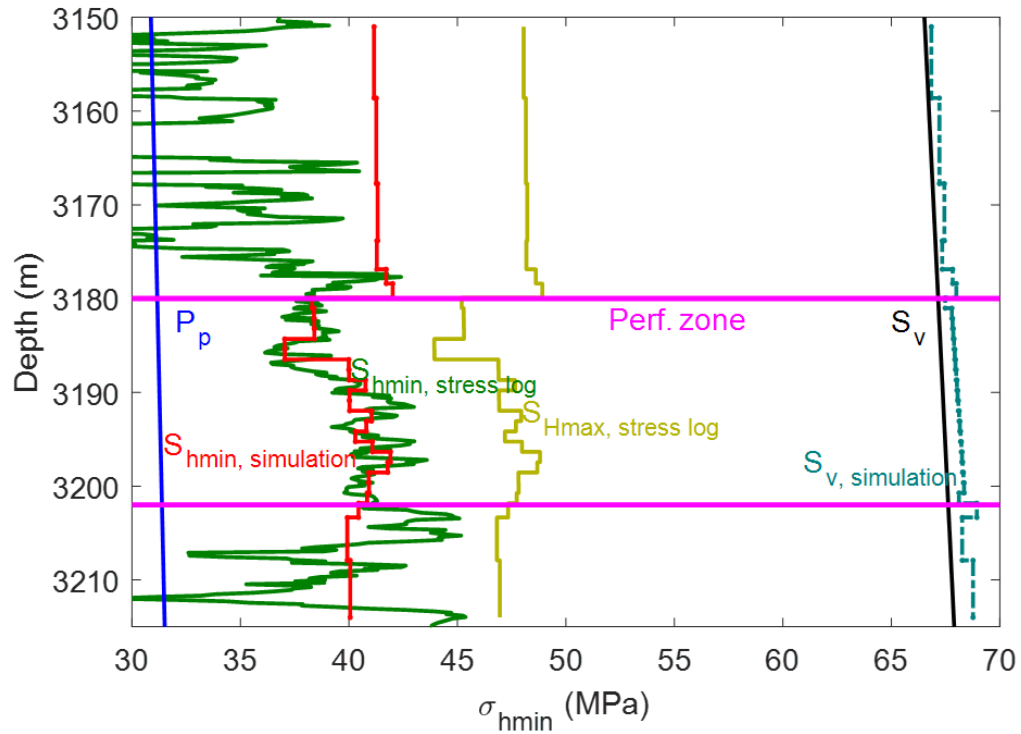
Figure 3.5: Initial stress conditions in the injection zone from analytical solutions and numerical simulation.

3.2.3.4 Fracture permeability model

We adopted dual permeability and the Barton-Bandis model (Barton et al., 1985) to capture fracture opening and the permeability evolution. The Barton-Bandis model enables permeability changes depending on effective stress. We assigned dual permeability elements aligned with the direction of maximum horizontal total stress S_{Hmax}. The fracture permeability is the same as the matrix permeability initially. Once the Biot effective stress reaches zero, the fracture is activated, and its permeability increases with a prescribed law.

Since the Barton-Bandis model follows a joint-system concept, we adjusted the maximum activated fracture permeability as 100 D equivalent to approximately 1.5 mm aperture of each fracture. The fracture is spaced every 3.0 m parallel to minimum principal stress direction. The details of parameters used for Barton-Bandis model are available in Table 3.4. The fracture model in CMG-GEM applies the Biot effective stress for Barton-Bandis fracture permeability calculation. This feature delays a fracture opening around 0.1 days in the model compared to applying Terzaghi's effective stress.

Table 3.4: Barton-Bandis parameter for fracture permeability evolution.

Initial fracture aperture [mm]	0.006
Initial normal fracture stiffness [kPa/m]	1.5×10^9
Fracture opening stress [kPa]	0
Hydraulic fracture permeability [mD]	100,000
Fracture closure permeability [mD]	233
Residual value of fracture closure permeability [mD]	1

3.2.3.5 Thermo-elastic properties and initial conditions

The initial bottom-hole temperature at CFU31F-1 is 127°C. The temperature dropped to 72 °C during injection according to field measurements (Kim and Hosseini, 2013). We set the initial temperature of the reservoir and injected CO_2 accordingly. The simulation adopts a linear thermal expansion coefficient $\alpha_T = 1.3 \times 10^{-5}$ 1/°C in the range of sandstones ($1.3 \sim 2.0 \times 10^{-5}$ 1/°C - Fjaer et al. 2008).

3.2.4 Description of Performed Simulations

Reservoir simulation included various cases (Table 3.5):

- Baseline scenario simulation without thermo-elasticity (BC wo TH),

- Thermo-elastic history match simulation with thermo-elsaticity (BC TH),

- Sensitivity analysis cases varying injection temperature (IT), thermal expansion coefficient (THexp), and fracture permeability (FP).

First, we conducted a simulation without thermo-elasticity. Injection schedule is adjusted to mimic the field injection schedule (Figure 3.6). We performed history matching of the DAS pressure transient by changing fracture permeability and thermal expansion coefficient and including thermo-elasticity as described in Section 3.2.3. The objective of CO_2 injection simulations was to quantify the stress alteration from CO_2 injection and the effect of thermo-elasticity. Further, the simulation examines the possibility of open-mode failure at the injection zone during CO_2 injection. Based on the history matched case, we conducted sensitivity analysis on injection temperature, thermal expansion coefficient, and fracture permeability. Both the injection temperature and the thermal expansion coefficient determine the amount of stress reduction as the rock temperature decresases from the near-injector region. Fracture permeability affects the BHP when the fracture opens. The details of simulations inputs are available in Table 3.5.

Table 3.5: Simulation input values (injection temperature, thermal expansion coefficient and fracture permeability) varied in numerical simulations.

	BC wo TH	BC TH	IT1	IT2	IT3	IT4	FP1	FP2	THexp1	THexp2
Thermo-elasticity	Isothermal	Non-Isothermal				Non-isothermal				
$T_{injection}$ [°C]	72	72	48	60	85	97	72	72	72	72
$k_{fracture}$ [D]	100	100	100	100	100	100	10	1,000	100	100
α_T [1/°C×10^6]	13	13	13	13	13	13	13	13	9.9	16

3.3 Results and Discussion

3.3.1. History-match Simulation without Thermo-elasticity

The simulation input properties and boundary conditions are described in detail in section 2.3. The results show that BHP is directly proportional to injection rate and pressure never reaches the minimum horizontal stress even at the depth of 3,186 m, local least of minimum horizontal stress S_{hmin} (Figure 3.5 & 3.6). The effective stress is positive throughout the three injection cycles, so that, fractures never initiate in the Barton-Bandis fracture model (Figure 3.7). Hence, the simulation without thermo-elasticity fails to predict the relatively flat pressure response with increasing injection rate observed in the field.
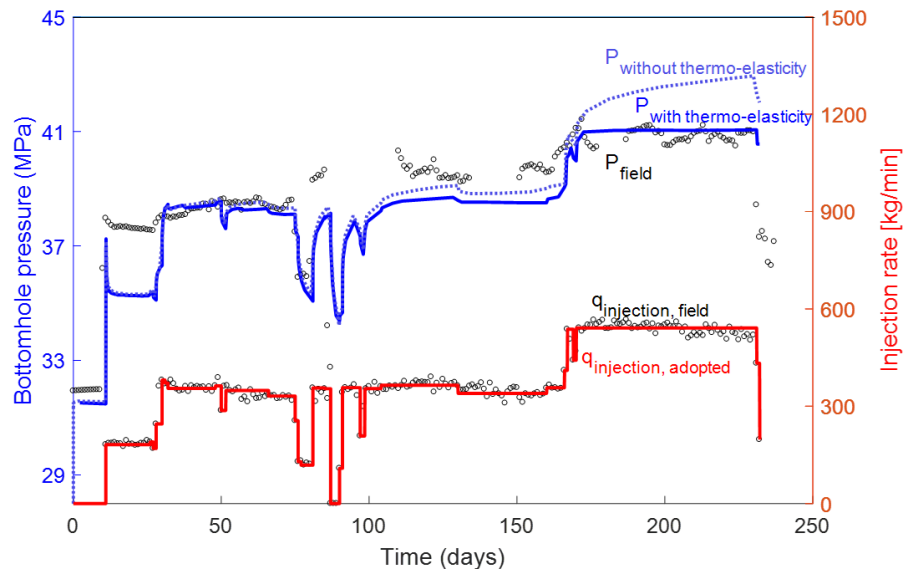
Figure 3.6: Injection schedule and BHP of CFU31F-1: field data, simulation without thermo-poro-elasticity, and simulation with thermo-poro-elasticity.

3.3.2 History-match Simulation with Thermo-elasticity

The simulation with thermo-elasticity shows a drastic reduction in minimum horizontal stress (Figure 3.7), and the Biot effective stress reaches zero at the depths of 3,186 m (local minimum of S_{hmin}) after 31 days of CO_2 injection when the first jump in injection rate happens. "Negative" effective stress activates block fracture permeability and increases its value. The fracture half-length was 3.0 m at 31 days and increased up to 51.8 m at the end of the simulation (232 days). Comparing the simulation without thermo-elasticity to the one with thermo-elasticity, we observe little difference in pressure response before 166 days. This is because the fractured blocks in the thermo-elastic simulation extend less than 33.5 m from the wellbore before the second injection rate increase.
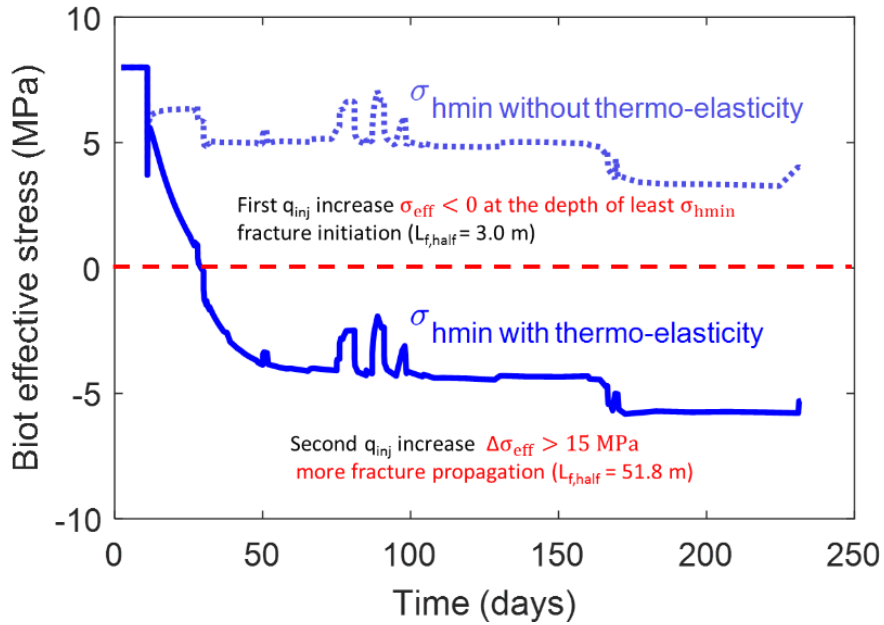
Figure 3.7: Biot effective stress at the wellbore block at depth 3185 m (local the least horizontal minimum stress) with and without thermo-elasticity.

Injection of CO_2 pumped from bottom-hole temperature conditions (T = 72 °C and $T_{reservoir}$ = 127 °C) results in a change of total minimum horizontal stress of ~ 9.7 MPa (1,406 psi) and Biot effective horizontal stress of ~ 9.0 MPa (1,305 psi) in the simulation (Figure 3.7). The analytical solution for one-dimensional vertical strain and no change of pore pressure yields a horizontal stress reduction equal to

$$\Delta S_{hmin} = \frac{\alpha_T \Delta T E}{1-v} = \frac{13\cdot 10^{-6} [\frac{1}{°C}]\cdot 55[°C]\cdot 12.14[GPa]}{1-0.285} = 12.1 \text{ MPa}. \qquad \text{(Eq. 3.4)}$$

The numerical solution agrees reasonably well with the one-dimensional strain assumption in the analytical solution. Even though the CO_2 plume extends up to 400 m, the reduction in temperature is significant only around 65 m away from the wellbore (Figure 3.8). Therefore, horizontal stress alteration due to thermal stress relaxation is more pronounced in the near-wellbore region.
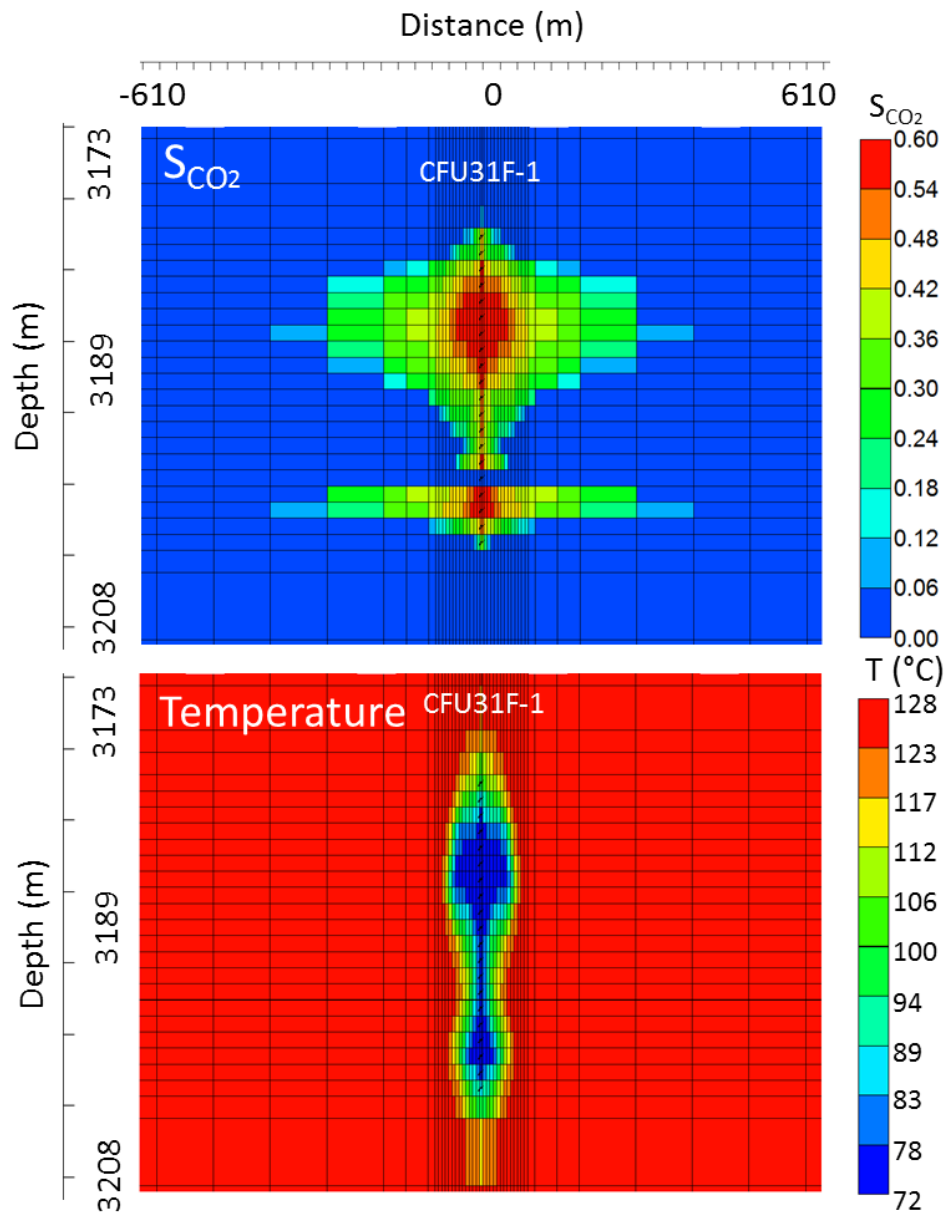
Figure 3.8: CO$_2$ Saturation and temperature in the DAS at the end of simulation (220 days after the initiation of the injection). Cross section perpendicular to S$_{hmin}$. The wellbore CFU31F-1 is in the center.

3.3.3 Sensitivity Study to Injection Temperature

Injectant temperature has a direct impact on the change of total horizontal stress. Low injection temperature reduces the horizontal total stress at the near-wellbore region significantly (Figure 3.9). However, the injection temperature does not change the BHP directly, rather it changes the fracture propagation length and the resulting BHP (fixed injection rate). Before the large fracture opening and propagation at the second injection rate increase at 172 days, the BHP did not show a significant difference among simulations IT1 to IT4. After the development of a large open-mode fracture in simulation at 172 days, the BHP begins to show notable gaps between the two simulations IT1 and IT4. The simulation case with the highest injection temperature T = 98 °C (ΔT = 29 °C) shows the shortest fracture propagation length equal to 39.6 m at the end of the simulation. The simulation with the lowest injection temperature T = 55 °C (ΔT = 72 °C) shows fracture propagation up to 70.1 m. Further, the difference of Biot effective stress between two cases is higher than 9 MPa. These simulations clearly demonstrate that the temperature of the injected fluid alters the horizontal total stress and impacts to fracture opening and propagation, and the resulting BHP. Therefore, the temperature of the injected fluid should be carefully analyzed for CO_2 storage injection to avert development of open-mode fractures.
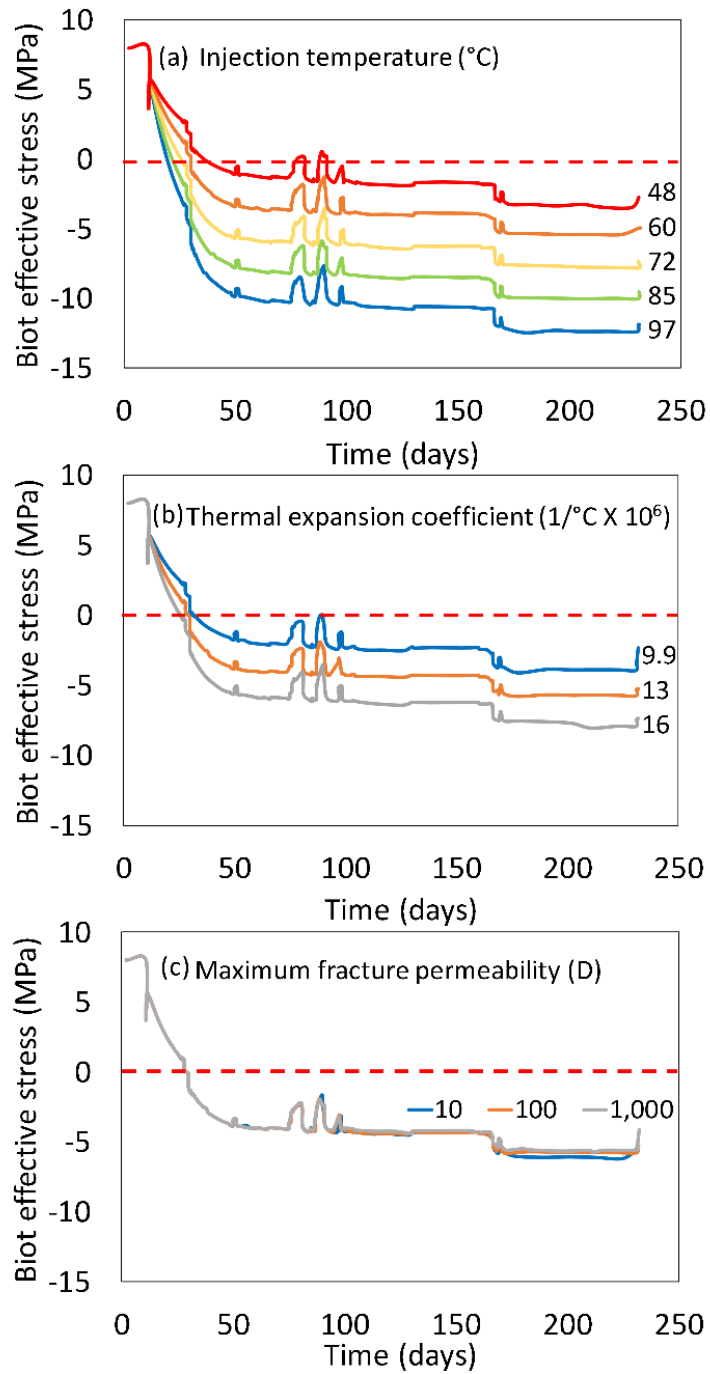
Figure 3.9: Sensitivity analysis results of (a) CO_2 injection temperature, (b) Thermal expansion coefficient, and (c) Maximum opened fracture permeability.

3.3.4 Sensitivity Study to Thermal Expansion Coefficient

The thermal expansion coefficient α_T determines horizontal stress reduction from temperature change. The simulation using the highest thermal expansion coefficient $\alpha_T = 1.60 \times 10^{-5}$ 1/°C (THexp2) results in earlier fracture opening and longer fracture propagation (58.0 m half length) than the case with lowest thermal expansion coefficient $\alpha_T = 0.99 \times 10^{-5}$ 1/°C (THexp1) with 39.6 m of fracture half-length. Simulation THexp2 shows 9 MPa decrease in Biot effective stress compared to 4 MPa decrease of the stress in Simulation THexp1 (Figure 3.9-b). The range of thermal expansion coefficient in sandstones is 1.3 to 2.0 $\times 10^{-5}$ 1/°C (Fjaer et al. 2008). Hence, accurate determination of the thermal expansion coefficient greatly contributes to predicting the fracture initiation time, length, and the resulting BHP response.

3.3.5 BHP Sensitivity to Fracture Permeability

Fracture opening accelerates the fluid pressure diffusion by increasing the effective permeability of the reservoir. Therefore, the amount of pressure decrease depends on the transmissibility of fractures. Our sensitivity analysis predicts the lowest BHP (P = 40.8 MPa at 225 days) for fracture permeability $k_f = 1,000$ D (Simulation FP2). The BHP is 1.43 MPa higher for Simulation FP1 with $k_f = 10$ D. Fracture half-length at the end of the simulation is 45 m and 64 m for FP2 and FP1 respectively. There are no significant differences in Biot effective stress between these two simulations (Figure 3.9-c).

3.3.6 Horizontal Stress Reduction due to Chemically-induced Creep from CO_2-acidified brine

Brine acidification by injected CO_2 can trigger rock deformation, alter rock strength and change reservoir local stresses (Hangx et al., 2012; Jung and Espinoza, 2017; Espinoza et al., 2018). This section investigates chemo-mechanical effects of CO_2-acidified brine injection in Tuscaloosa sandstone in order to assess their implications on wellbore pressure response.

We conducted laboratory experiments to observe the effect of CO_2-acidified brine injection and potential effects on rock fabric on stress alteration. We injected CO_2-acidifed brine in two Tuscaloosa sandstone samples (26H and 30V) subjected to in-situ effective stress conditions within a triaxial loading frame. Figure 3.10-a shows pressure and stress measurements for horizontal sample 26H. Before the CO_2-acidified brine injection, the sample was saturated with brine at a pore pressure of 2.1 MPa and constant total stresses $S_{axial} = 22.8$ MPa and $S_{radial} = 11.7$ MPa for an hour until creep was negligible. Then we injected the CO_2-acidified brine into the sample. The vertical dashed line in Figure 3.10-b indicates the initiation of the injection. The pressure difference between upstream P_{up} and downstream P_{down} was adjusted to be lower than 0.7 MPa. The confining and deviatoric stress are held constant during brine injection. Figure 3.10-b shows volumetric strain changes with four cycles of CO_2-acidified brine injection. The first injection cycle exhibits the highest strain damage rate. The change of strain diminishes with subsequent injection cycles. The maximum change of volumetric strain is $2.9 \cdot 10^{-3}$ during four cycles of the injection (Figure 3.10-b). Another tested sample (30V) showed $2.0 \cdot 10^{-3}$ volumetric strain

change during 140 minutes of the acidified brine injection. Since the vertical permeability is about 10 times lower than the horizontal sample, the injection amount was smaller in Sample 30V than in sample 26H.
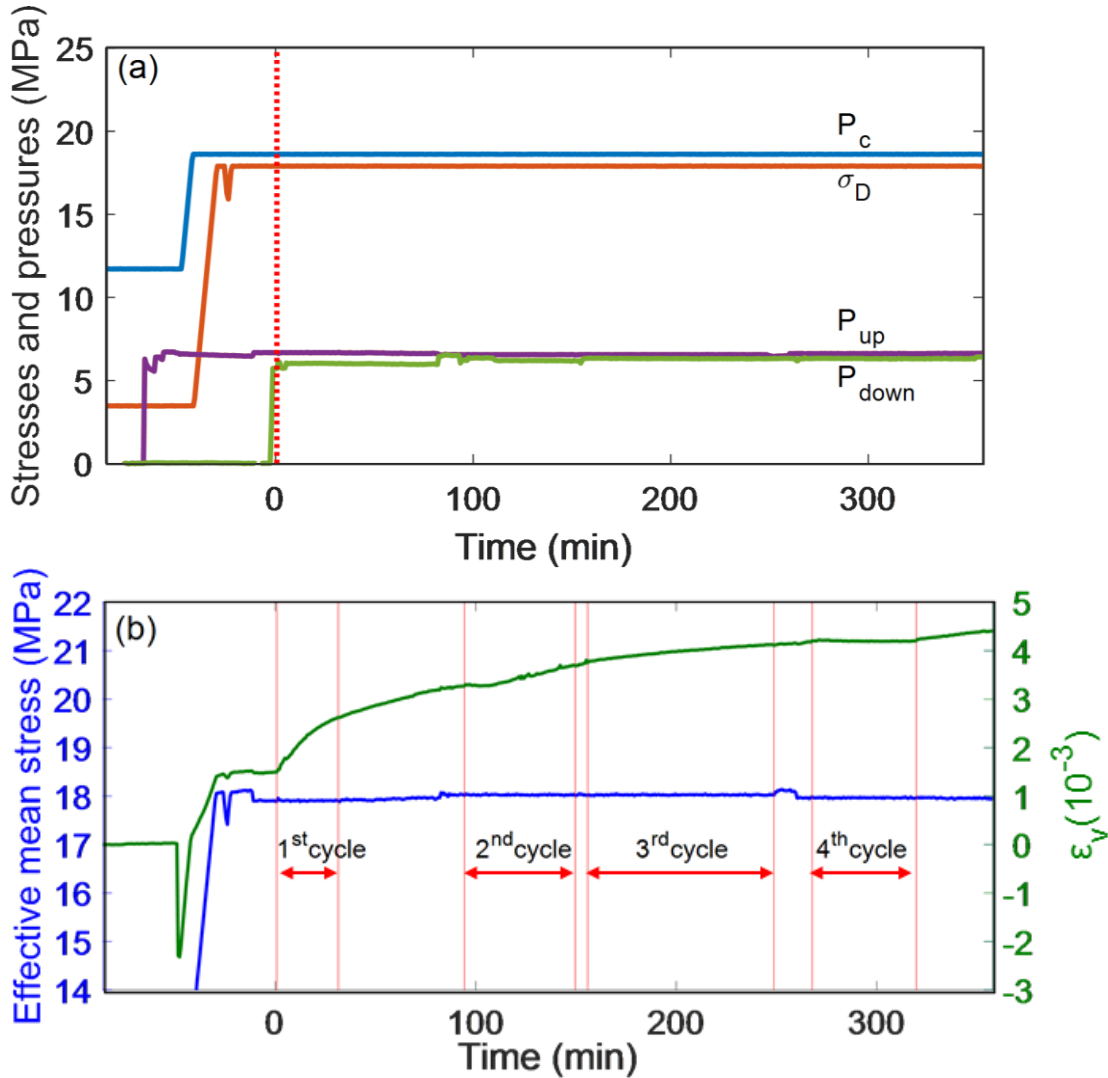
Figure 3.10: (a) Stress and pressure signals during injection of CO_2-acidified brine in a core sample of Tuscaloosa sandstone. (b) Volumetric strain changes upon injection of CO_2-acidified brine. The mean effective stress is constant $\sigma_{mean} = 18.0 \pm 0.13$ MPa during injection.

The results suggest that injection of CO_2-acidified brine increases the creep rate quickly after contacting with the rock. Other experiments have suggested rapid responses of chlorite clays to CO_2-acidified brine in Tuscaloosa sandstone and Mt. Simon sandstone (Yoksoulian et al., 2013; Rinehart et al., 2016). Chlorite dissolution is negligible in CO_2-acidified brine (Lu et al., 2012; Islam et al., 2016). However, autoclave experiments showed disintegrated Tuscaloosa sandstone samples after testing and slow depressurization (Lu et al., 2012). Hence, it seems likely that clay swelling, debonding, and dislodging -by changes in pore fluid chemistry- may have contributed to the damage of chlorite cements that increased creep rates in our experiments.

Chemical effects at the time scale of fracture propagation and injection are likely much less than those of thermal effects. Hence, we did not account for chemo-mechanical effects in numerical simulations. At large time-scales, interaction of CO2-acidified brine and rock minerals could lead to vertical deformation and horizontal stress relaxation from enhanced creep (Espinoza et al., 2018). For example, a change of strain of $\sim 1 \cdot 10\text{-}3$ (change of radial strain in horizontal sample 26H) multiplied by the height of the injection interval results in an upper bound estimation of a vertical displacement caused by enhanced creep: $1 \cdot 10\text{-}3 \times 20 \text{ m} = 2 \text{ cm}$. A change of 2 cm at 3 km of depth is negligible regarding subsidence. On the other hand, a change of lateral stress under zero lateral strain caused by chemical-stress-relaxation is the product of chemically-induced strain ($\sim 0.3 \cdot 10^{-3}$ from the change of axial strain in horizontal sample 26H) and the plane strain modulus. Hence, the

horizontal stress reduction could be as much as $\Delta\sigma_{hmin} = \varepsilon \cdot \frac{E}{(1-v^2)} = 0.3 \cdot 10^{-3} \times 10$ GPa

/ $(1-0.3^2) = 3.3$ MPa (Shovkun and Espinoza, 2018).

3.4 CONCLUSIONS

We performed a thermo-poro-elastic simulation of CO_2 injection in the water leg of the Cranfield reservoir and additional laboratory experiments in order to observe the geomechanical effects on wellbore response. Simulation results and sensitivity analyses show that:

- Heterogeneity in geomechanical properties such as Young's modulus, Poisson's ratio, and pore compressibility is critical to predicting local pore pressure buildup, horizontal stress and the localization of potential open-mode fractures in the wellbore.

- Injection of CO_2 from surface ambient conditions lowers temperature of the reservoir rock and leads to horizontal stress reduction in a near-wellbore region. The simulation results support the hypothesis of development of an open-mode fracture at the injector in the Cranfield CO_2 injection site.

- Despite the occurrence of an open mode fracture, the model also predicts fracture containment without propagation into bounding sealing layers.

- Sensitivity analysis of injection temperature and thermal expansion coefficient shows significant impact of these parameters on horizontal stress and fracture propagation. The fracture permeability changes the BHP upon injection. Therefore, accurate

calculation using injection temperature and thermal expansion coefficient is critical to avoid fracture opening and large fracture propagation.

- Laboratory experiments demonstrate that CO_2-acidified brine induces enhanced creep in chlorite-rich Tuscaloosa Sandstone. However, the impact of chemical effects at the time scale of injection is limited compared to thermal effects on stress reduction.

Chapter 4

CO_2 charged brines changed rock strength and stiffness at Crystal Geyser, Utah: Implications for leaking subsurface CO_2 storage reservoirs[1]

4.1 INTRODUCTION

Large-scale injection of carbon dioxide (CO_2) in deep subsurface formations is an alternative for disposing anthropogenic CO_2 instead of venting to the atmosphere (Pacala and Socolow, 2004). Natural CO_2 accumulations (stable and seeping) exist in various sedimentary basins, where pore pressure has been documented to vary from below hydrostatic pressure to almost lithostatic stress (Chiodini et al., 1995; Pearce et al., 1996; Heath et al., 2009; Sathaye et al., 2014; Hangx et al., 2015). Although the oil and gas industry has developed mature technologies for CO_2 injection and enhanced oil recovery, storing large volumes of CO_2 requires careful analyses of all possible implications that may affect effective and long-term CO_2 sequestration (Sharp, 1975; Lake, 1996; Rutqvist et al., 2016).

Carbonic acid is the most common chemical weathering agent on the Earth's crust, resulting from the reaction between atmospheric CO_2 and rainwater (Stumm and Morgan, 2012). Likewise, the injection of CO_2 in deep geological formations induces geochemical disequilibrium from mixing of CO_2 and resident brine, leading to reactions with minerals

in the host rock including potential mineral dissolution/precipitation and clay fabric alteration (Gunter et al., 2000; Kaszuba et al., 2005; McGrail et al. 2009; Espinoza and Santamarina, 2012; Yoksoulian et al., 2013). The extent of acidification increases with CO_2 pressure and CO_2 solubility in brine, and reaches a plateau around the CO_2 critical pressure (Duan and Sun, 2003; Spycher et al., 2003). Chemical reactions may occur in the reservoir/storage rock, the caprock, well-cement interfaces, and in fault gouge material, if contacted by CO_2. Advective processes control reactions in the reservoir rock (including density-driven convection caused by CO_2 dissolution into brine), while diffusion mechanisms control reactions in the caprock (in the absence of connected fractures) (Gaus et al., 2005; Xu et al., 2005; Kneafsey and Pruess, 2010; Hangx et al., 2010; Rutqvist et al., 2016).

Dissolution and precipitation of minerals due to CO_2 injection can alter rock petrophysical and geomechanical properties (Vanorio et al., 2011; Major et al., 2014; Rohmer et al., 2016). Such alterations depend on the amount of reacted minerals and where dissolution and precipitation take place in the pore structure. For example, precipitation of small mineral amounts in pore throats instead of pore bodies can have a significant effect on permeability and capillary pressure (Ross et al., 1982; Chiodini et al., 1995; Benavente et al., 2004). Predominantly quartzitic sandstones and unconsolidated sands are expected to have minor chemo-mechanical alteration when exposed to CO_2 due to a lack of reactive minerals. Sandstones with "CO_2-weak" intergranular cements appear to be the most easily alterable type of rock with respect to geomechanical properties, as even minor alterations

can have a large impact on geomechanical properties dependent on cementation. Dissolution and degradation of load-bearing cements can lead to (1) decreases of cohesive strength, fracture toughness, and yield stress locus size, (2) increases of compliance and creep, (3) changes in post-peak behavior, and (4) changes in frictional behavior (Fernandez and Santamarina, 2001; Bemer and Lombard, 2010; Xie et al., 2011; Zinsmeister et al., 2013; Major et al., 2014; Bakker et al., 2016; Rinehart et al., 2016; Sun et al., 2016a). Examples of these types of rock include carbonate-cemented sandstones (e.g., Entrada sandstone, Castlegate sandstone), and clay-cemented sandstones (Chlorite-cemented Tuscaloosa sandstone and Mt. Simon sandstone) (Yoksoulian et al., 2013; Rinehart et al., 2016; Major et al., in review). Grain-supported carbonate rocks such as chalks can suffer significant strains when exposed to CO_2-acidified brine (Liteanu et al., 2013), while matrix-supported carbonate rocks can undergo significant pore enlargement with modest effects on rock mechanical properties until large amounts of rock are dissolved (Fredd and Fogler, 1998; Carroll et al., 2013). Rocks with patchy or laminated distribution of dissolvable minerals, such as carbonate-rich shales, stand in between dissolvable-matrix rocks and dissolvable-cement sandstones (Shovkun and Espinoza, 2017). Core-scale experimental results investigating CO_2 reactions in shale caprocks are limited due to the inherent difficulties in machining and flowing fluids through such tight and fragile lithologies (Ilgen et al., in review). Design of CO_2 injection projects often neglects chemically-induced strains and stresses, however, coupled chemo-mechanical processes can affect short-term injection response and long-term trapping mechanisms in CO_2 geological storage.

Examples of coupled processes induced by mineral dissolution include changes in wellbore injectivity, reservoir compaction, and lateral stress relaxation (Ross et al. 1982; Oudinot et al., 2011; Shin et al., 2008; Stefanou and Sulem, 2014; Shovkun and Espinoza, 2017).

In this study, we investigate the changes in geomechanical properties caused by CO_2-charged brine over geologic time from rocks in a sedimentary system accessible in outcrops at the Crystal Geyser field site. First, we present an overview of the Crystal Geyser site, rock diagenetic history, and diagenesis triggered by seepage of CO_2-rich brine from a natural CO_2 source along faults. Second, we show and discuss experimental results from triaxial testing of rock specimens unaltered and altered by CO_2-charged brine, i.e., rock stress-strain behavior and shear strength. A systematic investigation of mode-1 fracture propagation in the same rock samples is outside the scope of this study and will be reported in a separate paper. The triaxial testing results are complemented by microphotographs, SEM-EDS, and X-ray microtomographic observations to understand how alteration and heterogeneities affect strain localization and micromechanical failure processes. Third, we introduce the application of discrete element modeling to understand particle-level mechanisms responsible for the mechanical alteration of the tested sandstone samples. The article finishes with a comparison of alteration paths expected on surface outcrops and under subsurface in-situ conditions.

4.2 CRYSTAL GEYSER: GEOLOGICAL SETTING, ROCK DIAGENETIC HISTORY, AND SAMPLING

The Crystal Geyser field site near the town of Green River in eastern Utah has been widely utilized as a CO_2 sequestration analog (e.g. Heath et al., 2009; Wilkinson et al., 2009; Burnside et al., 2013). Here, CO_2-charged brine sourced from rocks in the deep subsurface Paradox Basin migrates up along normal faults, including the Little Grand Wash Fault, and mixes with meteoric water from the shallower Navajo aquifer before reaching the surface in a series of fault-related seeps or through a small number of abandoned wells (Wilkinson et al., 2009). The roughly E-W striking normal faults dominantly dip southward and cut a series of Mesozoic siliciclastic rocks within the broad, gently northward plunging Green River Anticline (Dockrill and Shipton, 2010). A series of actively precipitating and fossil travertine mounds paralleling the normal faults are products of the CO_2 seeps active for at least 400 ka (Burnside et al., 2013).

The Little Grand Wash Fault near Crystal Geyser exposes primarily the Jurassic Summerville Formation, a marginal marine siltstone with carbonate and mudstone beds, and the Morrison Formation, including the Brushy Basin (dominantly mudstone) and Salt Wash (dominantly coarse-grained sandstone interbedded with mudstone) members. The Cretaceous Mancos shale is exposed in the hanging wall. The Salt Wash Graben located 10 km to the south of Little Grand Wash exposes units slightly lower in the stratigraphic section including the Jurassic Entrada Sandstone. All these units have been altered in the vicinity of the fault, resulting mostly in hematite dissolution and calcite precipitation that has been attributed to CO_2-brine-rock interactions (Urquhart, 2011; Wigley et al., 2012;

Major et al., 2014, in review). Localized calcite precipitation in the vicinity to faults has been attributed to CO_2 degassing of ascending CO_2-charged brine (Urquhart, 2011).

Rock samples selected for this study include both CO_2-altered (bleached) and unaltered (red) Entrada sandstone, CO_2-altered and unaltered Summerville Formation siltstones, and CO_2-altered and relatively unaltered Mancos shale. Altered/unaltered sample pairs were taken from outcrops (either adjacent to each other or from similar stratigraphic levels) in near and far proximity to the fault and travertine mounds (See details in Table 4.1 and locations in triangles in Figure 4.1). The field sampling strategy was based on recognition of bleaching and/or proximity to conduits (i.e. travertine mounds), then confirmed analytically by XRD and petrologic analyses. All samples were retrieved from blocks excavated in the sampling points about 10 cm away from the surface to minimize alterations from surface weathering. The following petrographic description corresponds to rocks sampled at the locations shown in Figure 4.1.

Table 4.1: Locations of rock sampling with respect to faults associated with CO_2-charged brine seepage. See satellite image of sampling location in Figure 1.

Lithology	Unaltered	Altered
Entrada Sandstone	JE1: 100 m away from fault (samples ~2 m above JEb1)	JEb1: 100 m away from fault Same place of unaltered sample but different depth
Summerville Siltstone	JS2: 150 m away	JSa1: Beneath travertine mound about 2 m away from fault conduit (foot wall)
Mancos Shale	KM4: 3 km south of fault	KMa1: Few meters from fault beneath travertine mound (hanging wall)
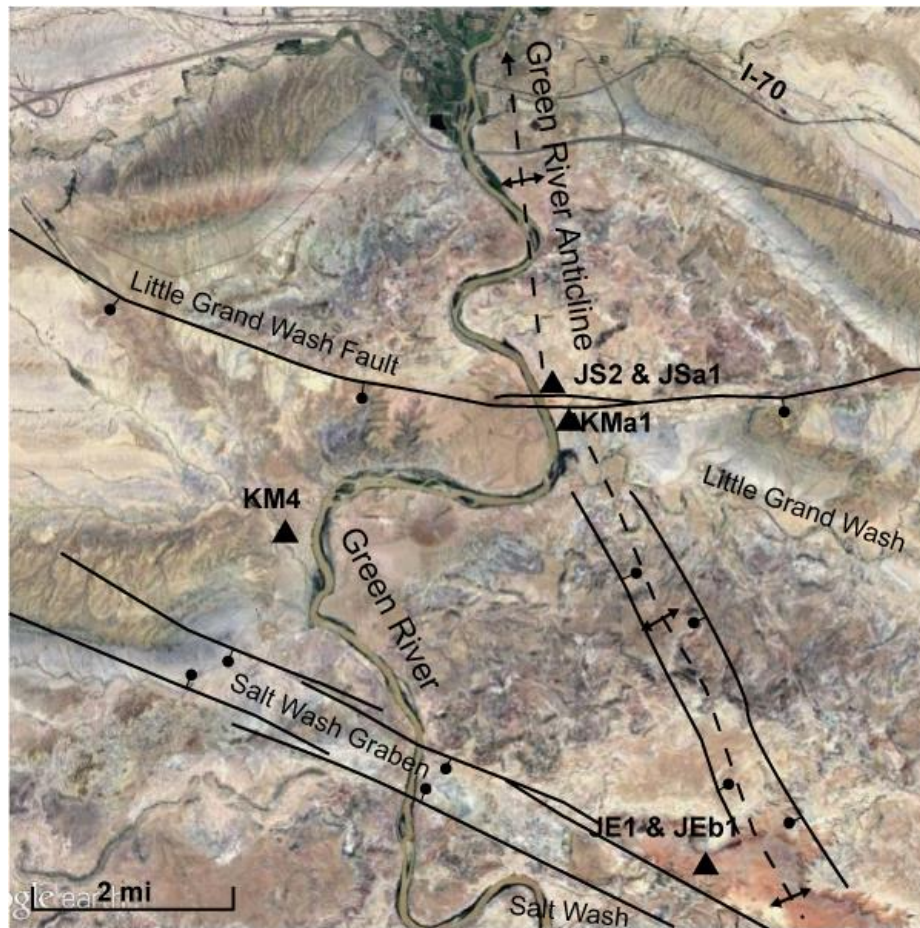
Figure 4.1: Simplified geologic map and satellite image (credit Google Earth) of the Crystal Geyser field site near Green River, Utah showing location of major structural features and locations of rock sampling. Entrada Sandstone samples were collected from Salt Wash Graben, whereas the other samples described were collected closer to Crystal Geyser and Little Grand Wash Fault.

Entrada sandstone: Unaltered entrada sandstone at Crystal Geyser consists of eolian dune deposits of well-sorted fine-to-medium grained reddish sandstone (~55 wt% Quartz, 24 wt% clays, 14 wt% carbonates, 7 wt% K-feldspar, plus trace minerals). Burial and diagenesis resulted in sub-angular to rounded grains with development of hematite, goethite, and illite-smectite grain coatings. Primary carbonates take about 5.5%wt of

mineral composition in the form of sparry calcite. Flow of CO2-charged brine resulted in bleaching of red Entrada Sandstone causing hematite dissolution (with ensuing trace metal mobilization), dissolution of preexisting carbonate and silicate minerals and formation of secondary clays and carbonates (Wigley et al., 2012).

Summerville Siltstone: Unaltered Summerville siltstone is a reddish siltstone with minor shale and limestone beds. The siltstone matrix is composed by very fine-grained quartz grains in a matrix formed principally by sparry calcite, illite-smectite, and feldspar; natural heterogeneity results in variations of carbonate content from 23 wt% to 43 wt% (Aman et al., 2017; Major et al., 2014). Samples of altered Summerville siltstone collected in the proximity of faults and below travertine mounds exhibit similar amounts of carbonate content but cementation is in the form of fine-grained micritic calcite and clays. Altered Summerville samples also have a distinct color with respect to unaltered Summerville as a result of bleaching and changes in mineralogy. In addition, some altered samples exhibit mineralized veins (example in Figure 4.5).

Mancos Shale: Mancos Shale is a regionally extensive gray marine shale, with a few silty layers exposed near the field site. Samples of Mancos Shale collected far from CO_2 springs exhibit a matrix dominated by fine quartz (64 wt%), feldspar and clay minerals (illite, illite/smectite, chlorite/smectite, and kaolinite). Retrieved unaltered Mancos samples exhibited open fractures likely resulting from a combination of surface exhumation and sample preparation (Figure 4.7). In contrast, Mancos Shale samples retrieved in proximity to faults exhibit large amounts of matrix calcite (~50 wt%) with decreased amount of clay

minerals. At larger scales, altered Mancos shale shows straight mm-thick mineralized veins separated by ~0.5 m. Despite the presence of these discontinuities, the retrieved altered Mancos samples did not show any open fractures observable with the X-ray microtomograph.

4.3 TRIAXIAL TESTING

4.3.1 Rock samples

Table 4.2 summarizes details from all samples tested and experiments conducted. All samples are cylindrical and have a nominal diameter of 25 mm. Entrada and Summerville samples were prepared to have a length to diameter ratio between 2:1 and 2.5:1 consistent with material testing standards (ASTM D7012). Mancos shale samples were limited in quantity and size; the tallest unaltered Mancos shale available for testing is 34.8 mm. Short samples are significantly affected by shear friction at loading caps, while long samples may present buckling instabilities under axial compression.

Table 4.2: List of tested rock samples and test results. Codes in parentheses refer to rock type as in Major et al., 2014. (*) Calculated from weight, bulk volume, and mineralogical composition from Major et al., [in review].

Lithology	Sample ID	Length [cm]	Diameter [cm]	Weight [g]	Porosity* [%]	Triaxial Test Type	Confining Stress σ_3 [MPa]	Axial stress σ_1 (peak) [MPa]	Loading E [GPa]	Loading ν [-]	Unload. E [GPa]	Unload. ν [-]	Mode of Failure
Entrada Sandstone Unaltered (JE1), Composition wt%: Q 55, Feld 7, Cal 7, Dol 7, Clays 24	EU1	5.37	2.544	67.07	8.7	Standard	0.69	70.9	6.1	0.43	16.6	0.19	Brittle, strongly strain-softening
	EU2	5.30	2.535	66.33	7.9	Standard	0.69	50.7	8.9	0.29	21.4	0.16	Brittle, strongly strain-softening
	EU3	5.17	5.537	64.24	8.6	Standard	0.69	82.6	8.9	0.42	19.1	0.12	Brittle, strain-softening
	EU4	5.41	2.542	67.75	8.4	Standard	6.9	115.8	11.2	0.36	23.0	0.17	Brittle, strongly strain-softening
	EU5	5.60	2.542	70.16	8.2	Standard	6.9	102.2	11.0	0.28	23.2	0.14	Brittle with two peaks, strain softening after
	EU7	5.72	2.545	71.97	8.1	Standard	20.7	179.3	17.0	0.25	35.2	0.19	Brittle, strongly strain-softening
Entrada Sandstone Altered (JEb1) Composition wt%: Q 58, Feld 5, Cal 4, Dol 6, Clays 27	EA1	5.47	2.537	65.39	11.7	Standard	0.69	61.7	6.3	0.25	14.6	0.32	Brittle, strongly strain-softening
	EA2	5.39	2.538	64.68	11.4	Standard	0.69	42.9	6.2	0.30	12.9	0.19	Brittle, strongly strain-softening
	EA8	5.33	2.530	63.56	11.4	Standard	0.69	68.7	8.4	0.44	NA	NA	Brittle, strongly strain-softening
	EA4	5.55	2.545	66.6	11.9	Standard	6.9	101.3	9.7	0.34	17.1	0.23	Brittle, strongly strain-softening
	EA7	4.95	0.527	58.88	11.4	Standard	6.9	94.3	11.9	0.27	23.7	0.18	Brittle, strongly strain-softening
	EA3	5.30	2.535	63.37	11.5	Standard	20.7	159.6	13.9	0.18	NA	NA	Brittle, strongly strain-softening
	SU1	5.19	2.57	68.82	3.5	Standard	0.69	152.3	36.2	0.26	47.3	0.18	Brittle, strongly strain-softening
	SU2	5.04	2.57	66.85	3.6	Standard	0.69	173.0	39.2	0.27	52.2	0.16	Brittle, strongly strain-softening

71

Table 4.2: Continued

						Test							
Summerville Siltstone Unaltered (JS2)	SU3	5.21	2.57	67.75	5.3	Multistage	0.69, 6.9, 20.7	158.4, 200.7, 221.5	39.1, 44.0, 43.5	0.20, 0.25, 0.23	54.2, 55.4, 55.8	0.08, 0.10, 0.16	No post-peak information
Composition wt%: Q 59, Feld 8, Cal 23, Clays 10	SU4	5.21	2.57	66.60	6.9	Multistage	0.69, 6.9, 20.7	142.8, 186.1, 227.0	33.4, 40.2, 42.0	0.29, 0.35, 0.27	45.0, 54.7, 55.1	0.15, 0.19, 0.21	No post-peak information
Summerville Siltstone Altered (JSa1)	SA1	5.13	2.57	63.99	9.8	Standard	0.69	26	8.2	0.30	15.4	0.22	Ductile, slightly strain-softening
	SA2	4.70	2.57	58.35	10.1	Standard	0.69	9.4	2.3	0.32	5.3	0.21	Ductile, perfect-plastic followed by strain softening
Composition wt%: Q 32, Feld 17, Cal 38, Clays 13	SA3	4.78	2.57	58.87	10.8	Multistage	0.69, 6.9, 20.7	24.5, 59.2, 116.7	5.2, 8.4, 9.9	0.06, 0.10, 0.13	14.0, 16.8, 22.0	0.14, 0.15, 0.19	No post-peak information
	SA4	4.79	2.57	59.36	10.3	Multistage	0.69, 6.9, 20.7	27.5, 50.6, 109.4	6.7, 7.2, 8.5	0.21, 0.21, 0.20	15.8, 16.5, 22.8	0.29, 0.33, 0.39	No post-peak information
Mancos Shale (KM4)	MU1	3.49	2.507	42.84	6.0	Standard	0.69	51.7	4.9	0.28	15.0	0.13	Brittle with microfractures, strain-hardening
Composition wt%: Q 64, Feld 15, Cal tr Clays 20	MU2	2.89	2.502	35.05	6.7	Loading no-failure	0.69	NA	0.7	0.11	NA	NA	No post-peak information
	MU3	2.90	2.450	34.04	5.9	Loading no-failure	0.69	NA	4.1	0.16	NA	NA	No post-peak information
Mancos Shale Altered (KMa1)	MA1	4.57	2.518	57.46	6.0	Standard	0.69	48.2	8.5	0.27	17.3	0.18	Brittle with multiple microfractures
Composition wt%: Q 16, Feld 9, Cal 50, Dol 1, Clays 20	MA2	3.48	2.519	43.59	6.6	Loading no-failure	0.69	NA	11.85	0.17	17.5	0.22	No post-peak information

4.3.2 Triaxial frame and deviatoric loading procedure

We conducted tests in an ultra-stiff (10^7 N/mm) triaxial frame manufactured by TerraTek and equipped with local strain transducers (set of cantilever arms) to measure bulk axial and radial strains. Servo-hydraulic systems control confining stress σ_3 and deviatoric stress σ_1-σ_3.   We conducted two types of tests: standard constant axial strain rate tests at a constant confining stress, and multistage experiments with axial loading at multiple confining stresses utilizing the same sample. Table 4.2 specifies the type of test run on each sample. Standard tests pursued clear evidence of post-peak behavior. The multistage test consists of stages of deviatoric loading, each one to the onset of sample dilation (based on volumetric strain measurements) before unloading and reloading at a higher confining stress (Alsalman et al., 2015, Ramos et al., 2017). Multistage triaxial tests are useful to define the failure envelope with a limited number of samples. Short unloading paths served to measure elastic rock rebound and characteristic elastic coefficients. All samples were air-dry, hence, pore pressure is negligible and all reported stresses are Terzaghi effective stresses. Deviatoric loading proceeded at an axial strain rate of $4{\cdot}10^{-6}$ s^{-1} in all tests. We chose effective confining stresses equal to 0.69 MPa (100 psi), 6.9 MPa (1,000 psi), and 20.7 MPa (3,000 psi) for our triaxial tests based on typical values to study friction-strengthening behavior of geomaterials and potential brittle to ductile transition in sandstones and shales. A confining stress of 6.9 MPa is more or less equivalent to a horizontal effective stress developed at about 1.6 km of depth in an on-shore sedimentary basin with hydrostatic pore pressure and no tectonic strains.

75

Data reduction utilizes a linear Coulomb criterion to characterize shear strength, such that,

$$\sigma_1(\text{peak}) = UCS + q \cdot \sigma_3 \qquad\qquad\qquad \text{(Eq 4.1)}$$

where *UCS* is the unconfined compressive strength, *q* is a friction parameter, and φ is the friction angle, such that $q = (1+\sin\varphi)/(1-\sin\varphi)$. The *UCS* [MPa] quantifies the level of cementation strength in the sample and φ [-] quantifies the increase in rock shear strength due to effective mean compressive stresses (Jaeger et al., 2009). We calculate Young's modulus *E* and Poisson's ratio *v* assuming material isotropy:

$$E = \left.\frac{\Delta\sigma_1}{\Delta\varepsilon_1}\right|_{\sigma_3} \qquad\qquad\qquad \text{(Eq 4.2)}$$

$$v = -\left.\frac{\Delta\varepsilon_3}{\Delta\varepsilon_1}\right|_{\sigma_3} \qquad\qquad\qquad \text{(Eq 4.3)}$$

where ε_1 and ε_3 are the strains along the maximum and least principal directions. The Young's modulus *E* [GPa] quantifies the stiffness of the rock and is proportional to degree of cementation and grain contact overlap; while *v* quantifies strains (and stresses if confined) perpendicular to the applied stress (Gueguen and Palciauskas, 1994). The reported loading elastic coefficients correspond to tangent measurements before departure from linearity and unloading coefficients correspond to the average of at least two unloading cycles.

4.3.3 Results

4.3.3.1 Entrada sandstone

The strain-stress results for standard tests in Entrada sandstone samples at various effective confining stress σ_3 are available in Figure 4.2a. We discarded two tests in altered Entrada

76

sandstone that showed unexpectedly low peak stress values (σ_1-σ_3 = 21.35 MPa at σ_3 = 6.9 MPa and σ_1-σ_3 = 49.56 MPa at σ_3 = 20.7 MPa) likely due to a failed confinement or a pre-existing weakness induced or not detected before triaxial testing. Unaltered samples appear stronger on average than CO_2-altered bleached samples, although natural heterogeneity contributes to scatter in the data. The tests run at σ_3 = 0.69 MPa show well defined peak stresses followed by rapid strain softening in both unaltered and altered samples. Post-peak behavior of unaltered samples conducted at higher confining stress show rapid strain softening as well. The weakest bleached samples show gradual strain softening after peak stress. Figure 4.2b shows an average unconfined compression strength reduction (UCS – Eq. 1) of about 14% in altered samples in comparison with unaltered samples. The difference in the friction parameter q is about 10%. The experimental data of Entrada Sandstone show dilation (0.8% to 0.4% from onset of dilatancy to peak stress decreasing with confining stress). Dilation is associated with grain rotation and fracture opening rather than grain crushing. Altered Entrada sandstone dilates less than unaltered entrada Sandstone, which suggests weakening and increased porosity in altered Entrada Sandstone with respect to unaltered Entrada.
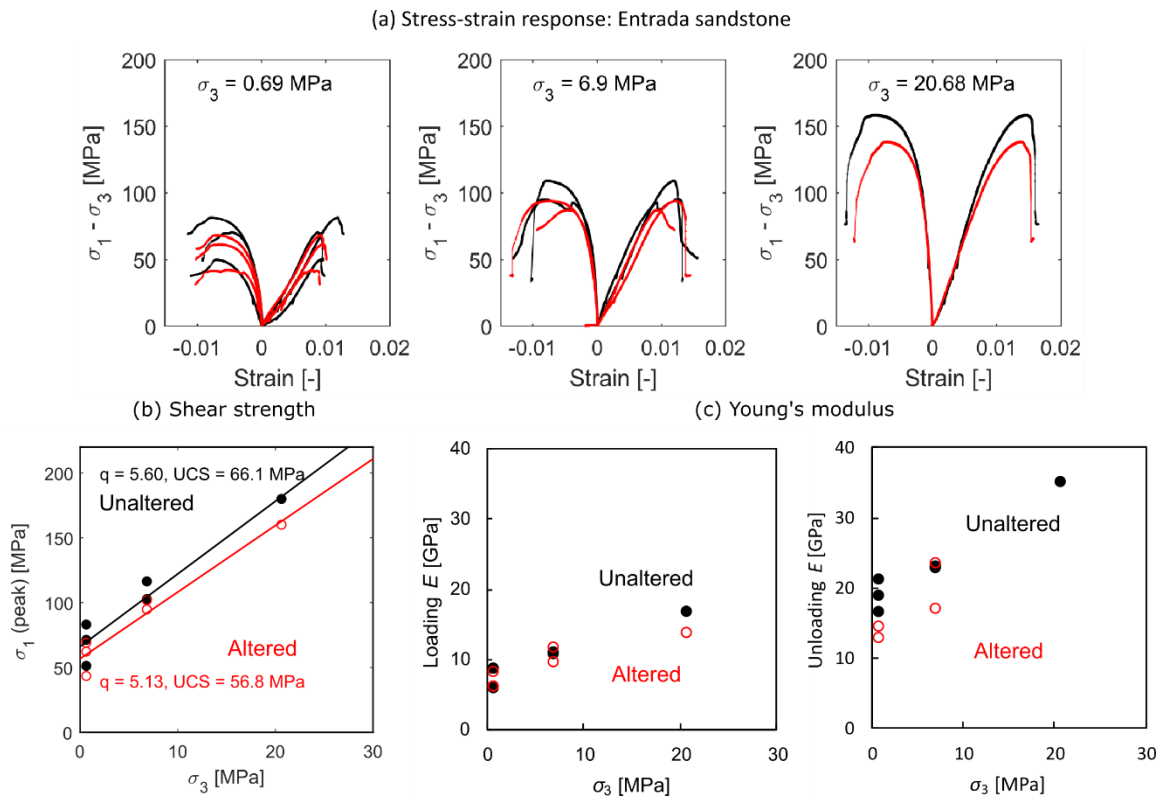
Figure 4.2: Mechanical response of unaltered (black) and altered (red) Entrada sandstone at various confining stresses σ_3. Axial strains are positive and radial strains are negative. (a) Stress-strain response. (b) Shear strength. (c) Loading and unloading Young's moduli. Altered samples are weaker –in average– and more ductile than unaltered samples.

Similar to strength trends, a number of CO_2-altered Entrada sandstone samples are softer (lower Young's modulus) than unaltered Entrada (See Figure 4.2c and Table 4.2). The loading and unloading Young's moduli of altered rocks are similar but typically lower than the moduli of unaltered rocks (Figure 4.2c).

78
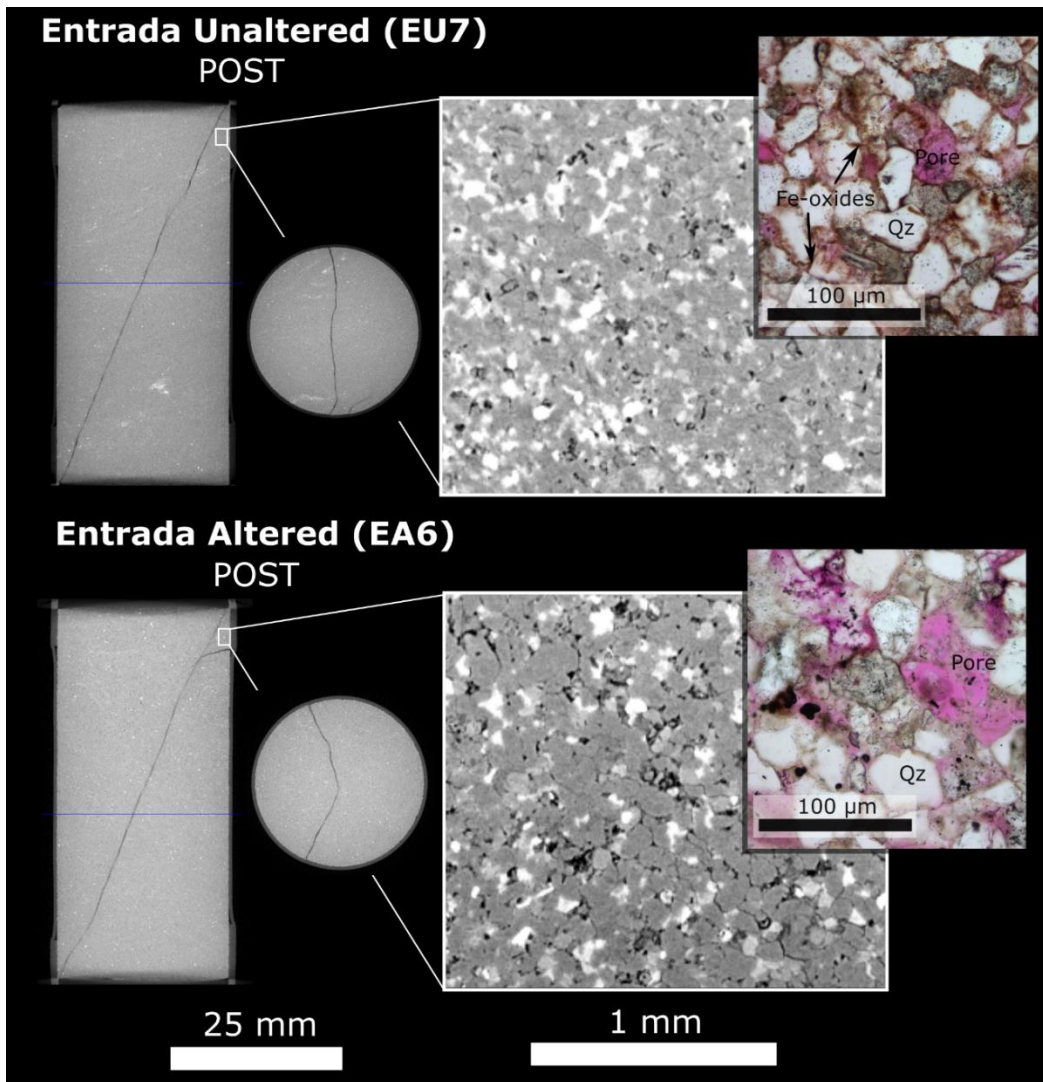
Figure 4.3: X-ray computed tomography slices of Entrada Sandstone samples post-deviatoric loading ($\sigma_3 = 20.7$ MPa). Samples showed clear shear fractures propagating from the ends toward the middle with and without coalescence. Mineral heterogeneities did not seem to affect damage localization. High magnification CT slices shows porosity (black), quartz, carbonates, clay (gray), and detrital mafic clasts (white). Microphotographs highlight the absence of grain-coating cementing iron-oxides in bleached (altered) Entrada Sandstone (pink color represents porosity).

Figure 4.3 shows X-ray micro-tomographic images of samples EU7 and EA6 after testing

to peak stress at $\sigma_3 = 20.7$ MPa. Strain localization concentrates in two planes at

characteristic angles corresponding to shear failure. Careful inspection shows that fractures originating from edges of the sample do not perfectly align but seem to coalesce upon a slight change of direction (top third in EU7 and lower fourth in EA6). Samples tested at lower confining stress exhibit similar patterns with clear shear fractures oriented at about the same angle: $72.4 \pm 2.9°$ in unaltered Entrada samples and $72.2 \pm 3.7°$ in altered Entrada samples (considers individual fractures, not average after coalescence). Sample heterogeneity mostly comprised of weak lamination does not seem to affect strain localization and damage evolution. High magnification tomographic slices show higher porosity and less cementation in altered samples than in unaltered samples.

4.3.3.2 Summerville siltstone

Figure 4.4a shows the strain-stress results from testing Summerville siltstone samples with standard tests at $\sigma_3 = 0.69$ MPa (100 psi), and multistage tests at $\sigma_3 = 0.69$ MPa (100 psi), 6.9 MPa (1,000 psi), and 20.7 MPa (3,000 psi). Results clearly show a weaker altered Summerville siltstone samples than unaltered samples. Both rock strength and stiffness undergo 7 to 10 fold decrease with rock alteration (See Table 4.2). Standard tests at $\sigma_3 = 0.69$ MPa show clear differences in strength, stiffness, and post-peak behavior between unaltered and altered samples (Figure 4.4a-c). Multistage testing at various confining stresses confirm marked reduction of rock strength and yield stresses in altered samples. Cohesive strength reduces about 8 fold, yet samples possess similar internal friction angles (Figure 4.4b).
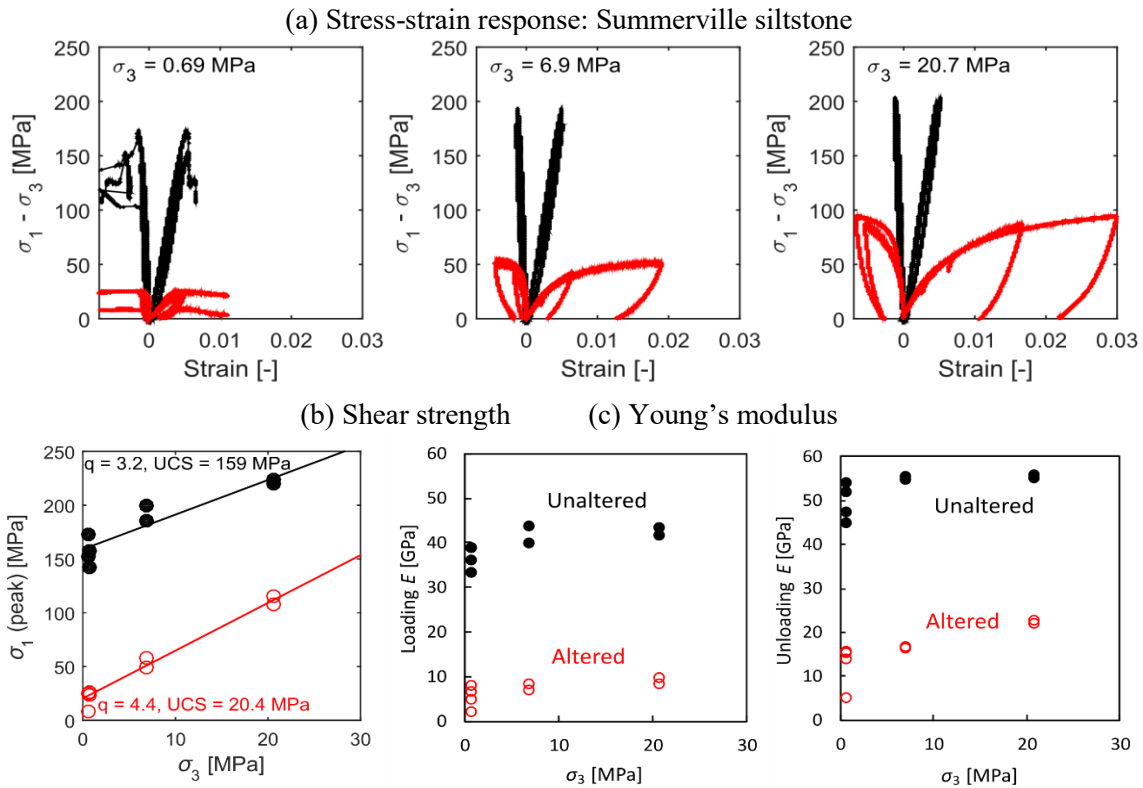
Figure 4.4: Mechanical response unaltered (black) and altered (red) Summerville siltstone at various confining stresses σ3. Axial strains are positive and radial strains are negative. The multistage experiments finish with deviatoric unloading at a fixed strain rate. (a) Stress-strain response. (b) Shear strength. (c) Loading and unloading Young's moduli. Altered samples show clear weakening and more ductile behavior compared to unaltered samples.

X-ray micro-tomographic images of Summerville siltstone samples help explain failure patterns (examples SU2 and SA2 in Figure 4.5). The unaltered sample SU2 shows various planes of failure combining apparent splitting and inclined shear fractures. The presence of multiple fractures likely corresponds to small brittle events (rapid drop of deviatoric stress) observed in strain-stress response of unaltered Summerville samples at σ3 = 0.69 MPa. The altered samples show marked heterogeneities comprised by distinct layers and partially mineralized fractures, some of them which likely associate with proximity to the

81

fault gouge (Table 4.1 and Figure 4.1). These heterogeneities contributed the branching and turning of fractures during failure. Despite an apparent "ductile" stress-strain signature up to $\varepsilon_1 \sim 0.03$, altered Summerville Siltstone samples showed a significant number of fractures, typical of brittle failure. X-ray tomographic inspection of unaltered siltstone samples after multistage testing at various confining stresses do not show observable fractures and discontinuities. This observation suggests that multistage testing did not take unaltered Summerville samples to stresses close to ultimate strength.
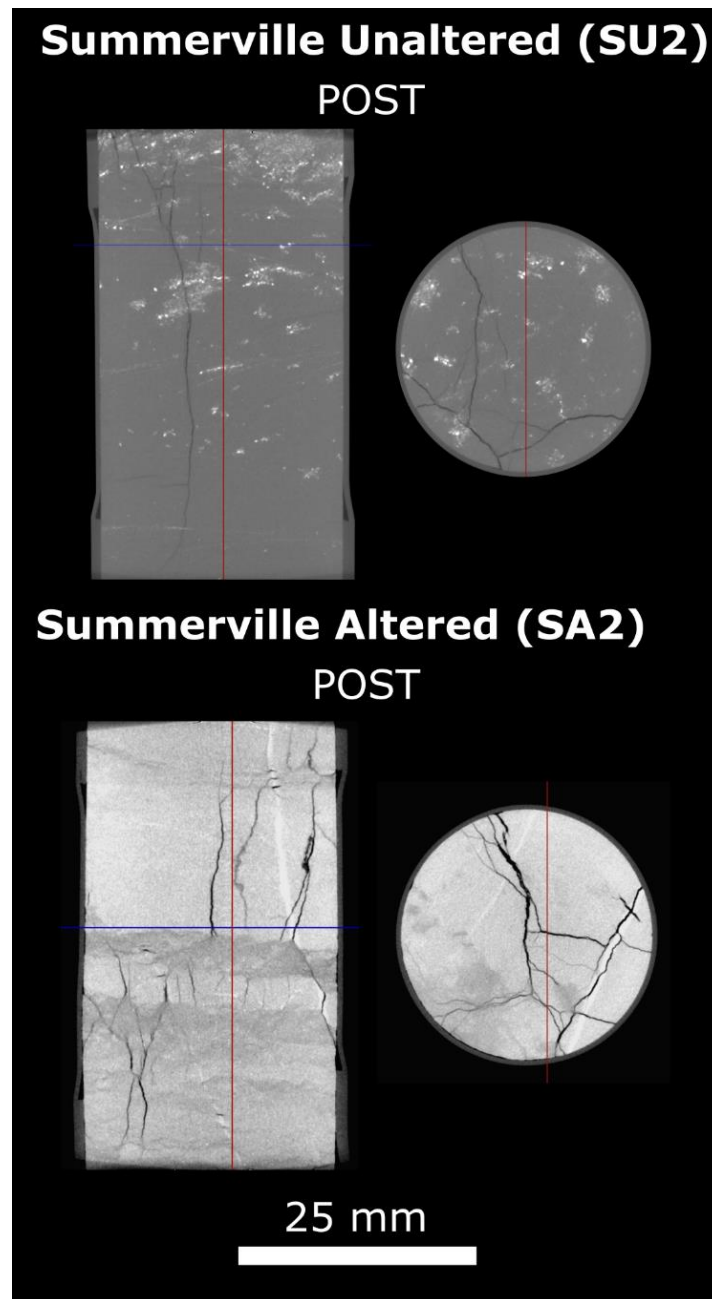
Figure 4.5 X-ray computed tomography slices of Summerville Siltstone samples post-deviatoric loading ($\sigma_3 = 0.69$ MPa). (a) Unaltered samples were mostly homogeneous with patches of detrital mafic clasts (bright mineral phase in CT slices) and exhibited various shear and tension planes upon failure. (b) Altered samples showed marked heterogeneities including layering and partially mineralized fractures, both of which altered strain localization during failure.

4.3.3.3 Mancos shale

Stress-strain results of Mancos shale samples at confining stress $\sigma_3 = 0.69$ MPa (100 psi) show that shale samples exposed to CO_2-charged brine in the vicinity if the fault are stiffer than the unaltered Mancos samples more distal from the fault (Figure 4.6 and Table 4.2). The altered samples also exhibit smaller difference of unloading versus loading Young's modulus than altered samples. We limited testing to a predetermined stress for short samples (MU2, MU3, MA2). Indeed, the observed peak stresses for MU1 and MA1 are not suitable for rock strength comparison because the unaltered sample MU1 is too short to yield a reliable value of shear strength. MU2 was also stopped early because of unexpected early dilation. A thorough strength measurement was unattainable due to limitations in successful coring of large samples because of pre-existing open fractures, mostly in the unaltered Mancos shale blocks. Non-optimal sample size also influences the accuracy of measured elastic properties.
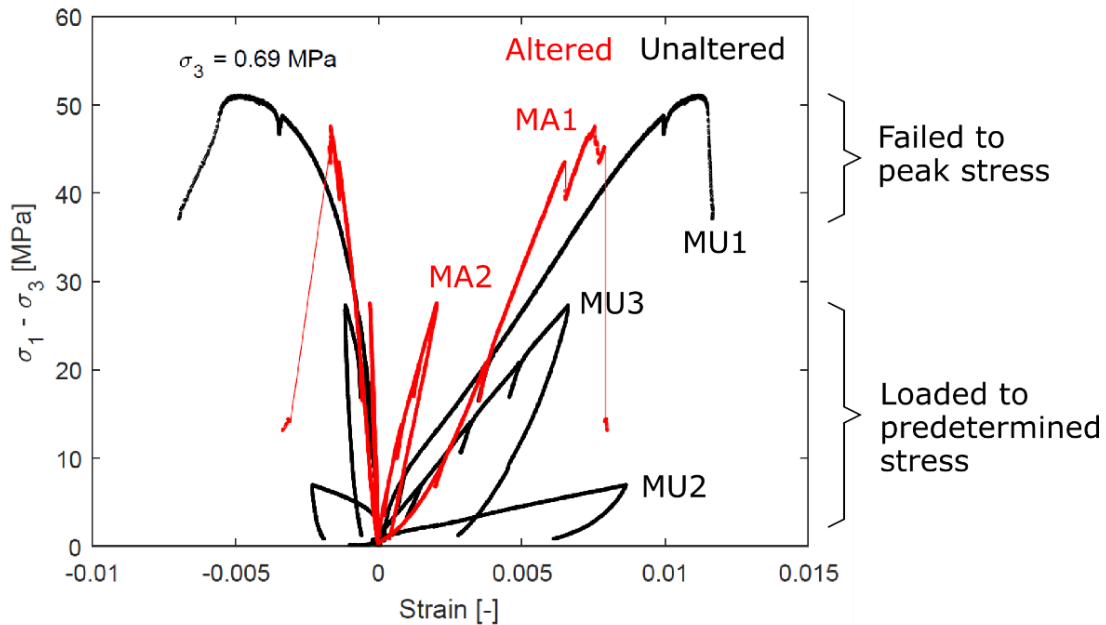
Figure 4.6: Stress-strain curves for Mancos shale unaltered (black) and altered (red) at an effective confining stress of 0.69 MPa (axial strains are positive and radial strains are negative). Altered samples are stiffer than unaltered samples. MA1 had a height to width ratio equal to 1.39 and therefore peak stress may not be representative of the rock shear strength. MU2, MU3 and MA2 were too short to obtain meaningful strength measurements.

Figure 4.7 shows X-ray micro-tomographic slices of Mancos shale samples before and after failure. Unaltered shale samples have numerous open pre-existing fractures along the bedding plane. Deviatoric loading in MU1 promoted growth of shear fractures that interacted with pre-existing weakness planes. The altered Mancos shale samples do not exhibit open fractures observable with micro-tomography. Altered shale samples have rare, closed sub-mm carbonate-filled veins, and gypsum filled fractures, the latter related to weathering and observed at the outcrop. These observations support higher stiffness observed in CO_2-altered Mancos shale than in unaltered Mancos shale with open fractures. Some open microfractures beyond the resolution of the microtomography may also exist,

85

as evidenced from the stiffening strain-stress response of MA1 (Figure 4.6). Linkages

between open and mineralized fractures are explored in Section 5.
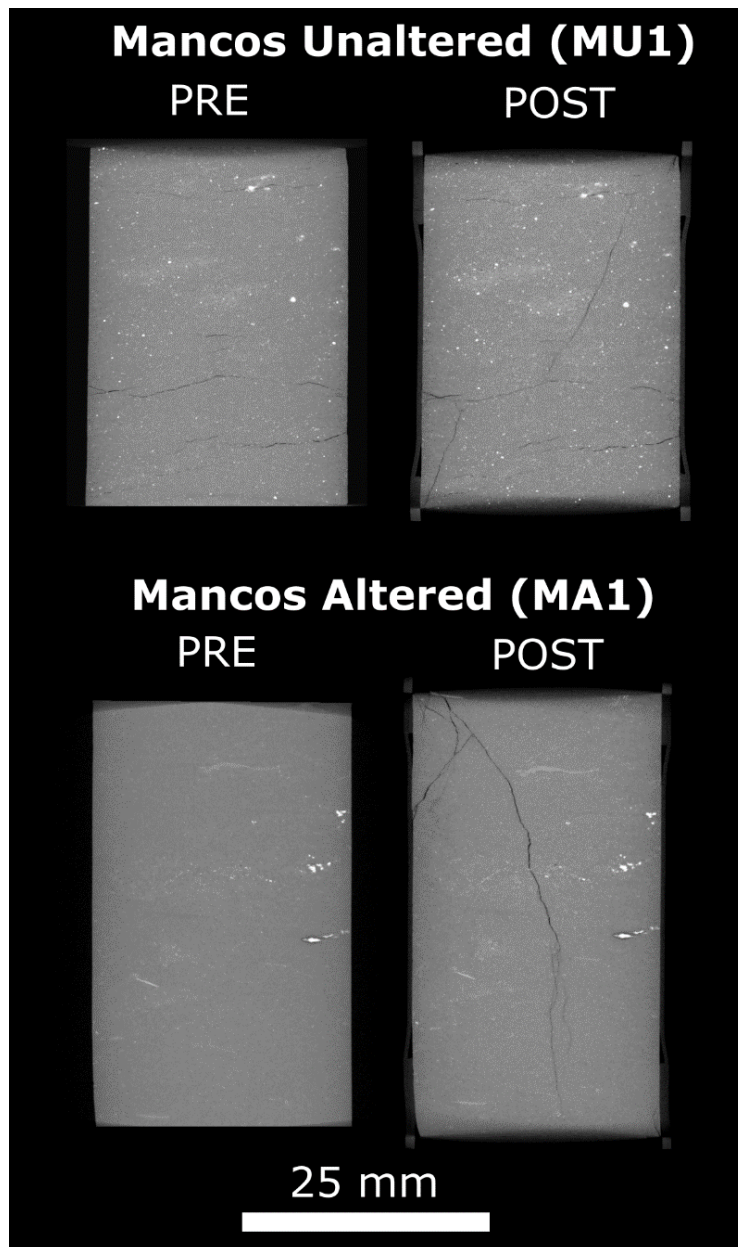
Figure 4.7: X-ray computed tomography slices of unaltered and altered Mancos shale samples pre- and post-deviatoric loading (σ_3 = 0.69 MPa). Unaltered samples show several pre-existing fractures along laminations which impacted rock stiffness and shear fracture initiation. Bright voxels correspond to pyrite and other Fe-bearing phases.

4.4 DISCUSSION

4.4.1 Origin of rock mechanical alteration and comparison with previous studies

Entrada sandstone. Previous work suggests dissolution of grain-coating hematite cement as the main factor for bleaching and weakening of Entrada sandstone (Major et al., 2014). Calcite dissolution and re-precipitation may also affect geomechanical properties. Unaltered and bleached Entrada Sandstone show velocity-strengthening slip behavior, unless significant carbonate precipitation occurs (Bakker et al., 2016). Both hematite and calcite dissolution are compatible with geochemical reactions in acidic environments (Eichhubl et al., 2004). Laboratory experiments show that CO_2-charged brine interaction with unaltered Entrada sandstone can result in localized carbonate dissolution and increases of porosity (Aman et al., 2017). As expected, there was no sign of pre-existing damage in Entrada samples (observed in X-ray microCT images) induced by the fault shear zone process (samples ~100 m away from fault). Our measurements indicate average porosity increases from 8.3±0.3% to 11.3±0.3% with alteration in Entrada sandstone. Triaxial test results presented here show weakening up to 14% of the unaltered rock stiffness and strength and agree with measurements based on indentation, scratching and double torsion techniques (Supplementary Information 3). A few samples of altered Entrada sandstone are as strong as (or stronger than) unaltered Entrada in triaxial tests (Figure 4.2). Such variation may be explained by the natural heterogeneity of the sandstone formation but also by variations in calcite dissolution and precipitation (such as in some portions close to the

fault (Bakker et al., 2016)). Our results document a small decrease in the internal friction coefficient as well.

Summerville siltstone. Hematite dissolution, calcite dissolution and precipitation as micritic cement, and increased amount of clay cements contribute to the weakening of Summerville siltstone. A significant increase of average porosity (Table 4.2) from 4.8±1.6% to 10.2±0.4% characterizes altered from unaltered samples. Laboratory studies show localized carbonate dissolution by CO_2-charged brine with ensuing increased porosity in unaltered Summerville Siltstone (Aman et al., 2017). In addition to changes in the rock matrix, X-ray tomographic images show the presence of mineralized natural fractures in altered Summerville that likely affected rock strength at the core scale (Figure 4.5). Pre-existing mineralized fractures usually constitute planes of weakness in rocks, because of lower shear and tensile bonding strength than the rock matrix (Gale et al. 2007, Lee et al., 2015). Pre-existing mineralized fractures may be the result of damage near the fault gouge and such alterations may also contribute to overall weakening of the retrieved altered Summerville samples (~2 m away from fault). The decreases of strength and stiffness up to 87% measured in triaxial tests are consistent with weakening measured through indentation and double torsion testing. Uncertainties in the determination of peak stress of unaltered Summerville siltstone in multistage testing do not permit unequivocally concluding about alterations of the internal friction angle (samples run only until onset of dilation). Yet, there appears to be little change of the internal friction angle if one disregards the data points at 20.7 MPa (Figure 4.4). A drop of ~38% in fracture toughness between

unaltered and altered Summerville siltstone was observed in double torsion mode-1 fracture mechanics tests by Major et al. (2014).

Mancos Shale. The unaltered Mancos shale samples are softer than the altered samples. One cause contributing to softening is the presence of pre-existing open fractures in unaltered shale as shown in X-ray tomography slices (Figure 4.7). The increase of stiffness up to +434% of altered Mancos with respected to unaltered –yet fractured– Mancos may be also aided by changes in the shale matrix. XRD analysis indicates calcite content increases by up to 50 wt% in altered samples in comparison to unaltered samples, the latter with much lower calcite amounts and higher clay content. The increased calcite content (Table 4.1) coincides with higher measured values of fracture toughness (Major et al., 2014).

4.4.2 Challenges of comparing mechanical properties of CO_2 naturally altered and unaltered rock outcrop samples

Our experimental results show evidence of differences in geomechanical properties between comparable rock lithofacies that have been exposed and unexposed to CO_2-charged brine. There is clear evidence of induced diagenesis by CO_2-charged brine on Crystal Geyser lithofacies (Wigley et al. 2012, Burnside et al. 2013). Some factors that could add uncertainty to the direct influence of CO_2-induced diagenesis in our comparison include the natural spatial variability of sedimentary rocks in vertical and horizontal direction, the presence of events that may postdate CO_2 alteration, the proximity of rock samples to faults, and effects of surface weathering.

90

We refer to our samples as unaltered and altered for simplicity. Yet, we acknowledge that some other factors may also be involved in the measured changes. The following actions and facts need to be taken into consideration to compare between the altered and unaltered lithofacies:

- Sampling of Entrada Sandstone took place in the same geographical location and same proximity to the leaking fault from different layers in the same stratigraphic succession.

- Sampling of Summerville Siltstone took place in the same stratigraphic layer but at different distance to the fault CO_2 leakage conduit. The proximity to the fault may have resulted in mechanical changes of rock fabric although such changes were not detectable in thin section petrography. Fracture networks resulted in extended reach of the CO_2-charged brine alteration beyond the reaction depth that it would be expected in a non-fractured medium (Kampman et al., 2016).

- Sampling of the Mancos Shale sample took place in similar stratigraphic layers but at different distances from the fault (Table 4.1). Similar to Summerville Siltstone, Mancos Shale also exhibits mineralized fracture networks in the proximity of the fault, not present far away from it.

All samples were excavated from beneath the immediate rock face in order to reduce the impact of surface weathering on rock diagenesis. Weathering effects would affect altered and unaltered samples equally. Observed diagenetic differences between altered and

unaltered samples are thus attributed to the variable water-rock interaction with distance from the CO_2 leakage fault conduits.

4.4.3. Field-scale implications of chemo-mechanical coupled processes in CO_2 reservoirs

The previous section provides evidence of compaction and horizontal stress relaxation due to load-bearing cement dissolution, as expected in some rocks exposed to CO_2-acidified brine. Significant strains caused by chemo-mechanical weakening (leading to compaction, shearing of wellbore casing, and subsidence) have yet to be observed in CO_2 injection field projects. Chemo-mechanical alteration under subsurface conditions can also result in stress changes in addition to those caused by pore pressure changes. For example, the Decatur site shows unexpected microseismic activity in the Mt. Simon reservoir sandstone and underlying basement rock well after CO_2 injection and related pore pressure transients (Bauer et al., 2016). In addition to pore pressure alterations, which are critical for safe CO_2 storage (Verdon et al., 2014; Jung et al., 2018), we hypothesize that one other possible mechanism for the seismic activity could be horizontal stress transfer to critically stressed basement faults arising from chemo-mechanical weakening of the overlying reservoir rock. Similar stress transfer mechanisms from the reservoir to adjacent formations occur during reservoir depletion, gas desorption from organic-rich rock, and rock cooling (Segall, 1989; Segall and Fitzgerald, 1998; Goulty, 2003; Espinoza et al., 2015; Paluszny et al., 2017). Small changes of minimum horizontal stress would have a direct impact on fault stability

for normal and strike-slip regimes but would not destabilize faults in reverse-faulting regime.

Dissolution of load-bearing mineral can also contribute to reduction of fracture toughness and thresholds for subcritical fracture propagation in both the reservoir and caprock (Major et al., 2014). Mineral dissolution also results in changes of rock strength and large-strain behavior – as observed in core scale experiments and DEM simulations. Even though dissolution may cause undesired strains and changes of stress in the reservoir, a large-scale change from brittle to ductile behavior could help avoid strain localization, high permeability channels, and rapid release of elastic energy (as induced seismicity) from the altered rocks. Conversely, mineral precipitation could lead to rock strengthening and fracture sealing.

The extent of coupled chemo-mechanical alterations is proportional to the extent of chemical reactions in the reservoir rocks. The injection of a finite amount of anhydrous CO_2 in a given reservoir results in distinct areas of CO_2-brine mixtures throughout the reservoir, with varying levels of bulk CO_2 saturation, brine saturation, salinity and pH (Kumar et al., 2005; Kneafsey and Pruess, 2010; Rohmer et al., 2016). Seepage through localized regions may result in flow of a significant number of pore volumes of CO_2-charged fluids, a situation unlikely in most of the CO_2 reservoir domains at depth (with exception of near-wellbore regions and areas of potential localized leaks). Hence, changes of rock properties (and expected changes of strain/stress) next to leakage paths represent end-members of chemo-mechanical alteration.

4.5. CONCLUSIONS

- This study shows experimental evidence of (1) reduction of stiffness, strength, and brittleness of Entrada sandstone and Summerville siltstone, and (2) increase of stiffness in Mancos shale after alteration with CO_2-charged brine.

- We tested outcrop rock samples that have been altered by fault-controlled percolation of CO_2-charged brines at the Little Grand Wash Fault, Crystal Geyser site, and compared against samples of lesser CO_2-brine alteration. Because of low overburden stress, rocks samples may have not undergone a directly coupled chemo-mechanical diagenesis. A different scenario is expected in a target storage formation under in-situ stresses and subsurface boundary conditions.

- The comparison of unaltered and altered lithofacies by CO_2 is appealing and instructive to elucidate long-term alteration mechanisms. However, several factors can affect a direct comparison. These include (in order of priority for our study): (1) distance to fault gouge and induced faulting strains and fractures, (2) location in the sequence stratigraphy and spatial variability in horizontal direction, (3) the presence of events that postdate CO_2 alteration, and (4) surface weathering.

- Extensive flow of CO_2-charged brine, such as in localized leakage pathways, can significantly alter the deformational behavior and mechanical properties of some sedimentary rocks.

- Early identification of CO_2-susceptible rocks and understanding of particle level mechanisms is helpful to avert undesired emergent phenomena from chemical and mechanical coupled interactions.

Chapter 5

Conclusions

This dissertation presents an investigation of geomechanical implications of CO_2 geological injection and storage in the presence of thermo-chemo-mechanical processes. The dissertation is based on three field case studies: Frio CO_2 injection pilot test in Dayton, Texas, Cranfield CO_2 sequestration in Cranfield, Mississippi, and Crystal Geyser outcrop sample test in Utah. Both Frio and Cranfield case studies are based on history-matched reservoir models and geomechanical analyses including experiments and numerical simulations. The first case study using Frio pilot test quantifies reservoir capacity to avert geomechanical failure in both near wellbore region and at reservoir bounding faults with an extended CO_2 injection scenario. The second case study, Cranfield project, focused on the thermo-chemo-mechanical impact of CO_2 injection on near-wellbore geomechanical integrity at the time scale of injection. The third case study -using rock samples from Crystal Geyser, Utah- examines the chemical effects of CO_2-charged brine to the host rock in geological time scale by conducting experiment of unaltered and altered rock pairs. The conclusions drawn from these studies are as follows:

- History-matched simulation of Frio CO_2 injection pilot test shows a considerable amount of dissolved CO_2 in brine, and the dissolution reduces tens-of-psi pore pressure buildup.

96

- Simulations demonstrates that fault reactivation is likely to occur after injecting 0.1 million tons of CO_2 assuming perfect compartmentalization, which is sixty times the amount injected at the Frio Pilot project.

- Maximum storage volume without fault reactivation and hydraulic fracturing decreases with the injection rates that follow a power law relationship according to extended sensitivity analyses.

- High reservoir permeability, high rock/pore compressibility, and low CO_2 viscosity prevent hydraulic fracturing of the injector in the Frio formation.

- Vertical heterogeneity in geomechanical properties such as elastic moduli and pore compressibility is critical to predicting local open-mode fractures near the wellbore region.

- Injection of CO_2 leads horizontal stress reduction in a near-wellbore region by lowering the temperature of rock and triggers an open-mode fracture at the injector in the Cranfield CO_2 injection site, which is confined by sealing layers.

- Sensitivity analysis shows injection temperatures and thermal expansion coefficients are critical to thermo-mechanical stress alteration to avoid fracture opening and large fracture propagation for CO_2 sequestration.

- Laboratory experiments demonstrate that CO_2-acidified brine induces enhanced creep in Tuscaloosa Sandstone – clay-rich sandstone – from Cranfield. However,

the short-term chemical effects on stress reduction are limited compared to that of thermal effects.

- Experimental studies on chemically altered and unaltered rocks in geological time from Crystal Geyser site show evidence of changes in deformational behavior mechanical properties including stiffness, strength, and brittleness after alteration with CO_2-charged brine.

- The samples from outcrops, loaded with less overburden stresses than in-situ stresses, may have not experienced direct coupled chemo-mechanical diagenesis. A different scenario is possible in a target storage formation under in-situ stresses.

- Diagnosing mineralogy of target formation with particle-level chemical reactions helps avoid undesired events from long-term CO_2 sequestration.

Appendix A

Frio CO₂ sequestration pilot test history matched simulation input files for IPARS

The version of IPARS used in this study is IPARSv3.1 with compositional fluid flow. As described in Chapter 1, the simulator solves material balance equation for compositional fluid flow, Darcy's law, and energy balance equation. The details of simulator can be found from Singh and Wheeler (2016).

A.1. Input file

```
TITLE(1)="CO2 STORAGE IN FRIO FAULTED GEOLOGICAL FORMATION"
TITLE(2)="Isothermal Test"

DESCRIPTION()=
"GRID BLOCKS : 50x78x71 (down, lateral, lateral) =    207,360 GRID ELEMENTS"

BLOCKMODEL(1)="COMPOSITIONAL_MODEL"


TIMEEND =1100.

$ I/O OPTIONS
$DEBUGS
$DEBUGM
OUTLEVEL = 3
$BUGKEY(6)
$BUGKEY(10)
$DUMPSTART = 999.0
$DUMPEND = 1000.0

$ NEWTON OPTIONS
MAXNEWT = 20

$ BCGS LINEAR SOLVER OPTIONS
$PRECOND = 3
$LINTOL = 1.0E-05
$LINTOL = 1.0E-03

$ GMRES LINEAR SOLVER OPTIONS
LSOL_TOL = 1.0E-06
LSOL_ITMAX = 500
GMRES_PREC = 16    $ AMG with LSOR.

$ WELL OUTPUT
```

WELLOUTKEY = 3   WELLFILE = "WELLS.OUT"   WELLFCUM = "WELLCUM.OUT"
$WELLOUTKEY = 0   WELLFILE = "CO2P3aSI.WEL"   WELLFCUM = "CO2P3aSI.CUM"

$ FAULT BLOCK AND MESH DATA
Include grid.dat

$ WATER PROPERTIES
WATERP = 14.7
WATFVF = 1.0
WATVIS = 0.2535
WATCMP = 3.3E-6
$WATCMP = 0.0
STDENW = 57.88

$ PHASE THERMAL CONDUCTIVITIES
PHTCOND(1,1 TO 3) = 48.5343
PHTCOND(2,1 TO 3) = 8.1714
PHTCOND(3,1 TO 3) = 10.8856
PHTCOND(4,1 TO 3) = 0.2203
$ ROCK ISOCHORIC SPECIFIC HEAT CAPACITY
ROCKCV = 0.17913

$ COMP NAMES
NHCOMP = 2
COMP(1) = "CO2"   COMP(2) = "BRINE"
LTCOMP = 1
ICINPH(,1) = 1 0 0
ICINPH(,2) = 0 1 1
ICINPH(,3) = 0 1 0
NXROCKS = 4
XMOL_DIFF(,,) = 0.0
XMOL_DIFF(,2,2 TO 3) = 0.5580

$ ROCK PROPERTIES
POROSITY1(,,)= 0.34
Include poroheterolarge.dat
$$ COMPNT. CRIT. PROPERTIES

$ CRITICAL TEMPERATURES
TCRIT(1 TO 2) = 547.5600   1165.2300

$ CRITICAL PRESSURES
PCRIT(1 TO 2) = 1070.3785   3203.8836

$ CRITICAL VOLUMES
ZCRIT(1 TO 2) = 0.274   0.22983

$ ACENTRIC FACTORS
$ACENT(1 TO 2) = 0.268   0.34400
ACENT(1 TO 2) = 0.2240   0.2440

$ MOL WEIGHTS
MOLWT(1 TO 2) = 44.0100   19.3537

$ PARACHOR

PARACHOR(1 TO 2) = 49.00   52.00
$ VOLUMETRIC SHIFT
VSHIFT(1 TO 2) = -0.19   0.0950
$ ISOBARIC SPECIFIC HEATS
HCCP(1 TO 2) = 14.8915   17.8176 $ for CO2, take mean of liq. & gas sp. heats.

$ BINARY INTERACTION COEFFICIENTS
BINACT(1,2) = -0.0602
BINACT(2,1) = -0.0602

$MODREL(1 TO 2) =   2

$ SURFACE CONDITIONS
TSURF = 57.694   PSURF = 14.7

$ INITIAL CONDITIONS
PORPRES1() = 14.7
Include init2.dat

$CONC1(,,,1) = 0.0
$CONC1(,,,2) = 1.0

$ SEPARATORS
PSEP(,1) = 14.7
TSEP(,1) = 57.694

$ SEPARATOR ASSIGNMENT FOR IN-PLACE CALCULATIONS
SEPSURF = 1

$ ROCK COMPRESSIBILITY
CR1() = 6E-6

$ FORMATION POROSITY AND PERMEABILITY

Include permheterolarge.dat

$ ROCK TYPES AND ROCK PROPERTIES
$ RELATIVE PERMEABILITY AND CAPILLARY PRESSURE TABLES

Include rock2.dat

$ WELLS
Include wellschedule2.dat

$ WELL OUTPUT FLAGS
$WOUTFLG(1 TO 24) = FALSE

$ NON-AQUEOUS COMPONENT WELL OUTPUT FLAGS
  $WELXOUT(1,1 TO 25)
  $WELXOUT(2,1 TO 25)
  $WXELOUT(1,2) = 7

$ INJECTION COMPOSITION
COMPINJ(,1) = 0.0 1.0 0.0

101

$ Uncomment below for equilibrium calc
$COMPINJ(,1) = 0.0 0.0 1.0

INJCOMP(1) = 1
$ TINJ(1) = 176.0

$ SEPARATOR ASSIGNMENT FOR WELLS
  IWSEP(1 TO 2) = 1

$ PRINTOUTS
  $OUT_MOLDW = TRUE
  $OUT_MOLD = TRUE
  OUT_VISCW = TRUE
  OUT_VISC = TRUE
  $ OUT_VISCO=TRUE
  $OUT_CO2LEAK = TRUE
  OUT_CO2MOL = TRUE
  XDARCYFLUX = TRUE

$PERMOUT
$VIS_SCL=3
$VISFLAG=7
$VIS_FNAME="PERM_"
$VIS_SCL_NAMES(1)="TCOFX"
$VIS_SCL_NAMES(2)="TCOFY"
$VIS_SCL_NAMES(3)="TCOFZ"

EndInitial

$ TRANSIENT DATA INPUT BLOCKS

BeginTime   0.0
    DELTIM = 0.01
    DTIMMUL = 1.1
    DTIMMIN = 1.0E-04
    DTIMMAX = 0.1
    TIMOUT = 0.1
    DTIMOUT = 0.1
    DSMAX = 0.9
    ICFL = 0

    $ VISUALIZATION
    VISOUT = 0.0   DVISOUT = 1.0
    VIS_SCL = 5
    VISFLAG = 7
    VIS_SCL_NAMES(1) = "PRES"
    VIS_SCL_NAMES(2) = "SGAS"
    VIS_SCL_NAMES(3) = "SWAT"
    VIS_SCL_NAMES(4) = "SOIL"
    VIS_SCL_NAMES(5) = "CO2"
    VIS_NVEC = 2
    VIS_VEC_NAMES(1) = "XVEL_GAS"
    VIS_VEC_NAMES(2) = "XVEL_OIL"
    VIS_FNAME = "frio_block_"
    $TIMRES = 80.0

```
        $DTIMRES =20.0
    EndTime

    BeginTime 80.0
    KINDWELL(3)=0
    KINDWELL(4)=0
    KINDWELL(5)=0
EndTime
```

A.2. Grid input

```
    BLOCKNAME(1) = "BLOCK1"

    $ FAULT BLOCK AND MESH DATA

    NX(1) = 50      NY(1) = 78        NZ(1) = 71
    DX(,1) = 2
    DY(,1) = 160 100 50 10 5 5 5 5 5 5 5 5 5 5 5 5 5 5 5 5 5 5 5 5 5 5 5 5 5 5 5 5 5 5 5 5 10 10 30 50 50 50 50
    50 50 50 50 50 50 50 50 30 10 10 10 5 5 5 10 30 50 100 250 300 250 100 50 30 10 5 5 5 10 35 50 100 200

    DZ(,1) = 1000 1000 500 300 300 150 80 55 10 10 10 5 5 5 5 5 5 5 5 5 5 5 5 5 5 5 5 5 5 5 5 5 5 5 5 5 5 5 5 5
5
    5 5 5 5 5 5 5 5 5 5 10 10 10 145 200 500 500 1000 1000 1000 4000 4000 4000 4000 4000 4000 4000 4000
    DOWN(,1) =      0.9511 -0.2367 0.1986
    $DOWN(,1) =     0.   0.   0.

XYZ111(,1) =   5020.          0.0000          0.0000
```

A.3. Well schedule

```
     $ WELLS AND BOUNDARY CONDITIONS
    NUMWELL =2

    WELLNAME( 1) = "WELL    1 MONITOR"
    $KINDWELL( 1) = 31 $production pressure specified
    $KINDWELL( 1) = 4 $production gas mass rate specified
    KINDWELL(1) = 37 $ production total volume rate specified (for restart file)
    DIAMETER(, 1) = 0.5
    WELLTOP(1 TO 3,1, 1) =       5045.     457. 3497.
    WELLBOTTOM(1 TO 3,1, 1) =      5063.     457. 3497.
    WELLPQ( 1) Block
      Interpolation Step
      Extrapolation Constant
      Data    0.0             0.0001,
    EndBlock

    WELLNAME(2) = "WELL 25 INJECTOR"
    KINDWELL(2) =    4 $gas injection mass rate specified
    $KINDWELL(2) =    4 $gas injection mass rate specified specified (for restart file)
    $gas injection, mass rate specified
    DIAMETER(,2) = 0.1
    PLIMITC(2) =        100000.0000
    WELLTOP(1 TO 3,1,2) =      5055    397. 3564.
    WELLBOTTOM(1 TO 3,1, 2) =      5073    397. 3564.
    WELLPQ(2) Block
```

Interpolation Step
Extrapolation Constant
Data
22   0.00001
1002.06 1482.078101
1002.09 2133.630464
1002.1 4397.520301
1003.176 4995.294015
1003.47 0.038908947
1003.68 4825.907806
1004.14 0.038908947
1004.32 4295
1005 0.038908947
1006.3 4194
1010.28 0.038908947
1011.03 2190
1011.18 0.038908947
1011.3 4500
1012.11 0.03
EndBlock

Appendix B

Geomechanics coupling method for CMG-GEM

The version of CMG used in this study is 2015 CMG-GEM coupled geomechanics including thermodynamics. CMG-GEM has a compositional fluid flow module based on several options of equation of state (EOS). The module chosen in this study is Peng-Robinson EOS and Henry's law to capture CO_2 dissolution into brine. The detailed parameters for EOS calculation are in Chapter 2, and also in Appendix C.

Mainly five governing equations are solved for fluid flow (mass balance for mixture-multiphase and Darcy's law and energy balance) and geomechanics (stress equilibrium including poroelasticity and thermoelasticity, strain-displacement relation, and constitutive relation) (Tran et al., 2009). In this version of simulator, there are four methods of coupling the geomechanics to fluid flow. The coupling method for fluid flow and geomechanics (formation deformation) that is used in this study is two way and sequential manner. That is two calculations alternate while passing information. The geomechanics module updates the formation deformation in response to the new pressures p, mean total stress σ_m, and temperatures T by updating porosity ϕ^{n+1}. The updated deformation goes back to the fluid flow calculation for use in the next time step. Porosity is calculated by the fluid flow module as function of pressure temperature, and the porosity is used to mass conservation calculation in each time step. Once the porosity is updated, the porosity is used for next

time step. The details of coupling algorithm and porosity equations are in Tran et al. (2009) and 2015 CMG-GEM manual.

Porosity equation:

$$\phi^{n+1} = \phi^n + \left(c_0 + c_2 \frac{2}{9}\frac{E}{1-v}\alpha c_b\right)(p - p^n) + \left(c_1 + c_2 \frac{2}{9}\frac{E}{1-v}\beta\right)(T - T^n)$$

where, $c_0 = f(V_b, \alpha, c_b, T, \sigma_m), c_1 = f(V_p, V_b, \beta), c_2 = f(V_b, c_b, \alpha)$.

V_b: bulk volume

V_p: pore volume

c_b: bulk compressibility

α: Biot coefficient

β: linear thermal expansion coefficient

v: Poisson's ratio

E: Young's modulus

σ_m: mean total stress

Appendix C

Cranfield CO₂ sequestration history matched simulation with thermo-elasticity input file using CMG-GEM

```
**   ==============   INPUT/OUTPUT CONTROL   ====================

*TITLE1 'GEM Geomechanics'
*TITLE2 'Geomechanics-Dependent Permeability'
*TITLE3 '3D Cartesian'

*INUNIT *FIELD

*WSRF *GRID 2
*WSRF *WELL 2
*OUTSRF *GRID    PERM POROS PRES SG
                            *SW *TEMP *POROS *YOUNG
                    *VERDSPLGEO *STRESI *STRESJ *STRESK
                        VDISPL W 'CO2' Y 'CO2' Z 'CO2'
                        *TSTRESI *TSTRESJ *TSTRESK
*INVENTORY-CO2
OUTSRF RES ALL
OUTSRF WELL PSPLIT
OUTSRF WELL PAVG
          GHGGAS
          GHGLIQ
          GHGSOL
          GHGSCRIT
          GHGTHY
WPRN GRID 0
WPRN WELL 0
WRST TIME

**   Distance units: ft
RESULTS XOFFSET               0.0000
RESULTS YOFFSET               0.0000
RESULTS ROTATION              0.0000   **   (DEGREES)
RESULTS AXES-DIRECTIONS 1.0 -1.0 1.0

**   ==============   GRID AND RESERVOIR DEFINITION   ================
GRID VARI 59 51 29
KDIR DOWN
DI IVAR
 5*660 400 360 6*330 2*130 40 27*20 40 2*130 6*330 360 400 5*660
DJ JVAR
 5*660 400 360 6*330 2*130 5*40 11*20 5*40 2*130 6*330 360 400 5*660
DK ALL
 3009*50 3009*30 3009*20 3009*10 6018*5 60180*3.6 3009*5 3009*15 3009*40

**top depth
DTOP
 3009*10313
```

DUALPERM
SHAPE GK

*TRANSFER 1
NULL *MATRIX CON   1

NULL FRACTURE CON   1
*MOD **$modifying fracture null block
 1:59   1:51   1:10   = 0
 1:59   1:51   13:29 = 0
 1:59   1:21   11:12 = 0
 1:59   31:51   11:12 = 0

*POR *MATRIX *KVAR   5*0.05 0.1097   4*0.178 2*0.181 2*0.2 0.2408 2*0.2 0.26 0.2408 0.1528
0.26   2*0.269   3*0.26 0.01 0.01 0.15
*POR *FRACTURE *KVAR   5*0.005 0.01097   4*0.0178 2*0.0181 2*0.02 0.02408 2*0.02 0.026
0.02408 0.01528 0.026   2*0.0269
                                                3*0.026 0.001 0.001 0.015   **
Fracture properties
*PERMI *MATRIX *KVAR   4*0.0001 0.00187   0.9144   0.1297   0.2770   2.9270   7.1105
        11.9379   17.6617   50.8940   29.4266   20.1713
                                        5.8337   1.0371   1.2347   1.1759   0.4066   2.6136
        0.001 21.4130 74.6762 2.2429 0.1077 0.07 0.0002 0.0001
PERMJ MATRIX EQUALSI
PERMK MATRIX EQUALSI * 0.1

*PERMI *FRACTURE *KVAR   4*0.0001 0.00187   0.9144   0.1297   0.2770   2.9270   7.1105
        11.9379   17.6617   50.8940   29.4266
                                20.1713   5.8337   1.0371   1.2347   1.1759   0.4066   2.6136   0.001
74.6762 2.2429 0.1077 0.1077 0.07 0.0002 0.0001
PERMJ FRACTURE EQUALSI
PERMK FRACTURE EQUALSI * 0.1
*DIFRAC CON 0
*DJFRAC CON 10
*DKFRAC CON 0
**   0 = pinched block, 1 = active block
PINCHOUTARRAY CON   1

*CROCKTYPE 1
 *CCPOR *MATRIX 2.35E-06
 *PRPOR *MATRIX 2000

*CROCKTYPE 2
 *CCPOR *MATRIX 2.40E-06
 *PRPOR *MATRIX 2000

*CROCKTYPE 3
 *CCPOR *MATRIX 2.19E-06
 *PRPOR *MATRIX 2000

*CROCKTYPE 4
 *CCPOR *MATRIX 2.24E-06
 *PRPOR *MATRIX 2000

*CROCKTYPE 5

```
  *CCPOR *MATRIX 2.27E-06
  *PRPOR *MATRIX 2000

*CROCKTYPE 6
  *CCPOR *MATRIX 2.04E-06
  *PRPOR *MATRIX 2000

*CROCKTYPE 7
  *CCPOR *MATRIX 2.17E-06
  *PRPOR *MATRIX 2000

*CROCKTYPE 8
  *CCPOR *MATRIX 8.03E-06
  *PRPOR *MATRIX 2000

*CROCKTYPE 9
  *CCPOR *MATRIX 2.68E-06
  *PRPOR *MATRIX 2000

*CROCKTYPE 10
  *CCPOR *FRACTURE 2.35E-06
  *PRPOR *FRACTURE 2000

*CROCKTYPE 11
  *CCPOR *FRACTURE 2.40E-06
  *PRPOR *FRACTURE 2000

*CROCKTYPE 12
  *CCPOR *FRACTURE 2.19E-06
  *PRPOR *FRACTURE 2000

*CROCKTYPE 13
  *CCPOR *FRACTURE 2.24E-06
  *PRPOR *FRACTURE 2000

*CROCKTYPE 14
  *CCPOR *FRACTURE 2.27E-06
  *PRPOR *FRACTURE 2000

*CROCKTYPE 15
  *CCPOR *FRACTURE 2.04E-06
  *PRPOR *FRACTURE 2000

*CROCKTYPE 16
  *CCPOR *FRACTURE 2.17E-06
  *PRPOR *FRACTURE 2000

*CROCKTYPE 17
  *CCPOR *FRACTURE 8.03E-06
  *PRPOR *FRACTURE 2000

*CROCKTYPE 18
  *CCPOR *FRACTURE 2.68E-06
  *PRPOR *FRACTURE 2000

  *CTYPE    *MATRIX *KVAR 6*8 4*1 2*2 2*3 4 2*3 5 4 6 5 2*7 3*5 3*9    **number*rocktype
```

```
  *CTYPE   *FRACTURE *KVAR 6*17 4*10 2*11 2*12 13 2*12 14 13 15 14 2*16 3*14 3*18
**number*rocktype

*END-GRID
**   ==============  FLUID DEFINITIONS   =====================
*MODEL     *PR
*NC     2     2
*TRES          262.000
*COMPNAME
            'CO2'            'CH4'
*SG         8.1800000E-01   3.0000000E-01
*TB        -1.0921000E+02 -2.5861000E+02
*PCRIT      7.2800000E+01   4.5400000E+01
*VCRIT      9.4000000E-02   9.9000000E-02
*TCRIT      3.0420000E+02   1.9060000E+02
*AC         2.2500000E-01   8.0000000E-03
*MW         4.4010000E+01   1.6043000E+01
*HCFLAG        0               0
*BIN
            1.0500000E-01
*VSHIFT     0.0000000E+00   0.0000000E+00
*VISCOR *HZYT
*MIXVC      1.0000000E+00
*VISVC      9.4000000E-02   9.9000000E-02
*VISCOEFF   1.0230000E-01   2.3364000E-02   5.8533000E-02 -4.0758000E-02
            9.3324000E-03
*OMEGA      4.5723553E-01   4.5723553E-01
*OMEGB      7.7796074E-02   7.7796074E-02
*PCHOR      7.8000000E+01   7.7000000E+01

*SOLUBILITY
** HENRYC calculated at     262.00 deg F
*HENRYC       1.0869039E+05   1.2170077E+06
*REFPH        4.5000000E+03   4.5000000E+03
*VINFINITY  3.6677118E-02   3.6830431E-02

*ENTHCOEF
            9.6880000E-02   1.5884300E-01 -3.3712000E-05   1.4810500E-07
           -9.6620300E-11   2.0738320E-14
           -2.8385700E+00   5.3828500E-01 -2.1140900E-04   3.3927600E-07
           -1.1643220E-10   1.3896120E-14

*AQUEOUS-DENSITY   *ROWE-CHOU
*AQUEOUS-VISCOSITY   *KESTIN
*THERMAL *ON
*TRACE-COMP 2
**   =============  ROCK-FLUID PROPERTIES   ====================
ROCKFLUID
RPT 1 *DRAINAGE **reservoir sandstone
**$        Sw        krw       krow
**         Sw        krw       krow        Pcow
SWT
        0.40       0.00       0          10
        0.4518    0.00271     0    4.487233333
        0.55      0.00605     0    2.634466667
        0.6001    0.01298     0    2.284085714
```

110

0.6492	0.02692	0	2.048155556
0.6777	0.03916	0	1.945608333
0.7003	0.05666	0	1.872040625
0.7258	0.07591	0	1.79424
0.7445	0.09693	0	1.740633333
0.7651	0.12321	0	1.6938
0.7817	0.1495	0	1.6606
0.7984	0.17754	0	1.620822222
0.816	0.21611	0	1.578777778
0.8288	0.2424	0	1.558117647
0.8425	0.27746	0	1.537970588
0.8562	0.31603	0	1.51623
0.868	0.34935	0	1.4944
0.8827	0.4002	0	1.467205
0.8983	0.45807	0	1.440454545
0.913	0.51769	0	1.418181818
0.9247	0.57206	0	1.400454545
0.9345	0.61765	0	1.39088
0.9433	0.65799	0	1.382432
0.9511	0.69482	0	1.375954167
1	1	0	1.375

```
**$      Sg        krg      krog
**       Sg        krg      krog
SGT
```

0.059	0.00	0
0.0836	0.0071	0
0.1101	0.0107	0
0.1435	0.0195	0
0.169	0.0301	0
0.1975	0.0477	0
0.226	0.0653	0
0.2506	0.0846	0
0.2762	0.1092	0
0.2998	0.1321	0
0.3234	0.1637	0
0.346	0.1935	0
0.3657	0.2234	0
0.3864	0.255	0
0.411	0.3007	0
0.4306	0.3428	0
0.4533	0.3885	0
0.4769	0.4411	0
0.4986	0.4956	0
0.5212	0.5588	0
0.5488	0.6342	0
0.5656	0.6852	0
0.5784	0.7273	0
0.5892	0.7676	0
0.6	0.7992	0

HYSKRG 0.4 **maximum trapped gas saturation

RPT 2 *DRAINAGE **caprock

**	Sw	krw	krow	Pcow
SWT				
	0.4	0.00	0	1740.45
	0.5	0.003	0	503.381
	0.551	0.00594	0	380.405
	0.601	0.00758	0	312.468
	0.645	0.01612	0	274.549
	0.678	0.02296	0	251.982
	0.705	0.03498	0	237.344
	0.736	0.0539	0	222.469
	0.765	0.07626	0	210.717
	0.784	0.09519	0	204.075
	0.811	0.12273	0	194.637
	0.834	0.15545	0	186.902
	0.85	0.18129	0	182.125
	0.865	0.20712	0	177.645
	0.883	0.23985	0	172.528
	0.903	0.28292	0	167.842
	0.918	0.326	0	164.328
	0.934	0.3639	0	160.989
	0.951	0.41215	0	159.328

**	Sg	krg	krog
SGT			
	0.05	0.0	0
	0.069	0.0018	0
	0.091	0.0018	0
	0.121	0.0053	0
	0.156	0.014	0
	0.186	0.0192	0
	0.212	0.0279	0
	0.249	0.04	0
	0.279	0.0573	0
	0.308	0.0712	0
	0.335	0.0902	0
	0.36	0.1075	0
	0.39	0.1317	0
	0.419	0.1576	0
	0.446	0.1852	0
	0.473	0.2163	0
	0.496	0.2439	0
	0.521	0.2767	0
	0.546	0.3147	0
	0.565	0.344	0
	0.586	0.3768	0
	0.6	0.401	0

HYSKRG 0.4 **maximum trapped gas saturation

*RTYPE *KVAR 6*2 20*1 3*2

** ============== INITIAL CONDITIONS ====================
*INITIAL
 *VERTICAL *DEPTH_AVE *WATER_GAS *EQUIL *NOTRANZONE
 *ZGAS 0.0 1.0

REFPRES
  4600

REFDEPTH
  10466

DWGC
  4000

SWOC
  0.999
**SWINIT *MATRIX   *CON 1.0
**SWINIT *FRACTURE *CON 1.0

**TEMPER *MATRIX   *CON 120
**TEMPER *FRACTURE *CON 120
** ============== NUMERICAL CONTROL   ====================
*NUMERICAL
*DTMAX 10
*DTMIN 1e-6
*NORM *PRESS 145.
*NORM *SATUR 0.05
*MAXCHANGE *SATUR 0.8
*MAXCHANGE *PRESS 1000.

*AIM *THRESH 0.1
*CONVERGE *MAXRES 1.E-04
*PRECC 1.E-06

ITERMAX 200

NCHECK-CEQ 3
**=================== GEOMECHANIC SECTION ===================
*GEOMECH   ** Main keyword for geomechanic option
*GEOM3D   ** 3D Finite elements
*GCOUPLING 2

*GEOGRID *GCART   47 39 29
*GDI   *GIVAR 1000 900 2*800 700 2*660 580 200 1*40 27*20 1*40 200 580 2*660 700 2*800 900 1000
*GDJ   *GJVAR 1000 900 2*800 700 2*660 580 200 5*40 11*20 5*40 200 580 2*660 700 2*800 900 1000
*GDK   *GKVAR   50 30 20 10 5 5 20*3.6 5 15 40

*GEODEPTH   *GTOP 1 1 1   10313
**   Linear elastic rock **sandstone
**   Linear elastic rock **shale

**   Linear elastic rock **shale
GEOROCK 1 **Matrix rocktype 1
ELASTMOD 1.99e6
POISSRATIO 0.2548
COHESION 689476
*THEXPCOEF 7.2E-6
*BIOTSCOEF 0.824

GEOROCK 2 **Matrix rocktype 1

113

ELASTMOD 1.95e6
POISSRATIO 0.2203
COHESION 689476
*THEXPCOEF 7.2E-6
*BIOTSCOEF 0.837

GEOROCK 3
ELASTMOD 1.76e+006
POISSRATIO 0.285
COHESION 689476
*THEXPCOEF 7.2E-6
*BIOTSCOEF 0.822

GEOROCK 4
ELASTMOD 1.43e+006
POISSRATIO 0.286
COHESION 689476
*THEXPCOEF 7.2E-6
*BIOTSCOEF 0.855

GEOROCK 5
ELASTMOD 1.31e+006
POISSRATIO 0.286
COHESION 689476
*THEXPCOEF 7.2E-6
*BIOTSCOEF 0.868

GEOROCK 6
ELASTMOD 2.21e+006
POISSRATIO 0.3241
COHESION 689476
*THEXPCOEF 7.2E-6
*BIOTSCOEF 0.728

GEOROCK 7
ELASTMOD 1.26e+006
POISSRATIO 0.3039
COHESION 689476
*THEXPCOEF 7.2E-6
*BIOTSCOEF 0.861

GEOROCK 8 **caprock upper
ELASTMOD 2.44e+006
POISSRATIO 0.3
COHESION 689476
*THEXPCOEF 7.2E-6
*BIOTSCOEF 0.849

GEOROCK 9 **caprock lower
ELASTMOD 3.65e+006
POISSRATIO 0.3
COHESION 689476
*THEXPCOEF 7.2E-6
*BIOTSCOEF 0.774

**fracture rock types

GEOROCK 10
ELASTMOD 1.99e6
POISSRATIO 0.2548
COHESION 689476
*THEXPCOEF 7.2E-6
*BIOTSCOEF 0.824

** B-B model	E0	Kni	FRS	Khf	Kccf	Krcf
*GPERMBB	1.981e-05	6.786e7	0	100000.	233.	1.

GEOROCK 11
ELASTMOD 1.95e6
POISSRATIO 0.2203
COHESION 689476
*THEXPCOEF 7.2E-6
*BIOTSCOEF 0.837

** B-B model	E0	Kni	FRS	Khf	Kccf	Krcf
*GPERMBB	1.981e-05	6.786e7	0	100000.	233.	1.

GEOROCK 12
ELASTMOD 1.76e+006
POISSRATIO 0.285
COHESION 689476
*THEXPCOEF 7.2E-6
*BIOTSCOEF 0.822

** B-B model	E0	Kni	FRS	Khf	Kccf	Krcf
*GPERMBB	1.981e-05	6.786e7	0	100000.	233.	1.

GEOROCK 13
ELASTMOD 1.43e+006
POISSRATIO 0.286
COHESION 689476
*THEXPCOEF 7.2E-6
*BIOTSCOEF 0.855

** B-B model	E0	Kni	FRS	Khf	Kccf	Krcf
*GPERMBB	1.981e-05	6.786e7	0	100000.	233.	1.

GEOROCK 14
ELASTMOD 1.31e+006
POISSRATIO 0.286
COHESION 689476
*THEXPCOEF 7.2E-6
*BIOTSCOEF 0.868

** B-B model	E0	Kni	FRS	Khf	Kccf	Krcf
*GPERMBB	1.981e-05	6.786e7	0	100000.	50.	1.

GEOROCK 15
ELASTMOD 2.21e+006
POISSRATIO 0.3241
COHESION 689476
*THEXPCOEF 7.2E-6
*BIOTSCOEF 0.728

** B-B model	E0	Kni	FRS	Khf	Kccf	Krcf
*GPERMBB	1.981e-05	6.786e7	0	100000.	50.	1.

GEOROCK 16
ELASTMOD 1.26e+006

POISSRATIO 0.3039
COHESION 689476
*THEXPCOEF 7.2E-6
*BIOTSCOEF 0.861
** B-B model   E0   Kni   FRS   Khf   Kccf   Krcf
*GPERMBB   1.981e-05   6.786e7   0   100000.   50.   1.

GEOROCK 17 **caprock upper
ELASTMOD 2.44e+006
POISSRATIO 0.3
COHESION 689476
*THEXPCOEF 7.2E-6
*BIOTSCOEF 0.849

GEOROCK 18 **caprock lower
ELASTMOD 3.65e+006
POISSRATIO 0.3
COHESION 689476
*THEXPCOEF 7.2E-6
*BIOTSCOEF 0.774

** 7*1   2*2   3   2*2   4   3   5   4 2*6 3*4
** Assign constitutive model on rock layer
*GEOTYPE *MATRIX *KVAR 6*8 4*1 2*2 2*3 4 2*3 5 4 6 5 2*7 3*5 3*9
*GEOTYPE *FRACTURE *KVAR 6*17 4*10 2*11 2*12 13 2*12 14 13 15 14 2*16 3*14 3*18

** Initial stresses: sigmaxx   sigmayy   sigmazz   sigmaxy   sigmayz   sigmaxz
*STRESS3D   1000.0   0   1100.0   0.0   0.0   0.0
*STRESSGRAD3D   0   0   -0.9336   0 0 0
*DLOADBC3D
*ijk 1:47 1:39 1 **top
** node1 node2 node3 node4 load
         1   2   3   4   455 **1 tonf/m2 = 13.88 psi
**Constant vertical stress 70*13.88 = 971.6 psi

**GOUTSRF   GGRID ALL
** ============= RECURRENT DATA   ===================
*RUN

*DATE 2000 1 1

   *DTWELL 1.0
WELL   'Injector 1'
   **INCOMP WATER
INJECTOR 'Injector 1'
INCOMP   SOLVENT   0.0   1.0
OPERATE   MAX   STG   0.0   CONT
OPERATE   MAX   BHP   4650.0   CONT
**   rad   geofac   wfrac   skin
GEOMETRY   K   0.23   0.2488   1.0   0.0
     PERF   GEO   'Injector 1'
** UBA   ff   Status   Connection
    30 26 7   1.0   OPEN   FLOW-FROM   'SURFACE'   REFLAYER
    30 26 8   1.0   OPEN   FLOW-FROM   1
    30 26 9   1.0   OPEN   FLOW-FROM   2

116

```
   30 26 10          1.0   OPEN     FLOW-FROM   3
   30 26 11          1.0   OPEN     FLOW-FROM   4
   30 26 12          1.0   OPEN     FLOW-FROM   5
   30 26 13          1.0   OPEN     FLOW-FROM   6
   30 26 14          1.0   OPEN     FLOW-FROM   7
   30 26 15          1.0   OPEN     FLOW-FROM   8
   30 26 16          1.0   OPEN     FLOW-FROM   9
   30 26 17          1.0   OPEN     FLOW-FROM   10
   30 26 18          1.0   OPEN     FLOW-FROM   11
   30 26 19          1.0   OPEN     FLOW-FROM   12
   30 26 20          1.0   OPEN     FLOW-FROM   13
   30 26 21          1.0   OPEN     FLOW-FROM   14
   30 26 22          1.0   OPEN     FLOW-FROM   15
   30 26 23          1.0   OPEN     FLOW-FROM   16
   30 26 24          1.0   OPEN     FLOW-FROM   17
   30 26 25          1.0   OPEN     FLOW-FROM   18
   30 26 26          1.0   OPEN     FLOW-FROM   19
```
*INJ-TEMP 'Injector 1'
                                255

*TIME 11
INJECTOR 'Injector 1'
INCOMP   SOLVENT   1.0   0.0
OPERATE   MAX   STG   4672000.0   CONT REPEAT
OPERATE   MAX   BHP   5500.0   CONT REPEAT
*INJ-TEMP 'Injector 1'
                                162
*TIME 12
  *DTWELL 1.0

*TIME 26
INJECTOR 'Injector 1'
OPERATE   MAX   STG   4883000.0

   *DTWELL 0.01

*TIME 27
INJECTOR 'Injector 1'
OPERATE   MAX   STG   4368000.0

*TIME 28
INJECTOR 'Injector 1'
OPERATE   MAX   STG   6311000.0

*TIME 30
INJECTOR 'Injector 1'
OPERATE   MAX   STG   9792000.0   CONT

*TIME 31
INJECTOR 'Injector 1'
OPERATE   MAX   STG   9564000.0   CONT

*TIME 32
INJECTOR 'Injector 1'
OPERATE   MAX   STG   9134400.0   CONT

117

*TIME 48
INJECTOR 'Injector 1'
OPERATE   MAX   STG   9336000.0   CONT

  *DTWELL 0.1

*TIME 50
INJECTOR 'Injector 1'
OPERATE   MAX   STG   7380000.0

  *DTWELL 0.01

*TIME 51.5
INJECTOR 'Injector 1'
OPERATE   MAX   STG   8966000.0

   *DTWELL 0.1

*TIME 66
INJECTOR 'Injector 1'
OPERATE   MAX   STG   8528000.0

   *DTWELL 0.01
*TIME 75
INJECTOR 'Injector 1'
OPERATE   MAX   STG   6573000.0

*TIME 76
INJECTOR 'Injector 1'
OPERATE   MAX   STG   3322000.0

*TIME 77
INJECTOR 'Injector 1'
OPERATE   MAX   STG   3045000.0

*TIME 81
INJECTOR 'Injector 1'
OPERATE   MAX   STG   9170000.0

*TIME 85
INJECTOR 'Injector 1'
OPERATE   MAX   STG   9109000.0

*TIME 87
INJECTOR 'Injector 1'
OPERATE   MAX   STG   0.0

*TIME 90
INJECTOR 'Injector 1'
OPERATE   MAX   STG   2791000.0

*TIME 91
INJECTOR 'Injector 1'
OPERATE   MAX   STG   9191000.0

*TIME 97

INJECTOR 'Injector 1'
OPERATE   MAX   STG   5358000.0

*TIME 98.5
INJECTOR 'Injector 1'
OPERATE   MAX   STG   9110000.0
 *DTWELL 0.1

*TIME 104
INJECTOR 'Injector 1'
OPERATE   MAX   STG   9377800.0

*TIME 130
INJECTOR 'Injector 1'
OPERATE   MAX   STG   8738500.0

*TIME 160
INJECTOR 'Injector 1'
OPERATE   MAX   STG   9181000.0

*TIME 166
INJECTOR 'Injector 1'
OPERATE   MAX   STG   10560000.0

*TIME 166.5
INJECTOR 'Injector 1'
OPERATE   MAX   STG   13830000.0

*TIME 169
INJECTOR 'Injector 1'
OPERATE   MAX   STG   11370000.0

*TIME 170
INJECTOR 'Injector 1'
OPERATE   MAX   STG   13930000.0
 *DTWELL 0.1

*TIME 231
INJECTOR 'Injector 1'
OPERATE   MAX   STG   11130000.0

*TIME 232
INJECTOR 'Injector 1'
INCOMP   SOLVENT   1.0   0.0
OPERATE   MAX   STG   5067000.0

*TIME 232.1
*STOP

Bibliography

Al Hosni, M, Vialle, S., Gurevich, B., and Daley, T. M., 2016, Estimation of rock frame weakening using time-lapse crosswell: The Frio birne pilot project, Geophysics, Volume 81 Pages B235-B245.

Alsalman, M. E., Myers, M. T., & Sharf-Aldin, M. H. 2015. Comparison of Multistage to Single Stage Triaxial Tests. In 49th US Rock Mechanics/Geomechanics Symposium. American Rock Mechanics Association.

Aman, M., D. N. Espinoza, A. G. Ilgen, J. R. Major, P. Eichhubl, and T. A. Dewers. 2017a. CO_2-induced chemo-mechanical alteration in reservoir rocks assessed via batch reaction experiments and scratch testing, Greenhouse Gas Science Technology, Volume 8, Pages 133-149.

Aman M. D., Ilgen A., Major J., Eichhubl P., Dewers T., Espinoza D. N. 2017b. Characterization of chemo-mechanical alteration in CO_2 storage rocks via scratch testing, Greenhouse Gases: Science and Technology.

ASTM. 2010. D7012–10: Standard test method for compressive strength and elastic moduli of intact rock core specimens under varying states of stress and temperatures. Annual Book of ASTM Standards, American Society for Testing and Materials, West Conshohocken, PA, Pages 495-498.

Bakker, E., Hangx, S. J., Niemeijer, A. R., & Spiers, C. J. 2016. Frictional behaviour and transport properties of simulated fault gouges derived from a natural CO_2 reservoir. International Journal of Greenhouse Gas Control, Volume 54, Pages 70-83.

Barton, N., S. Bandis, and K. Bakhtar. 1985. Strength, deformation and conductivity coupling of rock joints. International Journal of Rock Mechanics and Mining Sciences & Geomechanics Abstracts, Volume 22, Pages 121-140

Bauer, R. A., M. Carney, and R. J. Finley. 2016. Overview of microseismic response to CO_2 injection into the Mt.Simon saline reservoir at the Illinois Basin-Decatur Project, International Journal of Greenhouse Gas Control, Volume 54, Pages 378-388

Benavente, D., García, M. A., García, J., Sánchez-Moral, S., & Ordóñez, S. 2004. Role of pore structure in salt crystallisation in unsaturated porous stone. Journal of crystal growth, Volume 260, Pages 532-544.

Bemer, E., & Lombard, J. M. 2010. From injectivity to integrity studies of CO_2 geological storage-chemical alteration effects on carbonates petrophysical and geomechanical properties. Oil & Gas Science and Technology–Revue de l'Institut Français du Pétrole, Volume 65, Pages 445-459.

Bernier F, Li AL, Bastiaens W, Ortiz L, Van Geet M, Wouters L, Freig B, Blümling P, Desrues J, Viaggiani G, Coll C, Chanchole S, De Greef V, Hamza R, Malinsky L, Vervoort A, Vanbrabant Y, Debecker B, Verstraelen J, Govaerts A, Wevers M,

Labiouse V, Escoffier S, Mathier J-F, Gastaldo L, Bühler C. 2007 Fractures and self-healing within the Excavation Disturbed Zone in clays (SELFRAC). Technical Report EUR 22585, European Commission Nuclear Science and Technology.

Benson, S. M. and T. Surles. 2006. Carbon Dioxide Capture and Storage: An Overview with Emphasis on Capture and Storage in Deep Geological Formations, Proceedings of the IEEE, Volume 94, Pages 1795-1805.

Benson, S. M. & D. R. Cole. 2008. CO_2 sequestration in Deep Sedimentary Formations. Elements. Volume 4, Pages 325-331.

Bjerrum, L., Kennard, R. M., Gibson, R. E., and Nash, J. 1972. Hydraulic fracturing in field permeability testing. Geotechnique, Volume 22, Iss. 2, Pages 319-332.

Bosswell, R., Shelander, D., Lee, M., Latham, T., Collett, T., Guerin, G., Moridis, G., Reagan, M. and Goldberg, D., 2009. Occurrence of gas hydrate in Oligocene Frio sand: Alaminos Canyon Block 818: Northern Gulf of Mexico, Marine and Petroleum Geology, Volume 26, Pages 1499-1512

Burnside, N. M., Shipton, Z. K., Dockrill, B., and Ellam, R. M., 2013, Man-made versus natural CO_2 leakage: A 400 k.y. history of an analogue for engineered geological storage of CO_2: Geology, Volume 41, Pages 471-474.

Carroll, S., Hao, Y., Smith, M., & Sholokhova, Y. 2013. Development of scaling parameters to describe CO_2–rock interactions within Weyburn-Midale carbonate

flow units. International Journal of Greenhouse Gas Control, Volume 16, Pages S185-S193.

Carrigan C. R., X. Yang, D. J. LaBrecque, D. Larsen, D. Freeman, A. L. Ramirez, W. Daily, R. Aines, R. Newmark, J. Friedmann, and S. D. Hovorka. 2013. Electrical resistance tomographic monitoring of CO_2 movement in deep geologic reservoirs, International Journal of Greenhouse Gas Control, Volume 18, Pages 401-408.

Carpenter, C. B. and Spencer, G. B. 1940. Measurements of compressibility of consolidated oil-bearing sandstones, Report 3540, U. S. Bureaus of Mines, Denver

Carter, R. W., and K. T. Spikes. 2013 Sensitivity analysis of Tuscaloosa sandstones to CO_2 saturation, Cranfield field, Cranfield, MS, International Journal of Greenhouse Gas Control, Volume 18, Pages 485-496.

Cha, M., & Santamarina, J. C. 2014. Dissolution of randomly distributed soluble grains: post-dissolution k 0-loading and shear. Géotechnique, Volume 64, Pages 828-836.

Chiodini, G., Frondini, F., & Ponziani, F. 1995. Deep structures and carbon dioxide degassing in central Italy. Geothermics, Volume 24, Pages 81-94.

Computer Modeling Group Ltd. 2013. Compositional & Unconventional Reservoir Simulation. Calgary.

Daley, T. M., J. Henderickson, and J. H. Queen. 2014, Monitoring CO_2 Storage at Cranfield, Mississippi with Time-Lapse Offset VSP – Using Integration and Modeling to Reduce Uncertainty, MS, Energy Procedia, Volume 63, Pages 4240-4248.

Delshad, M., Kong, X., & Wheeler, M. F. 2011. On Interplay of Capillary, Gravity, and Viscous Forces on Brine/CO_2 Relative Permeability in a Compositional and Parallel Simulation Framework. Presented at the SPE Reservoir Simulation Symposium, The Woodlands, Texas, 21-23 February. SPE-142146-MS.

Delshad, M., Thomas, S. G. and Wheeler, M. F. 2011. Parallel Numerical Reservoir Simulations of Nonisothermal Compositional Flow and Chemistry. Society of Petroleum Engineers, 118847-PA, Volume 16, Pages 239-248.

Delshad, M., X. Kong, R. Tavakoli, S. A. Hosseini, M. F. Wheeler. 2013. Modeling and simulation of carbon sequestration at Cranfield incorporating new physical models, International Journal of Greenhouse Gas Control, Volume 18, Pages 463-473.

Dockrill, B., and Shipton, Z. K., 2010, Structural controls on leakage from a natural CO_2 geologic storage site; central Utah, U.S.A: Journal of Structural Geology, Volume 32, Pages 1768-1782.

Doelling, H. H. 2002. Interim Geologic Map of the San Rafael Desert 30' x 60 ' Quadrangle, Emery and Grand Counties, Utah. Salt Lake City: Utah Geological Survey.

Duan, Z., & Sun, R. 2003. An improved model calculating CO_2 solubility in pure water and aqueous NaCl solutions from 273 to 533 K and from 0 to 2000 bar. Chemical geology, Volume 193, Pages 257-271.

Dudley, J.W., Brignoli, M., Crawford, B.R., Ewy, R.T., Love, D.K., McLennan, J.D., Ramos, G.G., Shafer, J.L., Sharf-Aldin, M.H., Siebrits, E. and Boyer, J., 2016.

ISRM suggested method for uniaxial-strain compressibility testing for reservoir geomechanics. Rock Mechanics and Rock Engineering, Volume 49, Pages 4153-4178.

Doughty, C., Freifeld, B. M., Trautz, R. C. 2008. Site characterization for CO_2 geologic storage and vice versa: the Frio brine pilot, Texas, USA as a case study. Environmental Geology, Volume 54, Pages 1635-1656.

Ehlig-Economides, C. and M. J. Economides. 2010. Sequestering carbon dioxide in a closed underground volume. Journal of Petroleum Science and Engineering, Volume 70, Pages 123-130.

Ellsworth, W. L. 2013. Injection-Induced Earthquakes. Science, Volume 341 Iss 6142, Pages 1225942

Eichhubl, P., Taylor, W. L., Pollard, D. D., & Aydin, A. 2004. Paleo-fluid flow and deformation in the Aztec Sandstone at the Valley of Fire, Nevada—Evidence for the coupling of hydrogeologic, diagenetic, and tectonic processes. Geological Society of America Bulletin, Volume 116, Pages 1120-1136.

Espinoza, D. N., and Santamarina J. C. 2010. Water-CO_2-mineral systems: Interfacial tension, contact angle, and diffusion—Implications to CO_2 geological storage, Water Resources Research, Volume 46, Pages 1-10.

Espinoza, D. N., S. H. Kim, and J. C. Santamarina. 2011. CO_2 geological storage - Geotechnical implications, KSCE Journal of Civil Engineering, Volume 15, Pages 707-719.

Espinoza, D. N., & Santamarina, J. C. 2012. Clay interaction with liquid and supercritical CO_2: the relevance of electrical and capillary forces. International Journal of Greenhouse Gas Control, Volume 10, Pages 351-362.

Espinoza, D. N., Pereira, J. M., Vandamme, M., Dangla, P., & Vidal-Gilbert, S. 2015. Desorption-induced shear failure of coal bed seams during gas depletion. International Journal of Coal Geology, Volume 137, Pages 142-151.

Espinoza, D. N., Jung, H., Major, J. R., Sun, Z., Ramos, M. J., Eichhubl, P., Balhoff, M. T. Choens, R. C., Dewers, T. A. 2018. CO_2 charged brines changed rock strength and stiffness at Crystal Geyser, Utah: Implications for leaking subsurface CO_2 storage reservoirs. International Journal of Greenhouse Gas Control. Volume 73. Pages 16-28.

Fernandez, A. L., & Santamarina, J. C. 2001. Effect of cementation on the small-strain parameters of sands. Canadian Geotechnical Journal, Volume 38, Pages 191-199.

Fetkovich, M. J., Reese, D. E., and C. H. Whitson. 1998. Application of a General Material Balance for High-Pressure Gas Reservoirs, Society of Petroleum Engineers Journal, Volume 3.

Fjaer, E., R. M. Holt, A. M. Raaen, R. Risnes, and P. Horsrud. 2008. Petroleum Related Rock Mechanics, Elsevier Science, Volume 53, 2nd Edition.

Fredd, C. N., & Fogler, H. S. 1998. Influence of transport and reaction on wormhole formation in porous media. AIChE journal, Volume 44, Pages 1933-1949.

Frohlich, C. 2012. Two-year survey comparing earthquake activity and injection-well locations in the Barnett Shale, Texas, Proceedings of the National Academy of Sciences of the United States of America, Volume 109, Pages 13934-13938

Gale, J. F., Reed, R. M., & Holder, J. 2007. Natural fractures in the Barnett Shale and their importance for hydraulic fracture treatments. AAPG Bulletin, Volume 91, Pages 603-622.

Gaus, I., Azaroual, M., & Czernichowski-Lauriol, I. 2005. Reactive transport modelling of the impact of CO_2 injection on the clayey cap rock at Sleipner (North Sea). Chemical Geology, Volume 217, Pages 319-337.

Ghomian, Y., 2008. Reservoir simulation studies for coupled CO_2 sequestration and enhanced oil recovery, PhD dissertation, University of Texas Digital Library

Gor, G. Y., and J. H. Prevost. 2013. Effect of CO_2 injection temperature on caprock stability. Energy Procedia, Volume 37, Pages 3727-3732.

Goulty, N.R., 2003. Reservoir stress path during depletion of Norwegian chalk oilfields. Petroluem Geoscience, Volume 9, Pages 233–241.

Gueguen, Y., & Bouteca, M. 1999. Mechanical properties of rocks: Pore pressure and scale effects. Oil & Gas Science and Technology, Volume 54, Pages 703-714.

Gunter, W. D., Perkins, E. H., and Hutcheon, I. 2000. "Aquifer disposal of acid gases: Modelling of water-rock reactions for trapping of acid wastes." Applied Geochemistry, Volume 15, Pages 1085-1095.

Hangx, S. J. T., Spiers, C. J., & Peach, C. J. 2010. The effect of deformation on permeability development in anhydrite and implications for caprock integrity during geological storage of CO_2. Geofluids, Volume 10, Pages 369-387.

Hangx S., A. Linden, F Marcelis, and A Bauer. 2012. The effect of CO_2 on the mechanical properties of the Captain Sandstone: Geological storage of CO_2 at the Goldeneye field (UK), International Journal of Greenhouse Gas Control, Volume 19, Pages 609-619.

Hangx, S., Bakker, E., Bertier, P., Nover, G., & Busch, A. 2015. Chemical–mechanical coupling observed for depleted oil reservoirs subjected to long-term CO_2-exposure–A case study of the Werkendam natural CO_2 analogue field. Earth and Planetary Science Letters, Volume 428, Pages 230-242.

Heath, J. E., Lachmar, T. E., Evans, J. P., Kolesar, P. T., and Williams, A. P., 2009, Hydrogeochemical characterization of leaking, carbon dioxide-charged fault zones in east-central Utah, with implications for geological carbon storage: Geophysical Monograph, Volume 183, Pages 147-158

Hosseini, S. A., H. Lashgari, J. W. Choi, J. Nicot, J. Lu, and S. D. Hovorka. 2013. Static and dynamic reservoir modeling for geological CO_2 sequestration at Cranfield, Mississippi, U.S.A., International Journal of Greenhouse Gas Control, Volume 18, Pages 449-462.

Hovorka, S. D., Holtz, M. H., Sakurai, S., and others 2003. Report to the Texas Commission on Environmental Quality to Accompany a Class V Application for an Experimental Technology Pilot Injection Well: Frio Pilot in CO_2 Sequestration in Brine-Bearing Sandstones.

Hovorka, S. D., Doughty, C., Benson, S. M., Pruess, K., and Knox, P. R. 2004. The impact of geological heterogeneity on CO_2 storage in brine formations: a case study from the Texas Gulf Coast. Geological Society, London, Special Publications, Volume 233, Pages 147-163.

Hovorka, S. D., C. Doughty, S. M. Benson, and others 2006. Measuring permanence of CO_2 storage in saline formations: The Frio experiment. Environmental Geosciences, Volume 13, Pages 105–121.

Hovorka, S. D., T. A. Meckel, and R. H. Trevino. 2013. Monitoring a large-volume injection at Cranfield, Mississippi—Project design and recommendations, International Journal of Greenhouse Gas Control, Volume 18, Pages 345-360.

IPCC. 2005. Underground geological storage, – Metz, B., O. Davidson, H. Coninck, M. Loos, and L. Meyer (Eds.) IPCC Special Report on Carbon Dioxide Capture and

Storage, prepared by Working Group III of the Intergovernmental Panel on Climate Change, Cambridge University Press, Cambridge, UK, and New York, USA, pp 195–276

Islam, A., A. Y. Sun, and J. Lu. 2016. Simulating in-zone chemistry changes from injection time to longer periods of CO_2 storage, Environmental Earth Sciences, Volume 75.

Jung, H. and D. N. Espinoza. 2017. Chemo-Poromechanical Properties of Tuscaloosa Sandstone: Implications on CO_2 Geological Storage. 51st U.S. Rock Mechanics/Geomechanics Symposium, 25-28 June, San Francisco, California, USA, ARMA-2017-0303

Jung, H., Singh, G., Nicolas Espinoza, D., & Wheeler, M. F. 2017a. An Integrated Case Study of the Frio CO_2 Sequestration Pilot Test for Safe and Effective Carbon Storage Including Compositional Flow and Geomechanics. In SPE Reservoir Simulation Conference. Society of Petroleum Engineers

Jung, H., G. Singh, D. N. Espinoza, and M. F. Wheeler. 2017b. Quantification of a maximum injection volume of CO_2 to avert geomechanical perturbations using a compositional fluid flow reservoir simulator. Advances in Water Resources. Volume 112, Pages 160-169.

Jung, H., D. N. Espinoza, and S. A. Hosseini. 2018a. Local stress changes near CO_2 injection wells due to thermo-poro-mechanical processes: impact of formation

heterogeneity. 52st U.S. Rock Mechanics/Geomechanics Symposium, 16-20 June, Seattle, Washington, USA, ARMA-2018-0889.

Jung, H., D. N. Espinoza, and S. A. Hosseini. 2018b. Wellbore injectivity response to step-rate CO_2 injection: coupled thermo-poro-elastic analysis in a vertically heterogeneous formation. International Journal of Greenhouse Gas Control. (Submitted).

Kaszuba, J. P., Janecky, D. R., and Snow, M. G. 2005. Experimental evaluation of mixed fluid reactions between supercritical carbon dioxide and NaCl brine: Relevance to the integrity of a geologic carbon repository. Chemical Geology, Volume 217, Pages 277-293.

Kharaka, Y. K., Cole, D. R., Hovorka, S. D., Gunter, W. D., Knauss, K. G., & Freifeld, B. M. 2006. Gas-water-rock interactions in Frio Formation following CO_2 injection: Implications for the storage of greenhouse gases in sedimentary basins. Geology, Volume 34, Pages 577-580.

Kim, J., Tchelepi, H. A., Juanes, R. 2011. Stability, accuracy, and efficiency of sequential methods for coupled flow and geomechanics. Society of Petroleum Engineers, Volume 16, Pages 249-262.

Kim, S. H. and S. A. Hosseini. 2013. Above-zone pressure monitoring and geomechanical analyses for a field-scale CO_2 injection project in Cranfield, MS. Society of Chemical Industry. Greenhouse Gas Sci Technol.Volume 4, Pages 81-98.

Kim, S., & Santamarina, J. C. 2014. CO_2 geological storage: hydro-chemo-mechanical analyses and implications. Greenhouse Gases: Science and Technology, Volume 4, Pages 528-543.

Kim, S. H. and S. A. Hosseini. 2017. Study on the ratio of pore-pressure/stress changes during fluid injection and its implications for CO_2 geologic storage, Journal of Petroleum Science and Engineering, Volume 149, Pages 138-150.

Kneafsey, T. J., & Pruess, K. 2010. Laboratory flow experiments for visualizing carbon dioxide-induced, density-driven brine convection. Transport in Porous Media, Volume 82, Pages 123-139.

Kong, X., Delshad, M., and Wheeler, M. F. 2015. History Matching Heterogeneous Coreflood of CO_2/brine by Use of Compositional Reservoir Simulator and Geostatistical Approach. Society of Petroleum Engineers, Volume 20, 267-276.

Kumar, A., Noh, M. H., Ozah, R. C., Pope, G. A., Bryant, S. L., Sepehrnoori, K., & Lake, L. W. 2005. Reservoir simulation of CO_2 storage in aquifers. Society of Petroleum Engineeris Journal, Volume 10, Pages 336-348.

Lake, L. W. 1996. Enhanced oil recovery. Prentice Hall. 600 p.

Lee, H. P., Olson, J. E., Holder, J., Gale, J. F., & Myers, R. D. 2015. The interaction of propagating opening mode fractures with preexisting discontinuities in shale. Journal of Geophysical Research: Solid Earth, Voluem 120, Pages 169-181.

Lorenz, J. C., L. W. Teufel, and N. R. Warpinski. 1991. Regional fractures; I, A mechanism for the formation of regional fractures at depth in flat-lying reservoirs, American Association of Petroleum Geologists, Volume 5, Pages 1714-1737.

Liteanu, E., Spiers, C. J., & De Bresser, J. H. P. 2013. The influence of water and supercritical CO_2 on the failure behavior of chalk. Tectonophysics, Volume 599, Pages 157-169.

Lu, J., Y. K. Kharaka, J. J. Thordsen, J. Horita, A. Karamalidis, C. Griffith, J. A. Hakala, G. Ambats, D. R. Cole, T. J. Phelps, M. A. Manning, P. J. Cook, and S. D. Hovorka. 2012. CO_2–rock–brine interactions in Lower Tuscaloosa Formation at Cranfield CO_2 sequestration site, Mississippi, U.S.A., Chemical Geology, Volume 291, Pages 269-277.

Lu, J., M. Kordi, S.D. Hovorka, T.A. Meckel, and C.A. Christopher. 2013. Reservoir characterization and complications for trapping mechanisms at Cranfield CO_2 injection site, International Journal of Greenhouse Gas Control, Volume 18, Pages 361-374

Luo, Z., and S. Bryant. 2011. Influence of Thermo-Elastic Stress on Fracture Initiation During CO_2 Injection and Storage. Energy Procedia. Volume 4, Pages 3714-3721.

Major, J.R., Eichhubl, P., Dewers, T.A., Urquhart, A.S., Olson, J.E., Holder, J., 2014. The Effect of CO_2-Related Diagenesis on Geomechanical Failure Parameters: Fracture Testing of CO_2-Altered Reservoir and Seal Rocks from a Natural Analog at Crystal

Geyser, Utah, ARMA. American Rock Mechanics Association, Minneapolis, MN, Pages 1-5.

McDuff, D., Shuchart, C. E., Jackson, S., Postl, D., & Brown, J. S. 2010. Understanding wormholes in carbonates: Unprecedented experimental scale and 3-D visualization. In SPE Annual Technical Conference and Exhibition. Society of Petroleum Engineers.

McGrail, B. P., Schaef, H. T., Glezakou, V.-A., Dang, L. X., and Owen, A. T. 2009. "Water reactivity in liquid and scCO$_2$ phase: Has half the story been neglected?." Energy Procedia GHGT-9, Volume 1, Pages 3415-3419.

Menaceur H, Delage P, Tang A, Conil N. On the thermo-hydro-mechanical behaviour of a sheared Callovo-Oxfordian claystone sample with respect to the EDZ behaviour. 2015 Rock Mechanics and Rock Engineering, Volume 49, Pages 15875-1888.

Mikelic, A. and Wheeler, M. F. 2013. Convergence of iterative coupling for coupled flow and geomechanics. Computational Geosciences, Volume 17, pp 455-461.

Min, B., M. F. Wheeler, and A. Y. Sun. 2017. Parallel Multiobjective Optimization for the Coupled Compositional/Geomechanical Modeling of Pulse Testing, SPE Reservoir Simulation Conference 2017 at Mongomery, 20 – 22 February.

Muller, N., Ramakrishnana, T.S., Boyd, A. and Sakruai, S. 2007. Time-lapse carbon dioxide monitoring with pulsed neutron logging, International Journal of Greenhouse Gas Control, Volume 1, Pages 456-472

Nikolinakou, M. A., Flemings, P. B., and Hudec, M. R. 2013. Modeling stress evolution around a rising salt diaper. Marine and Petroleum Geology, Volume 51, Pages 230-238.

Oudinot, A., Koperna, G., Philip, Z., Liu, N., Heath, J., Wells, A., Young, G., Wilson, T., 2011. CO_2 injection performance in the Fruitland Coal Fairway, San Juan Basin: results of a field pilot. Society of Petroleum Engineers Journal. Volume 16, Pages 864–879.

Owen, G. Deformation processes in unconsolidated sands, Geological Society, London, Special Publictaions, Volume 29, Pages 11-24.

Peters, E. J. 2012, Advanced Petrophysics. Austin, Texas: Live Oak Book Company

Pacala, S., & Socolow, R. 2004. Stabilization wedges: solving the climate problem for the next 50 years with current technologies. Science, Volume 305, Pages 968-972.

Paluszny, A., Salimzadeh, S., Tempone, P., & Zimmerman, R. W. 2017. Evaluating Natural Fracture Growth in Shale Caprocks During Cold CO_2 Injection at the Heletz Pilot Site. In 51st US Rock Mechanics/Geomechanics Symposium. American Rock Mechanics Association.

Pearce, J. M., Holloway, S., Wacker, H., Nelis, M. K., Rochelle, C., & Bateman, K. 1996. Natural occurrences as analogues for the geological disposal of carbon dioxide. Energy Conversion and Management, Volume 37, Pages 1123-1128.

Perkins, T. K., and J. A. Gonzalez. 1985. The Effect of Thermoelastic Stresses on Injection Well Fracturing. Society of Petroleum Engineers Journal, Volume 25.

Rachford, H.H., Rice, J.D. 1952. Procedure for the use of electronic digital computers in calculating flash vaporization hydrocarbon equilibrium. Society of Petroleum Engineers. Volume 4, Iss 10, Pages 327-328

Ramos, M., Espinoza, D. N., Torres-Verdin, C., Grover T. Use of shear-wave anisotropy to quantify the onset of stress-induced microfracturing. Geophysics – In press.

Rimmelé, G., Barlet-Gouédard, V., & Renard, F. 2010. Evolution of the petrophysical and mineralogical properties of two reservoir rocks under thermodynamic conditions relevant for CO_2 geological storage at 3 km depth. Oil & Gas Science and Technology–Revue de l'Institut Français du Pétrole, Volume 65, Pages 565-580.

Rinaldi, A. P., and J. Rutqvist. 2013. Modeling of deep fracture zone opening and transient ground surface uplift at KB-502 CO_2 injection well, In Salah, Algeria, International Journal of Greenhouse Gas Control, Volume 12, Pages 155-167.

Rinehart, A. J., T. A. Dewers, S. T. Broome, and P. Eichhubl. 2016. Effects of CO_2 on mechanical variability and constitutive behavior of the Lower Tuscaloosa Formation, Cranfield Injection Site, USA, International Journal of Greenhouse Gas Control, Volume 53, Pages 305-318.

Rohmer, J., Pluymakers, A., & Renard, F. 2016. Mechano-chemical interactions in sedimentary rocks in the context of CO_2 storage: Weak acid, weak effects?. Earth-Science Reviews, Volume 157, Pages 86-110.

Ross, G. D., Todd, A. C., Tweedie, J. A., & Will, A. G. 1982. The dissolution effects of CO_2-brine systems on the permeability of UK and North Sea calcareous sandstones. In SPE Enhanced Oil Recovery Symposium. Society of Petroleum Engineers.

Rutqvist, J., A. P. Rinaldi, F. Cappa, P. Jeanne, A. Mazzoldi, L. Urpi, Y. Guglielmi and V. Vilarrasa. 2016. Fault activation and induced seismicity in geological carbon storage–Lessons learned from recent modeling studies. Journal of Rock Mechanics and Geotechnical Engineering, Volume 8, Pages 789-804.

Sakurai, S., Ramakrishnan, T. S., Boyd, A., Mueller, N., and Hovorka, S. D. 2006. Monitoring Saturation Changes for CO_2 Sequestration: Petrophysical Support of the Frio Brine Pilot Experiment. Society of Petrophysics and Well Log Analysis, Volume 47, Pages 483-496.

Sathaye, K. J., Hesse, M. A., Cassidy, M., & Stockli, D. F. 2014. Constraints on the magnitude and rate of CO_2 dissolution at Bravo Dome natural gas field. Proceedings of the National Academy of Sciences, Volume 111, Pages 15332-15337.

Segall, P., & Fitzgerald, S. D. 1998. A note on induced stress changes in hydrocarbon and geothermal reservoirs. Tectonophysics, Volume 289, Pages 117-128.

Settari, A. and Maurits, F. 1998. A coupled reservoir and geomechanical simulations system. Society of Petroleum Engineers, Volume 3, Pages 219-226.

Sharp, J. M. 1975. The Potential of Enhanced Oil Recovery Processes. In Fall Meeting of the Society of Petroleum Engineers of AIME. Society of Petroleum Engineers.

Shin, H., Santamarina, J. C., & Cartwright, J. A. 2008. Contraction-driven shear failure in compacting uncemented sediments. Geology, Volume 36, Pages 931-934.

Shovkun, I. and D.N. Espinoza. 2018. Geomechanical implications of dissolution of mineralized natural fractures in shale formations, Journal of Petroleum Science and Engineering, Volume 160, Pages 555-564.

Singh, G. and Wheeler, M. F. 2016. Compositional Flow Modeling using a Multipoint Flux Mixed Finite Element Method. Computational Geosciences, Volume 20, Pages 421-435.

Soltanian, M. R., M. A. Amooie, D. R. Cole, D. E.   Graham, S. A. Hosseini, S. Hovorka, S. M. Pfiffner, T. J. Phelps, and J. Moortgat. 2016. Simulating the Cranfield geological carbon sequestration project with high-resolution static models and an accurate equation of state, International Journal of Greenhouse Gas Control, Volume 54, Pages 282-296.

Sone, H. and M. D. Zoback, 2014a, Time-dependent deformation of shale gas reservoir rocks and its long-term effect on the in situ state of stress, International Journal of Rock Mechanics and Mining Sciences, Volume 69, Pages 120 – 132

Sone, H. and M. D. Zoback, 2014b, Viscous relaxation model for predicting least principal stress

magnitudes in sedimentary rocks, Journal of Petroleum Science and Engineering, Volume 124, Pages 416 – 431

Spycher, N., Pruess, K., & Ennis-King, J. 2003. CO_2-H_2O mixtures in the geological sequestration of CO_2. I. Assessment and calculation of mutual solubilities from 12 to 100 C and up to 600 bar. Geochimica et cosmochimica acta, Volume 67, Pages 3015-3031.

Stefanou, I., & Sulem, J. 2014. Chemically induced compaction bands: Triggering conditions and band thickness. Journal of Geophysical Research: Solid Earth, Volume 119, Pages 880-899.

Stumm, W., & Morgan, J. J. 2012. Aquatic chemistry: chemical equilibria and rates in natural waters, Volume 126. John Wiley & Sons.

Sun, Y., Aman, M., & Espinoza, D. N. 2016a. Assessment of mechanical rock alteration caused by CO_2–water mixtures using indentation and scratch experiments. International Journal of Greenhouse Gas Control, Volume 45, Pages 9-17.

Sun, Z., Espinoza, D. N., & Balhoff, M. T. 2016b. Discrete element modeling of indentation tests to investigate mechanisms of CO_2-related chemomechanical rock alteration. Journal of Geophysical Research: Solid Earth, Volume 121, Pages 7867-7881.

Sun, Z., Espinoza, D. N., Balhoff, M. T., & Dewers, T. A. Discrete Element Modeling of Micro-scratch Tests: Investigation of Mechanisms of CO_2 Alteration in Reservoir Rocks. Rock Mechanics and Rock Engineering, Pages 1-12.

Sun, Z., Espinoza, D. N., Balhoff, M. T., Reservoir rock chemo-mechanical alteration quantified by triaxial tests and implications to fracture reactivation. International Journal of Rock Mechanics and Mining Sciences. In review.

Torres-Verdin, C. 2016. Integrated Geological-Petrophysical Interpretation of Well Logs. Course Notes of Fundamentals of Well Logging, The University of Texas at Austin

Urquhart, A. S. M., 2011, Structural controls on CO_2 leakage and diagenesis in a natural long-term carbon sequestration analogue: Little Grand Wash fault, Utah [MS Thesis]: University of Texas at Austin, Page 437.

Wheeler, J.A., Wheeler, M.F. and Yotov, I. 2002. Enhanced Velocity Mixed Finite Element Methods for Flow in Multiblock Domain. Computational Geosciences, Volume 6, Pages 315-332.

White, W. B., Culver, D. C., Herman, J. S., Kane, T. C., & Mylroie, J. E. 1995. Karst lands. American scientist, Pages 450-459.

Wigley, M., Kampman, N., Dubacq, B., and Bickle, M., 2012, Fluid-mineral reactions and trace metal mobilization in an exhumed natural CO_2 reservoir, Green River, Utah: Geology.

Wilkinson, M., Gilfillan, S. V. M., Haszeldine, R. S., and Ballentine, C. J., 2009, Plumbing the Depths: Testing Natural Tracers of Subsurface CO_2 Origin and Migration, Utah, in Grobe, M., Pashin, J. C., and Dodge, R. L., eds., Carbon dioxide sequestration in geological media—State of the science, Volume AAPG studies in geology: Tulsa, OK, American Association of Petroleum Geologists, Pages 619–634.

Xie, S. Y., Shao, J. F., & Xu, W. Y. 2011. Influences of chemical degradation on mechanical behaviour of a limestone. International Journal of Rock Mechanics and Mining Sciences, Volume 48, Pages 741-747.

Xu, T., Apps, J. A., & Pruess, K. 2005. Mineral sequestration of carbon dioxide in a sandstone–shale system. Chemical geology, Volume 217, Pages 295-318.

Yoksoulian, L.E., J.T. Freiburg, S. K. Butler, P. M. Berger, and W. R. Roy. 2013. Mineralogical alterations during laboratory-scale carbon sequestration experiments for the Illinois Basin, Energy Procedia, Volume 37, Pages 5601-5611.

Zimmerman, W. R., Wilbur H. S., and King S. M. 1986, Compressibility of porous rocks, Journal of Geophysical Research, Volume 91, Pages 12765-12777

Zinsmeister, L., Dautriat, J., Dimanov, A., Raphanel, J., & Bornert, M. 2013. Mechanical evolution of an altered limestone using 2D and 3D digital image correlation (DIC). In 47th US Rock Mechanics/Geomechanics Symposium. American Rock Mechanics Association.

Zoback, M. D. and S. M. Gorelick. 2012. Earthquake triggering and large-scale geologic storage of carbon dioxide. Proceedings of the National Academy of Sciences, Volume 109, Pages 10164-10168.

Zoback, M. D. 2007. Reservoir geomechanics. Cambridge: Cambridge University Press.